Mechanical Behavior of 3D Printed Lattice-Structured Materials

by

Rafaela Vannutelli

Submitted in Partial Fulfillment of the Requirements

for the Degree of

Master of Science in Engineering

in the

Mechanical Engineering

Program

YOUNGSTOWN STATE UNIVERSITY

December 2017

Mechanical Behavior of 3D Printed Lattice-Structured Materials

Rafaela Vannutelli

I hereby release this thesis to the public. I understand that this thesis will be made available from the OhioLINK ETD Center and the Maag Library Circulation Desk for public access. I also authorize the University or other individuals to make copies of this thesis as needed for scholarly research.

Signature:

Rafaela S. Vannutelli, Student Date

Approvals:

Dr. C. Virgil Solomon, Thesis Advisor Date

Dr. Hazel Marie, Committee Member Date

Dr. Jae Joong Ryu, Committee Member Date

Dr. Salvatore A. Sanders, Dean of Graduate Studies Date

Abstract

Lattice structures are created by the repetition of a unit cell where solid struts connected to each other provide parts that combine lightweight and strength. This makes the use of cellular solids advantageous in many applications, varying from engineering to industrial areas. This work focused on designing and mechanical testing of different lattices using 3D printing methods and compression testing. Initially, four different lattices were designed using SolidWorks. Then, the parts were 3D printed from Inconel 718 powders using selective laser melting (SLM). Compression testing of these parts provided mechanical properties that were later compared to a finite element analysis (FEA) model. The four geometries were also 3D printed from NiMnGa powders using binder-jetting technique. This process delivers porous structures that are required in functional materials made of NiMnGa magnetic shape memory alloys (MSMAs) in order to explore the shape memory effects (SMEs). Modeling of these parts provided a better understanding of the compressive behavior of porous structures. Although NiMnGa materials have weak mechanical properties, by creating lattice structures, it was possible to improve the mechanical and functional characteristics and to create parts with controlled porosity, and strength.

Acknowledgements

First I would like to thank my advisor, Dr. C. Virgil Solomon, for giving me the opportunity of working as a research assistant at YSU and to be involved in this thesis project. I appreciate all his support during my time as a graduate student at YSU and none of this work would be possible without him.

Also, I would like to thank the members of this thesis committee, Dr. Hazel Marie and Dr. Jae Joong Ryu for spending their time reading and reviewing all the work.

I owe many thanks to all the colleagues and graduate students at YSU that helped me and gave me advices during my time as a grad student. I would like to specially thank Chris Barret for all the help in 3D printing at America Makes and Matt Caputo for all the time he spent helping me on everything in the lab.

I would like to acknowledge the support offered by the Ohio Federal Research Network (OFRN) High Temperature Magnetic Materials grand for the graduate assistantship received during my second year in the Mechanical Engineering Graduate Program.

My friends and family were essential in this process and gave me all the support to pursue my objectives and I would like to thank you very much.

Finally, I would like to thank Youngstown State University for use of its research facilities within the Center of Excellence in Material Science and Engineering and Center for Innovation in Additive Manufacturing.

Table of Contents

List of Figures and Tables

Chapter 1 – Introduction

1.1. NiMnGa Magnetic Shape Memory Alloys (MSMAs)

Shape memory alloys (SMAs) are smart materials that are able to recover an initial predetermined shape after a deformation is imposed. The strain recovery is called shape memory effect and it is possible due to a reversible thermo-elastic martensitic phase transformation that can be induced via temperature or due to a magnetic field [1].

NiMnGa alloy, the shape memory material explored in this work, is known as a magnetic shape memory alloy (MSMA) with reversible magnetic field induced strain (MFIS). In the presence of a magnetic field, this alloy presents large strains that can be useful in producing actuators and mechanisms that depend on rapid response [2 3]. Internal stresses, created by the magnetic field through the magneto crystalline anisotropy, promote the twin boundaries movement responsible for the strains in the material [4].

Single crystals of NiMnGa present up to 10% of recoverable magnetic field induced strain (MFIS), NiMnGa foam-like materials present up to 8%, and bulk polycrystalline NiMnGa presents up to 0.5% [5]. The mechanical properties of single crystals of NiMnGa, however, are reported to be weak and thus not suitable for structural modeling. The growth process is prone to chemical segregation and internal stresses promote crack nucleation on twin boundary intersections reducing strength and durability of produced parts. Moreover, production of single crystals is difficult [6].

Polycrystalline NiMnGa are then mostly used and, even though they present lower values of MFIS, research conducted by Chmielus *et al.* in 2008 showed that 8.7% of strain can

be achieved on this type of material [7]. By increasing the porosity, the twin boundaries are able to dislocate with reduced constraints and thus increase the strain of the material [8].

Larger MFIS in polycrystalline NiMnGa are also achievable by approaching different strategies, other than porosity, that include growing the grains, and/ or shrinking the sample [4].

The production of NiMnGa particles is possible by different methods. Ball milling and spark erosion are the most common [6, 9, 11]. The ball milling is a cost effective method that delivers high productivity and does not require complexity when compared to the spark erosion process. It is important to notice that the milling energy and the crystalline structure are interdependent. Planetary ball milling consists of a lower energy case where particles show martensitic transformation behavior after annealing above 500°C and present face centered tetragonal structure. The high energy approach, vibration ball milling, produces face centered cubic particles and show a weak martensitic transformation behavior after annealing above 800°C[10]. Spark erosion process presents a lower production volume compared to ball milling and, during the melting, there is potential loss of Mn and Ga due to evaporation [4].

Brittleness is an intrinsic characteristic of NiMnGa alloys and improvement of ductility was reported by spark plasma sintering method [12].

1.2. Inconel 718

The Inconel 718 is a solid-solution or precipitation and an age-hardenable alloy composed of mainly nickel, iron, and chromium. Usually, the microstructure of this alloy consists a three intermetallic precipitation phases: γ', composed of Ni_3 (Al, Ti, Nb), having a cubic ordered face-centered Ll_2 crystal structure; γ'', with Ni_3Nb and body-centered tetragonal (bct) (DO_{22}) crystal structure; and an orthorhombic (DO_a) δ phase with composition Ni_3Nb [13].

Inconel parts with controllable mechanical properties can be produced by conventional methods, such as wrought, cast, and by powder metallurgy sand techniques [14].

Categorized as a superalloy, this material is weldable in aged condition and presents excellent corrosion resistance, fatigue properties, wear resistance, and high strength under temperatures as high as 700 ºC. Thus, it is commonly used for producing parts required to operate at high temperature environments such as jet engines, pump bodies and parts, rocket motors and thrust reversers, and even space craft [15 16].

Conventional manufacturing methods when producing Inconel 718 small size ingots deliver a reasonable microstructure. However, poor part surface integrity and niobium segregation have been reported which leads to the formation of macro-segregation, freckles, Laves phase and white spots [13].

Industrial applications of Inconel 718 have increased by the use of AM methods when producing parts. Development of modern industry requires complex shape structures, high performance, and higher dimension precision. Thus, this material is widely used for 3D printing using selective laser melting (SLM) technique [17].

1.3. Design of Cellular and Lattice Structures

3D printing is a continuum growing market that in 2013 had $3.07 billion of revenue and it is expected to have $12.8 billion on 2018, and more than $21 billion by 2020. This is a rapidly evolving manufacturing approach that is replacing conventional manufacturing methods[18].

Complex shaped parts can now be created with reduced time and material consumption. Part customization is no longer a high cost process and part design is possible with reduced or even elimination of fixture requirements. Low volume custom production is economically advantageously. The Additive Manufacturing (AM) method allows combining increased design complexity with enhanced mechanical properties from the materials processed [19].

The challenges encountered vary among the different types of AM where, depending on the material and the printing parameters, parts can present residual stress and anisotropy. Segregation of phases in microstructure has also been reported due to rapid solidification of molten metal, inherent of some methods[20]. The formation of non-equilibrium phases due to high cooling rates, negatively affects the mechanical properties of printed parts [21]. Thus, there is a need of post processing approaches such as machining and heat treatment to promote stress relief and annealing.

A major advantage of AM includes complex part design for light weight applications such as open cellular foams, monolithic foam combinations used to achieve reticulated mesh structures, engineered porous structures for osseo-integration and non-stochastic

auxetic mesh structures. In almost all cases, such complex shapes and geometries would not be possible to be manufactured by casting or other conventional techniques.

Initially observed in nature, architected cellular structures combine high strength and stiffness with low densities. Animal bones, as an example, present a sophisticated and highly porous core of random ligaments with a gradient density. Thus, biological and mechanical properties are directly influenced by the cellular structures [22].

Implementation of a cellular structure requires designing and selecting a unit cell type. Combining mechanical design with the material scaling improves architectural efficiency with the development of exceptional structural elements. Gibson & Ashby, in 1997, classified different types of cellular solids and provided a comprehensive understanding of the difference between honeycombs, open cell foams, and closed cell foams [25].

The honeycombs are prismatic structures commonly used for defined flows or loads. However, due to thin cell walls, lateral strength and stiffness are reduced and the structure fails via buckling. The presence of strong anisotropy in the out of the plane direction is also observed in this arrangement despite the simplicity when designing honeycombs structures.

An improvement of honeycombs is the sandwich-structured panel. This structure consists of a cellular structure covered with two faces made of thin and stiff material sheet. Thus, under load, sandwich panels carry compression or tension on face sheets while the internal cells carry shear load.

Figure 1.1 shows a schematic of sandwich panel consisting of a honeycomb core structure.

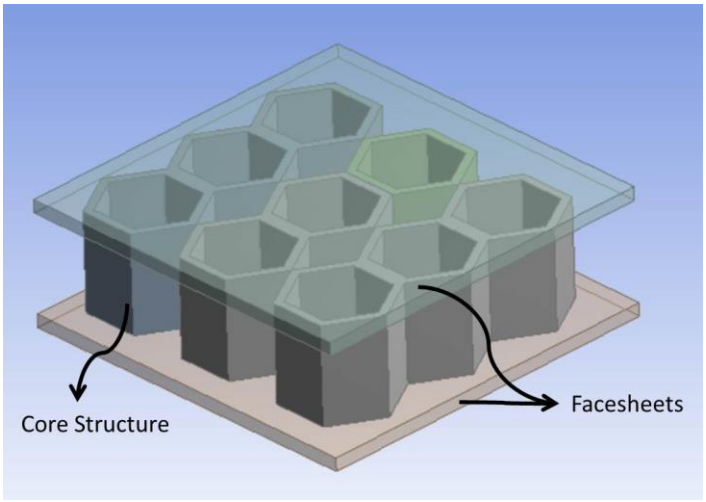

Figure 1.1: Schematic sandwich panel.

Foams are another cellular architecture that has been studied over the years due to the spatial configuration of solids and voids. They present a bending dominated response, which make them not desirable for optimum mechanical properties. On the other hand, foams are ideal for fluid flow, due to the interconnectivity of its structure, and for environment stimulus response such as involving energy absorption.

The selection of the unit cell is then based not only on the manufacturability, but also on the required performance. Exceptional mechanical properties are frequently intrinsic characteristics desired when developing and implementing cellular structures.

Optimization of cellular materials for different loading conditions has enabled the development of the lattice structures. The design of a lattice structure is based on the unit cell architecture that is repeated along the material.

Applications of this mesostructured parts range from biomedical to aeronautic engineering industries where the tradeoff between stiffness and strength to weight ratio

are extremely appealing and implemented on lightweight structures. High mass efficiency can be achieved by the reduction of the structure's mass and use of slender members that contribute to the load bearing properties.

In 2015, Boeing presented a microlattice termed as the lightest metal ever with 99.9% air. This achievement was possible due to the creation of an ordered 3D open cellular structure based on a polymer pattern design. The objective was to create a lightweight structure with hollow tubes that presented energy absorption properties. The goal is to implement the microlattices in structural components of aerospace apparatus [47].

The scale of lattice structures creates the possibility to study them not only by classical methods of mechanics, but also as a material. The manipulation of the mechanical properties of microllatices involve changing strut angles and cross sections, varying relative density, and exploring AM techniques accordingly to the material available.

The basic parameter to be determined when designing and manufacturing a lattice structure is the relative density, given by:

$$\rho_{relative} = \frac{\rho_{known}}{\rho_{part}} \quad (1)$$

where ρ_{known} is the density of the material, and ρ_{part} is the density of the structure. Lowest relative densities achievable for cellular solids are in the order of 0.003. Values above 0.3 are not desired and the structure is then considered a solid with isolated pores.

Porosity is another important parameter and it is the measurement of the amount of void material that occupies the volume. From the relative density, the porosity is defined as:

$$Porosity = 1 - \rho_{relative} \quad (2)$$

Based on the porosity, different cells can be compared varying the design in order to explore the mechanical properties since the shape of cellular solids is a crucial characteristic. Also, depending on the chosen AM method, different levels of porosity are produced and it has a direct influence on the final part depending. A typical analysis when considering design includes, Figure 1.2:

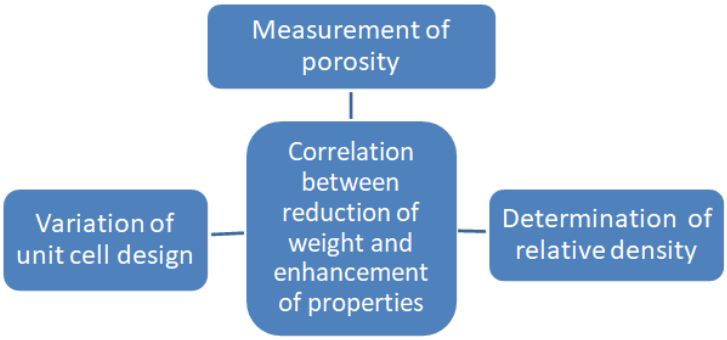

Figure 1.2: Typical design analysis.

It is important to note that stress-strain response of lattice structures are directly dependent on the topology designed. Considering a compressive axial load, two different behaviors are presented depending on the architecture: bend-dominated and stretch-dominated. The first one, bend-dominated, is advantageous for energy absorbing purposes while stretch-dominated behavior is beneficial when designing structures that require improved strength and stiffness.

Bend-dominated structures present a reduced connectivity between the struts and reduced stiffness and strength when compared to stretch-dominated parts at a given relative density. Under an axial compressive load, the increasing load decreases the struts stiffness and they bend. In the case of closed cellular structures, the reduction of stiffness

leads to face buckling as the lateral dimensions are much smaller than the longitudinal. The stretched-dominated lattices present higher stiffness and strength due to the fact that the struts carrying tension fail before than other struts that bend, carry compression or present buckling [23].

The different behaviors can be stablished by a simple equation, when analyzing 3D structures manufactured via AM and under static load case. Considering that all the joints are locked, Maxwell's Stability Criterion states that:

$$M = b - 3j + 6 \quad (3)$$

Where b is the number of struts and j is the number of joints.

Then, for $M<0$, the structure is considered to present bend-dominated behavior and for $M\geq0$, the behavior is stretch-dominated [24].

Mechanical properties of a lattice structure designed with equiaxed cells and isotropic properties can be determined by equations similar to the beam structures. In this case, as shown in Figure 1.3, considering a strut of length *l* under compressive load *P* at its midpoint, the linear elastic deflection obtained is used to calculate the Young's modulus parallel to the load direction:

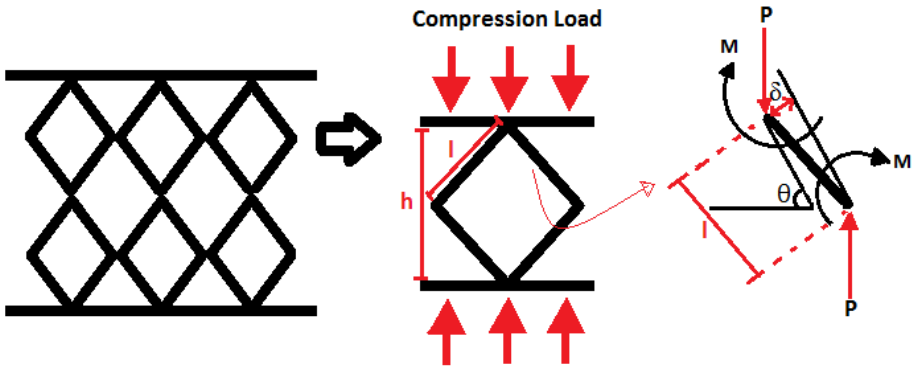

Figure 1.3: Equiaxed cells under compression.

From equilibrium of forces, the moment to bend the strut is given by:

$$M = \frac{Pl\cos\theta}{2} \tag{4}$$

Where l is the length of the strut and P is the load in the y direction.

The strain, given by:

$$\varepsilon = \frac{\delta\cos\theta}{h} \tag{5}$$

Where h is the height of the unit cell. The deflection of the strut is calculated based on the standard beam theory:

$$\delta = \frac{Pl^3\cos\theta}{12EI} \tag{6},$$

Where I is the second moment of inertia and E is the Young's Modulus of the strut.

Finally, the Young's Modulus in the y direction will be given by:

$$E_{y\ direction} = \frac{\sigma}{\varepsilon} \tag{7},$$

Where σ is the stress applied on the lattice based on the force over the area.

Besides bending, inclined struts in cellular structures under compressive load are also subjected to axial and shear load. Unit cells with small aspect ratio present negligible deformations compared to bending, and thus they can be disregarded. However, as the collinearity of the load no longer exists, bending and moment deflections increases creating a non-linear stress strain curve due to the beam column effect. Again, when calculating the Young's modulus, this effect can be neglected for small deflections [25].

Lattice structures designed with slender and straight struts where the length is considerably larger than the strut radius present a similar behavior to a slender structural member, as illustrated below:

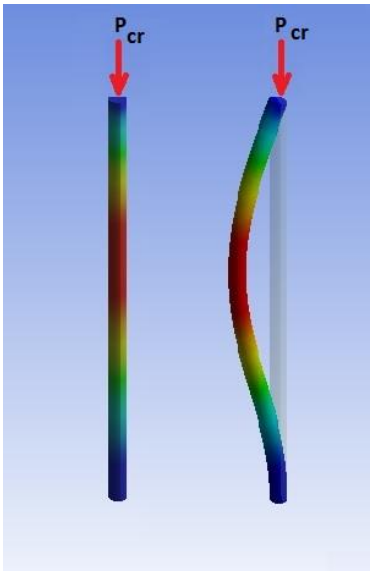

Figure 1.4: Slender structural member under compressive load.

Buckling of the struts is directly related to their slenderness, which is proportional to the relative density. The slenderness is determined as:

$$S = l \cdot \left(\frac{I}{A}\right)^{-1/2} \tag{8}$$

Where l is the length of the strut, I is the second moment of inertia of the strut, and A is the cross sectional area.

For this case, the critical load to cause the buckling, called critical buckling load P_{cr}, is given by Euler formula:

$$P_{cr} = \frac{\pi^2 EI}{(kl)^2} \tag{9}$$

Where E is the modulus of elasticity, I is the second moment of inertia of the strut, l is the strut length, and k is the effective length factor that varies depending on the boundary conditions of the end of the struts. In the case of the lattice structure, $k = 2$ is a recommended design value since both ends of the struts are rotation and translation fixed.

For lattice structures produced via AM, the connections between the struts are nodes with spherical shapes that interfere on the model. This leads to a change of the radius of the struts introducing stress concentration and errors that can invalidate the Euler buckling model [26].

In reality, some lattice structures are considered a type of foam and the mechanical properties follow proportions to the relative density. A lattice created from regular cubic unit cells of length l has the elastic modulus E of the structure described by:

$$\frac{E}{E_S} \propto \frac{\rho_{known}}{\rho_{part}} \tag{10}$$

Where E_s is the Young's modulus of the bulk structure.

This is expected for a structure with bending dominated behavior, where the failure strength σ_{pl} proportion to the relative density is:

$$\frac{\sigma_{pl}}{\sigma_{Bulk}} \propto \left(\frac{\rho_{known}}{\rho_{part}}\right) \tag{11}$$

With σ_{Bulk} described as the yield strength of the bulk structure.

Considering the same situation for a stretching dominated behavior lattice, the elastic modulus E of the structure is described by:

$$\frac{E}{E_S} \propto \frac{1}{3}\left(\frac{\rho_{known}}{\rho_{part}}\right) \tag{12}$$

And the failure strength σ_{pl} proportion to the relative density is:

$$\frac{\sigma_{pl}}{\sigma_{Bulk}} \propto \frac{1}{3}\left(\frac{\rho_{known}}{\rho_{part}}\right) \tag{13}$$

Brittle materials also present proportions between relative elastic modulus and relative density. The collapse of the cell under compressive load in this situation leads to fracture of the struts. Defects inside the structure are random and their presence directly influence on determining the constant of proportionally, where accuracy then cannot be stablished without experimental results [27].

Stress-strain curves obtained from compressive testing of lattice structures are used to study the response of different mechanisms of deformation. Rubber materials present

elastomeric response, metals present elastic-plastic behavior, and ceramic show elastic-brittle behavior. Table 1.1 schematically shows how material and collapse are related under compressive load:

Table 1.1: Collapse mechanisms

Compressive Load	
Material type	Collapse
Linear elastic	Yielding
Elastomeric	Elastic buckling
Brittle	Fracture

A similar regime of the curves can be observed from the three different groups of materials: initially, there is a linear-elastic curve, followed by a plateau of constant stress, and finally a steeply rising stress is present.

Considering metals, the material used for this present work, the typical elastic-plastic stress-strain curve for a lattice structure is shown in Figure 1.5:

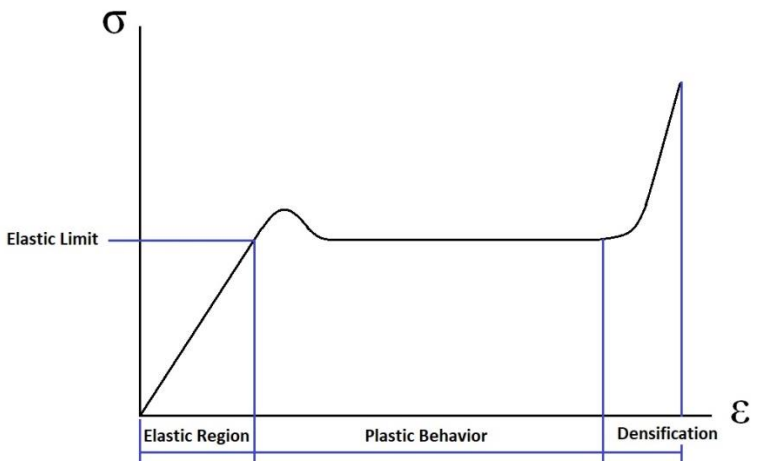

Figure 1.5: Linear-elastic stress-strain curve.

The first region is characterized by a linear elasticity which corresponds to the bending of the struts in the structure. After reaching the critical stress, the plateau of plastic behavior begins and the lattice initiates its collapse. It is common to visualize extensive plasticity for metals that yield plastically and fracture of struts for brittle metals during this process. Finally, at higher strains, the structure is totally collapsed, and further load will promote compression of the cells within each other creating the densification of the material leading to a fast increase of stiffness [25].

Elastic strain is intrinsic in compression testing of the lattice structures. In this case, the stress-strain curve of the elastic region is the extension of the tension curve in the negative direction and presents increased stress strain values than tension. At atomic level, as the stress raises, the interatomic distance increases and less repulsive force exists in between the atoms. The atomic planes slip with the increasing load due to shearing stress resulting in plastic deformation[28].

Optimization of lattice structures involves increasing relative density of the unit cells. As the struts become less slender, the resistance of bending increases, and the stresses required to collapse the lattice are higher. However, plastic behavior region is decreased and the densification starts at lower strains than before [25].

The use of AM methods to manufacture lattices structures offers the opportunity to explore optimization of structures through a facile approach. 3D printed cellular solids are then used to predict and test collapse mechanisms by two different methods: small scale and large scale lattices.

Study of small scale lattices provide information on local deformation behavior and consider a single or a couple of unit cells. Usage of micro-tomography, for mapping strain deformation during axial compressive testing, reveals internal defects which create non uniform strain distribution within the struts for single cells. Thus, localized collapse mechanisms are not homogeneous and vary within the structure since the stress is not uniformly distributed. Compressive testing at nominal quasi-static strain rate of a single cell with octet-truss geometry present a stretch-dominated behavior with an abrupt transition from linear elastic to non-linear anelastic region. On the other hand, same test for single cell with rhombic dodecahedron geometry reveals bend-dominated behavior where the transition between the two regions was smoother [29].

On the other hand, large scale lattice approach is used to study the overall macro-scale deformation mechanism by disregarding the heterogeneous responses encountered from compressive testing of single cells. In this case, development of equivalent continuum method allows performing theatrical analysis of the structure by assuming that a lattice made of periodic unit cells is the continuum material. This assumption is valid for ratio between the structure and the unit cell diameters greater than 20 so that the dimension of the cell is small enough compared to the part [30].

Validation of equivalent continuum method is achievable by developing finite element model. Moreover, the finite element method is used to predict the deformation behavior and understand the stress distribution within the lattice structure. The results are useful to compare the model to the experimental data and map stress concentrations for lattice structures.

1.4. AM using Binder Jetting Process

Among the different AM techniques, the binder jetting process consists in creating a part, layer by layer, by intercalating metal powder and polymer binding agent that bind the particles and layers together. This method does not involve heating from laser which affects the part, and the parts present internal porosity depending on the binder properties.

Figure 1.6 shows the working space of a 3D binder jetting printer.

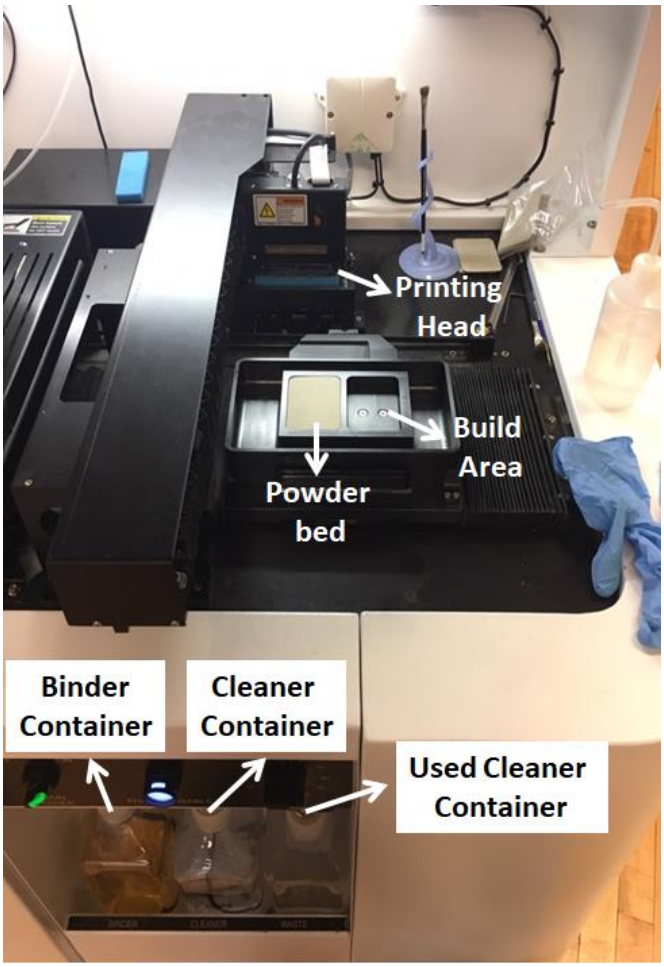

Figure 1.6: Working space of the binder jetting printer used in this research.

A rotating cylindrical roller spreads a layer of powder from the powder bed onto the build area. Then, the print head deposits binder on selected areas accordingly to the CAD file

design. As the plate from the build is dropped down, a new layer is created and again the binder is deposited. This process repeats until last layer of the part is crated.

This method allows creating functional parts with complex shapes. An explored application is the manufacturing of permanent magnets that can be used for eletromechanical purposes. Production of bonded magnet parts consist in mixing magnet powders and exploring shapes as well as post processing techniques that enhance mechanical properties and preserves or even enhances magnetic properties.

Near-net-shape NdFeB bonded magnets produced via binder jetting is an example of bonded magnets that can be manufactured with no processing-induced degradation and with a density of 46% [31].

In this work, lattice structures have been manufactured by binder jetting from NiMnGa ball milled powders, in order to investigate the process capability to obtain parts with bimodal porosity and enhanced mechanical and functional (magnetic shape memory effect) properties.

1.5. AM using Selective Laser Melting Process

The main advantage of the selective laser melting (SLM) method is in producing metallic fully dense parts. SLM produced parts produced in this work were used in compressive testing to validate the mechanical behavior predicted by the computer modeling performed using finite element analysis (FEA).

After a layer of powder is deposited on the build plate and a wiper blade spreads the powder uniformly, an ytterbium fiber laser scans the CAD pattern melting the powder together. Then, a new layer of powder is spread and the process continues forming the structure. The whole process takes place under argon atmosphere in order to avoid oxidation of produced parts. This process involves large thermal gradient and creates non-equilibrium phases due to the high localized heat input from the laser beam. Thus, although parts produced present a satisfactory finishing, post heat treatments are usually performed to promote stress relieving [32].

Use of laser for AM makes processing parameters a direct interference on the quality of produced parts. Parameters that are explored include laser power, layer thickness, laser scanning speed, and hatch spacing. Pore formation, which directly impacts on the density of the part, is influenced in the SLM process by hatch spacing. Distances greater than beam spot size leads to the creation of pores[33]. Moreover, hatch spacing influences the surface quality of produced parts due to the heat and mass transfer within the molten pool created by the presence of surface tension. Thermal accumulation can be reduced by increasing hatch spacing since the temperature gradient of the molten liquid is reduced [34].

Thermodynamic behavior of molten pool created by the laser beam and powder interaction are governed by the mass, momentum and energy conservation equations based on the density ρ, thermal conductivity κ, dynamic viscosity μ, pressure p, temperature gradient ∇T that is distributed along coordinates X, Y, and Z, motion velocity of the melt $\vec{V}$, mass source M_s, body force $\vec{F}$, and the source of energy term S_H [33]:

$$\frac{\partial \rho}{\partial t} + \frac{\partial(\rho u)}{\partial X} + \frac{\partial(\rho v)}{\partial Y} + \frac{\partial(\rho w)}{\partial Z} = 0 \quad (14)$$

$$\rho\left(\frac{\partial \vec{V}}{\partial t} + \vec{V} \cdot \nabla\vec{V}\right) = \mu\nabla^2\vec{V} - \nabla p\vec{V} + M_s \cdot \vec{V} + F \quad (15)$$

$$\rho\left(\frac{\partial \vec{V}}{\partial t} + \vec{V} \cdot \nabla T\right) = \nabla \cdot (\kappa \nabla T) + S_H \quad (16)$$

$$S_H = -\rho\left(\frac{\partial}{\partial t}\Delta H + \nabla \cdot \left(\vec{V}\Delta H\right)\right) \quad (17)$$

1.6. Purpose

Lattice structures present the combination of reduced weight and increased efficiency. By repeating a unit cell, these periodic structures deliver functional parts of lightweight nature with superior structural characteristics and minimal material.

The purpose of this study is to create, explore, and optimize truss architectures of unit cells to be used in lattice structures in order to tailor mechanical properties. Analysis of the mechanical behavior of the base level patterns is essential in order to visualize the responses, which depend on each different design. In order to optimize the lattice structured materials, the constraints need to be identified and avoided.

This work investigates two types of lattice structures. The first one is bend dominated structures with applications in mechanical energy dumping/absorption. The second type are stretch dominated lattice structures with enhanced strength and stiffness properties used for structural load bearing.

The approach of this study is based on experimental investigation and modeling by finite element analysis (FEA) in order to determine the mechanical behavior of lattice structured materials. Numerical analysis of compressive loaded unit cells is used to assess the efficiency of each design. The optimized design will be used in 3D printing of NiMnGa lattice structures. The goal is to manufacture parts from NiMnGa MSMAs displaying improved mechanical and functional characteristics.

It must be noted that for modeling purpose the strut on the lattice structure was made of 100% dense material. However, in the case of lattice structure manufactured by binder jetting the strut is not 100% dense, due to the nature of the technique. Therefore, in order

to assess the validity of FEA, cellular structures with fully dense struts have to be use. For this purpose, similar lattice structures have been manufactured from Inconel 718 powders using selective laser melting (SLM). The Inconel 718 powder was selected since was available in large enough quantities to be used in additive manufacturing process using selective laser melting technique. The SLM technique was employed since, different than binder jetting, produces lattice structures with fully dense struts.

Chapter 2 – Experimental Methods

2.1 Lattices Design and Manufacturing Process

Four different lattice structures were designed to investigate the deforming mechanism and determine the mechanical properties. Starting with a reduced amount of struts, each geometry was changed by gradually increasing the struts and connections in order to obtain a stiffer and stronger part resembling truss structures.

Geometries shown in Figure 2.1 were created using SolidWorks. The rectangular parallelepiped dimensions are 5 mmx5 mmx10 mm, with top and bottom plates of 0.5 mm thickness, and struts of 0.5 mm diameter.

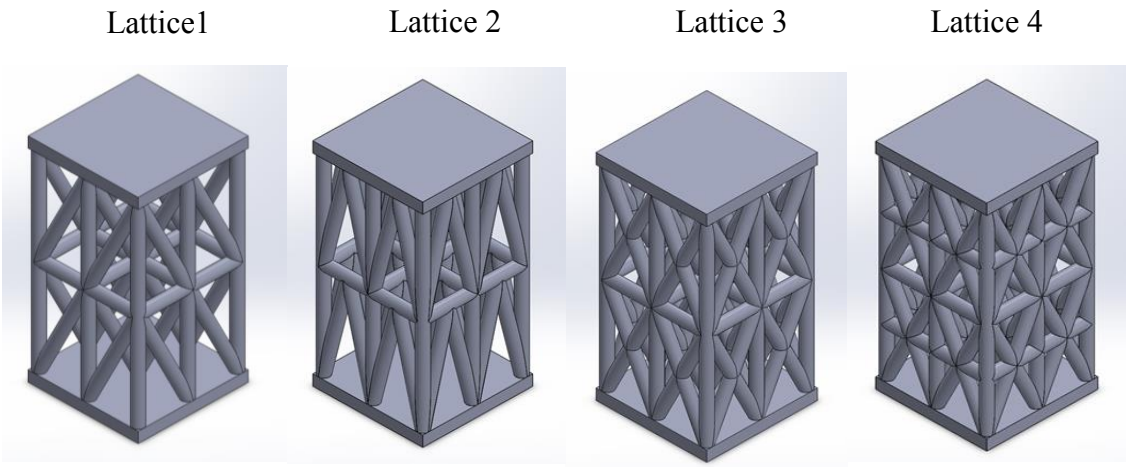

Figure 2.1: Lattice structures.

Designing unit cells with increased transverse struts is an optimization method to make them carry tension and increase stiffness. Geometries files were converted into STL files, to be used for printing the parts.

Initially, the lattices were built with Inconel 718 by selective laser melting in order to validate the FEA modeling.

The machine used for the SLM printing was a ProX 320 DMP from 3D Systems located at America Makes, Figure 2.2.

Figure 2.2: Selective laser melting machine used for printing of Inconel 718 parts.

The laser parameters used were laser power 180 W with a scanning speed of 900 mm/s. Inconel 718 powder was made by argon gas atomization and purchased from Praxair Inc. The layer thickness was 30 μm and the melting was performed under argon atmosphere in order to avoid oxidation of manufactured structures. The 3D printed samples were wire cut using an electro discharge machining process, in order to be removed from the build plate. The printed parts are shown in Figure 2.3.

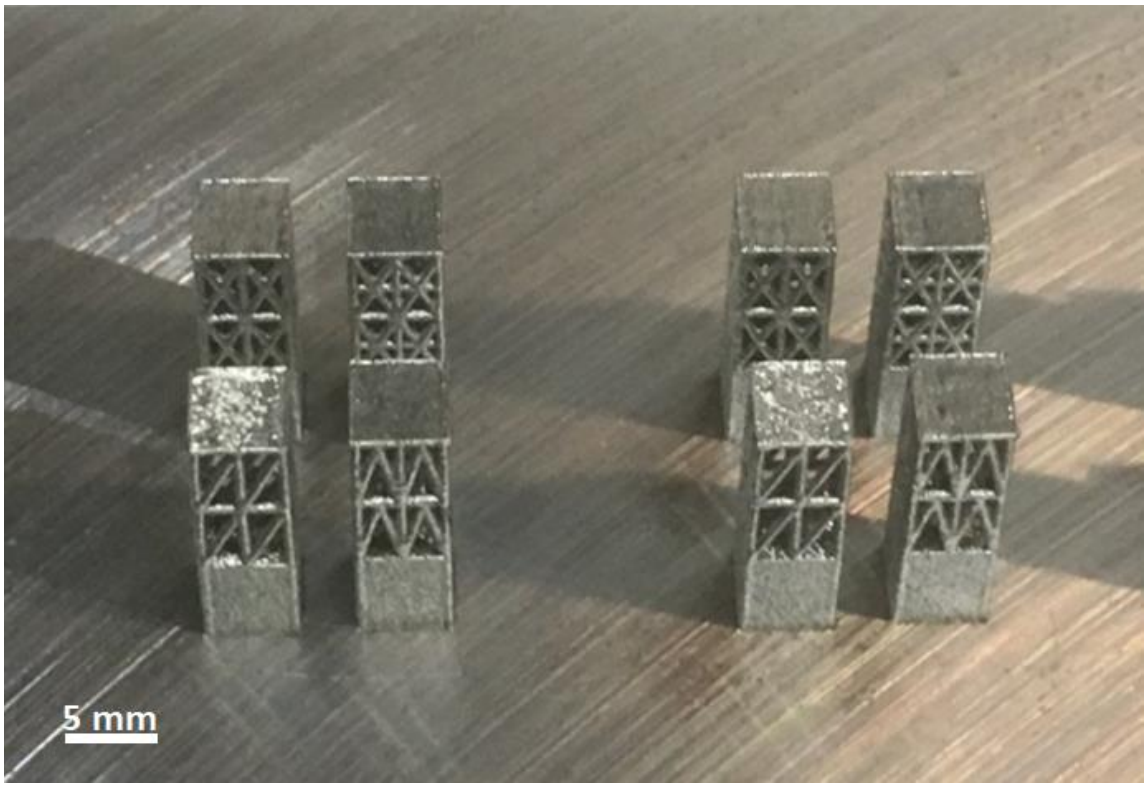

Figure 2.3: Inconel 718 lattices printed on the built plate.

Due to the fact that the parts were built onto a plate, it was needed to create a 5mm base to ensure that the lattices dimensions were preserved during the SLM process. The sizes of the samples were small enough and no fixtures were required to be designed for this printing process. After printing, the base was removed using Buehler IsoMet 1000

precision cutter and both bottom and top surfaces were polished to ensure parallel and smooth surfaces required to perform a uniform uniaxial compressive testing, Figure 2.4.

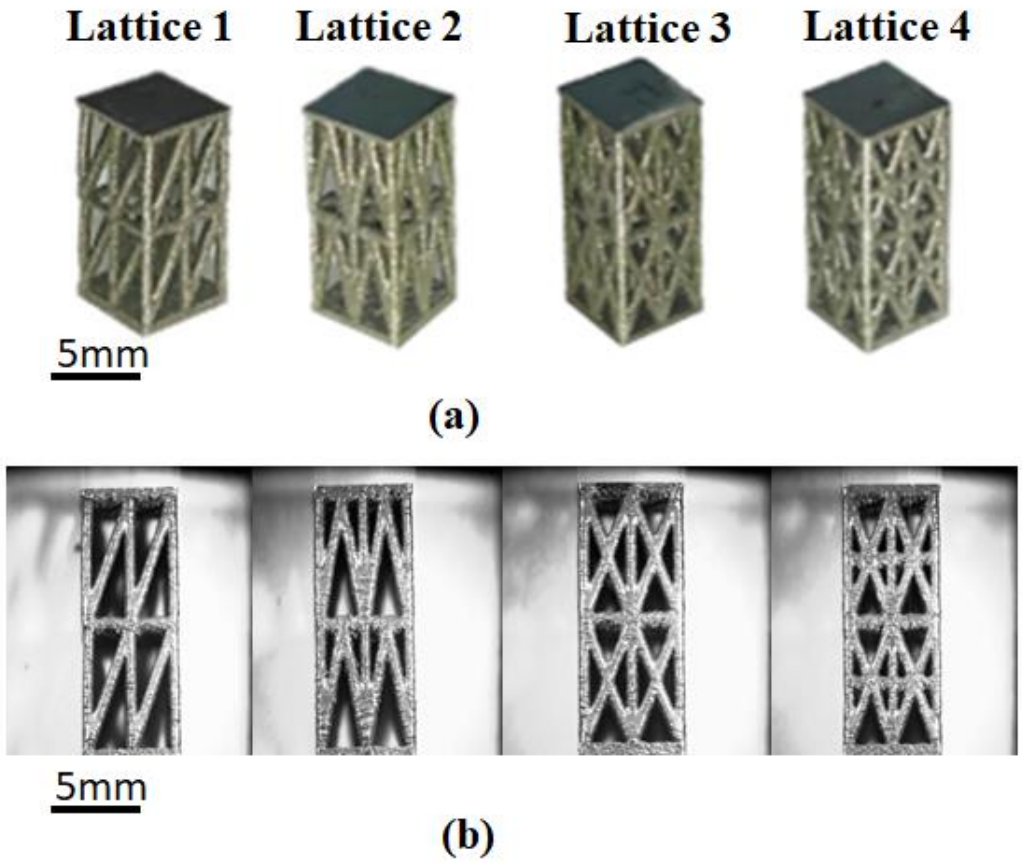

Figure 2.4: (a) Inconel 718 lattice structures after the base was removed and top and bottom surfaces polished; (b) Front view images of Inconel 718 lattice structures.

Most of the SLM printed samples were mechanical tested in as-printed state. A set of four samples, one from each design, were encapsulated in a quartz tube filled with argon gas and annealed at 1000°C for 17h, followed by slow cooling in the furnace in order to remove internal stresses. The annealing temperature was selected based on the optimal microstructure homogenization process described for Inconel 718 specimens manufactured via SLM with maximum laser power of 100 W [32].

Using binder jetting method, the four designed lattice structures were printed using NiMnGa powder produced at YSU. Elemental Ni, Mn, and Ga of high purity (99.99%) were melted together in an arc melting furnace, under argon atmosphere, to prepare NiMnGa (49.73 at% Ni - 29.03 at% Mn - 21.24 at% Ga) alloy buttons. The process is presented in Figure 2.5.

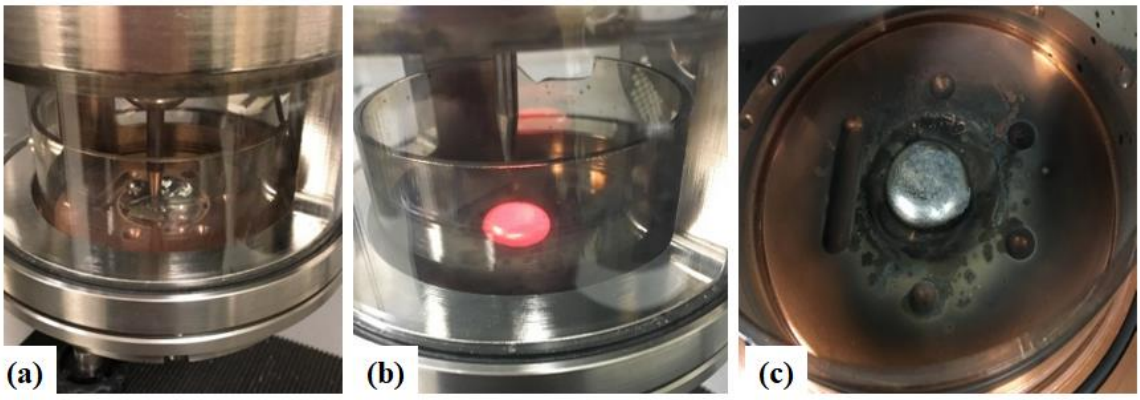

Figure 2.5: (a) Elemental metals in the melting chamber; (b) Arc melting of NiMnGa alloy; (c) Ingot of NiMnGa.

The ingots were encapsulated in quartz tube under argon and underwent heat treatment of 1020 °C for 16h to promote homogenization. Following the homogenization heat treatment, the buttons were grinded into NiMnGa prealloyed powders by ball milling. The half-ingots and the ball milling machine are shown in Figure 2.6.

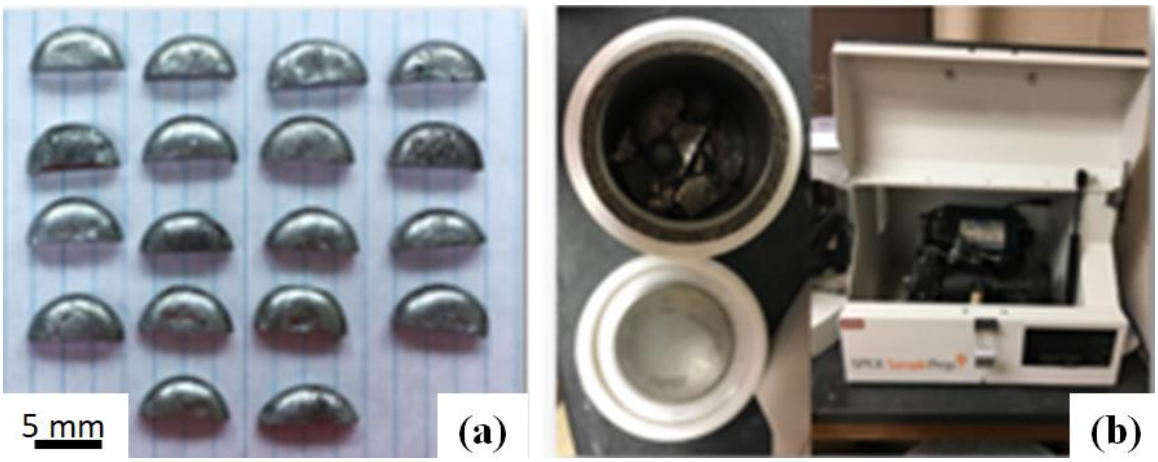

Figure 2.6: (a) NiMnGa ingots; (b) Ball milling process.

After particle size distribution analysis, the powders were acceptable to be used in the printer. Then, the lattices made of NiMnGa were 3D printed with the X1-Lab 3-D from ExOne machine shown in figure 2.7 below. The layer thickness used for this process was of 110 μm.

Figure 2.7: Binder-jetting 3D printer at YSU.

The as built parts were placed in a quartz tube under argon. The parts were sintered at 1020ºC for 16h. Figure 2.8 shows the NiMnGa lattices after the sintering process.

In order to calculate the experimental strain, the sintered parts were measured using a caliper. For this case, the use of extensometers to determine the strain was not possible due to the small scale of the samples. The most appropriate method to use for this situation would be digital image correlation. However, it is not available at YSU.

Weight was also determined for each part in order to calculate the relative density and porosity of the lattices.

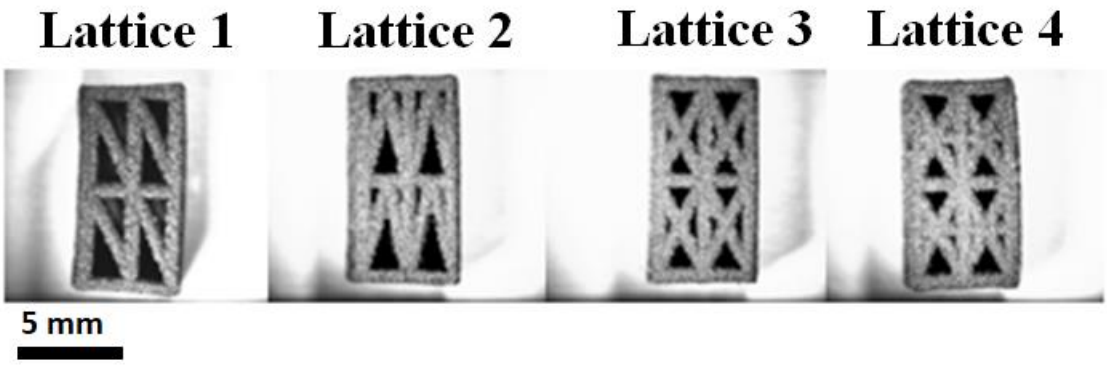

Figure 2.8: NiMnGa optical microscope images – front view.

The sintered samples were compressed using Instron Machine 5500R using a load cell of 150kN, Figure 2.9. A strain rate of 0.5mm/min was employed for the compressive testing.

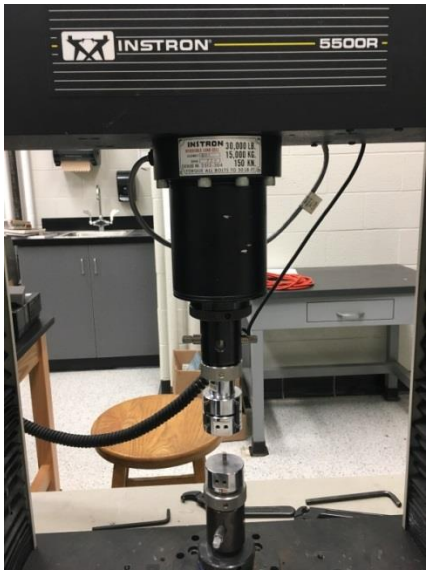

Figure 2.9: Instron machine used for compressive testing.

The curves obtained were load, in Newton, vs. extension, in millimeter. Photographs were taken at extensions from 0 to 3 mm at each 0.5 mm for Inconel 718 samples. On the other hand, for samples made of NiMnGa, photographs were taken at extension from 0 to 1.5 mm at each 0.5 mm. The use of photographs helps to compare the deformation behavior between the different lattices as well as to observe the collapse mechanism for each geometry.

Mechanical properties and stress-strain relationships of tested samples were obtained based on the load and displacement of the compressor moving crosshead. Stress-strain curves were created from the load vs. extension where the strain was calculated from:

$$\varepsilon = \frac{\Delta L}{L} \tag{18}$$

With L as the initial height of the lattice structure, measured for each tested sample using a caliper, and with ΔL as the extension given by the software that corresponds to the displacement of the compressor head.

The stress was calculated based on the following formula:

$$\sigma = \frac{F}{A} \tag{19}$$

Where F is the load displayed from the software and A is the area of the cross section of the struts normal to the top plate. For each sample, the measurements were taken using the geometry from SolidWorks.

The compressive testing was performed for the following samples: six samples of each geometry from Inconel 718 as built, one sample of each geometry from Inconel 718 heat treated, and one sample of each geometry from NiMnGa.

Materials characterization included powders size distribution analysis, scanning electron microscopy, chemical composition investigation, differential scanning calorimetry, and optical microscopy.

Powder size analysis was performed using a CILAS 1064 instrument. A scanning electron microscopy (SEM) equipped with X-ray energy dispersive spectrometer (XEDS) was used to investigate the morphology and chemical composition of metallic powders used in AM, and printed parts. SEM and optical microscope were also employed to perform a failure analysis of some compressed samples. The electron microscope used in this work was the JEOL JSM7600F Scanning Electron Microscope equipped with the EDAX Octane Plus X-ray Energy Dispersive Spectrometer. Differential scanning

calorimetry was employed to ensure that after heat treatment, lattices structures made of NiMnGa still presented reversible martensitic transformation. For that, it was used the Diamond DSC from Perkin Elmer.

2.2 Finite Element Analysis (FEA)

The objective of using finite element analysis in this work was to map the maximum stress points at the struts on the structure as well as compare deformation behavior between numerical and experimental analysis. In this sense, it is possible to identify what differences in geometries creates better load distribution.

Initially, in order to create the geometry for the model, the CAD files of the samples were imported into ANSYS Workbench and a compressor was created on top of each lattice to serve as a driving displacement.

Simulation of compressive testing was performed by designing a compressor based on Saint Venant's Principle where the length was large enough to create a uniform stress distribution on the sample [36]. The geometry for the finite element model is shown in Figure 2.10.

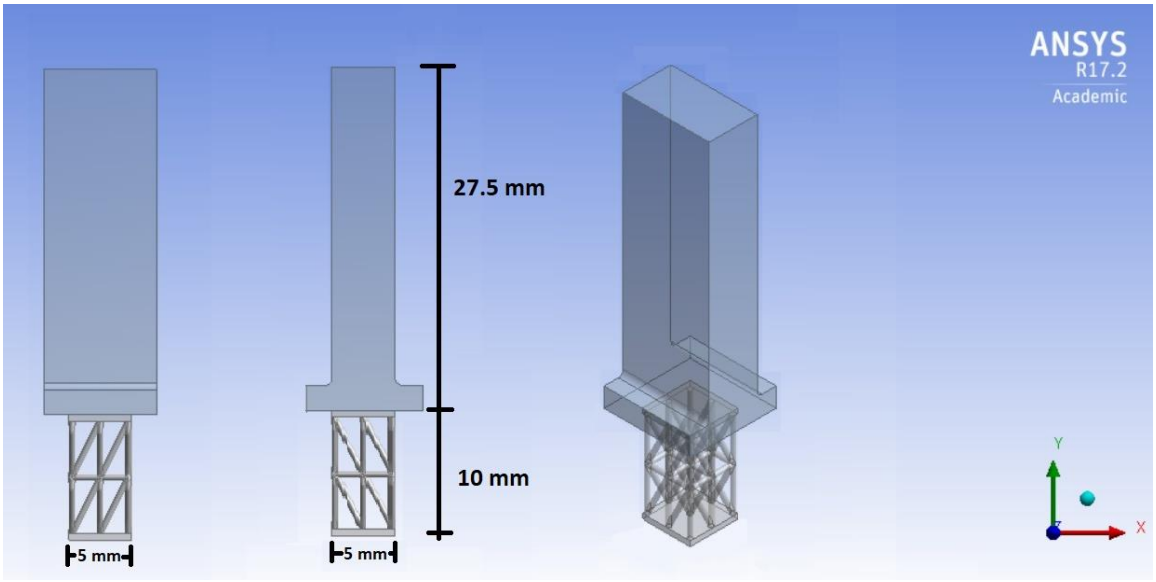

Figure 2.10: Lattice and compressor geometry.

Structural steel was the material used to model the compressor and the width of it was the same as the modeled sample, 5mm. However, because the samples are modeled with different material than the compressor, the lateral deformation is different for each material. In this case, the sample tends to deform more than the compressor, leading to a variation in the stress value between the sample and the compressor. Thus, the compressor head is designed wider at the sample interface in order to account for that difference.

Materials definition is based on two independent parameters: isotropic and orthotropic elasticity, where Young's modulus and Poisson's ratio are independent of direction.

Engineering data used for materials properties of Inconel 718 samples were obtained from literature [37].

The input properties input for the Inconel 718 lattices are shown in Figure 2.11.

Properties of Outline Row 3: Inconel 718

	A	B	C	D	E
1	Property	Value	Unit		
2	Density	8190	kg m^-3		
3	Isotropic Elasticity				
4	Derive from	Young's Modulus and Poisson's Ratio			
5	Young's Modulus	2.08E+11	Pa		
6	Poisson's Ratio	0.3			
7	Bulk Modulus	1.7333E+11	Pa		
8	Shear Modulus	8E+10	Pa		

Figure 2.11: Engineering data - Inconel 718.

On the other hand, Ni-Mn-Ga material properties were obtained from experimental results of bulk Ni-Mn-Ga determined in Eric Myers' thesis [38], where the material inputs were used for both bulk and AM models. The input properties for NiMnGa lattices are shown in Figure 2.12.

Properties of Outline Row 4: NiMnGa

	A	B	C	D	E
1	Property	Value	Unit		
2	Density	7602	kg m^-3		
3	Isotropic Elasticity				
4	Derive from	Young's Modulus and Poisson's Ratio			
5	Young's Modulus	1.6585E+10	Pa		
6	Poisson's Ratio	0.3			
7	Bulk Modulus	1.3821E+10	Pa		
8	Shear Modulus	6.3788E+09	Pa		
9	Superelasticit				
10	Sigma SAS	1.42E+08	Pa		
11	Sigma FAS	3.79E+08	Pa		
12	Sigma SSA	3.79E+08	Pa		
13	Sigma FSA	1.42E+08	Pa		
14	Epsilon	0.00366	m m^-1		
15	Alpha	0			

Figure 2.12: Engineering data for ANSYS Workbench - NiMnGa.

Material properties used for lattice models correspond to bulk materials, thus the results are proportional to the relative densities of the samples as explained in the beginning of this work.

Voids existent in the lattice samples of Inconel 718 and Ni-Mn-Ga contribute to the decrease of the mechanical integrity. It also leads to different mechanical properties than the bulk. Moreover, Ni-Mn-Ga samples printed using binder jetting 3D method present internal porosity which contributes even more to the difference in the properties between bulk and AM samples. Discontinues within the geometries create stress raisers or increase of stress along the struts due to the presence of sharp corners.

Similar boundary conditions were applied for all lattices with both Inconel 718 and Ni-Mn-Ga materials. They are shown in Figure 2.13.

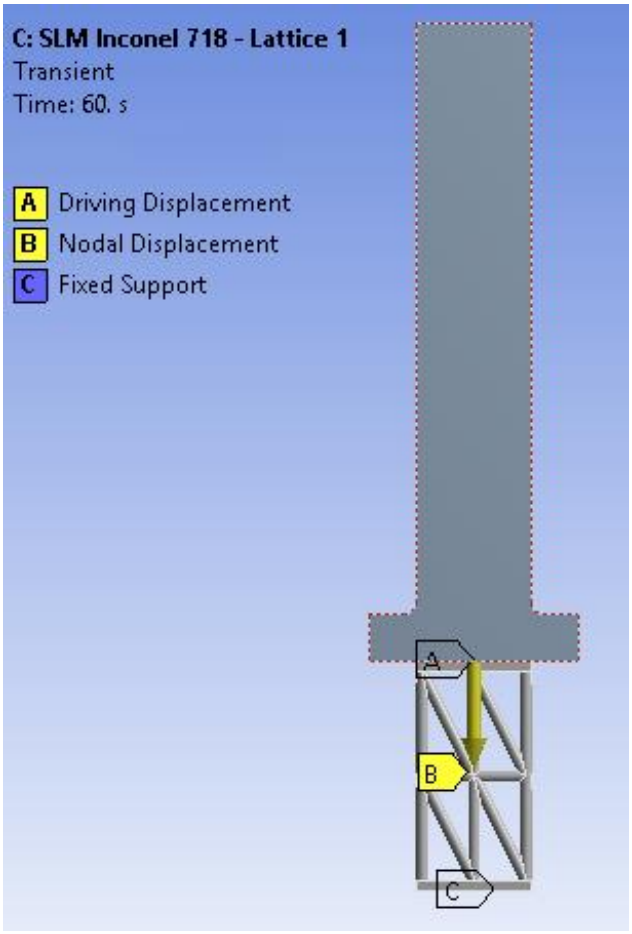

Figure 2.13: Boundary conditions.

The bottom plate was constrained as a fixed support (C). In a 2D analysis, a displacement in x, z direction would be used in the bottom of the sample. However, the same boundary condition when applied in the 3D case, allows the rotation of the sample when under the compressive load; thus the need of using a fixed support.

The compressor had a driving displacement (A) with 0.5 mm displaced in 60 seconds in order to simulate the experimental compressive testing under the same strain rate.

A named selection (B) was created in the center of the middle strut of each sample in order to constrain a node from the lattice giving stability to the model and to prevent rigid body motion in x and z directions.

Finally, the contact condition in between the compressor surface and the top plate surface of the lattice was a “no separation” as shown in Figure 2.14.

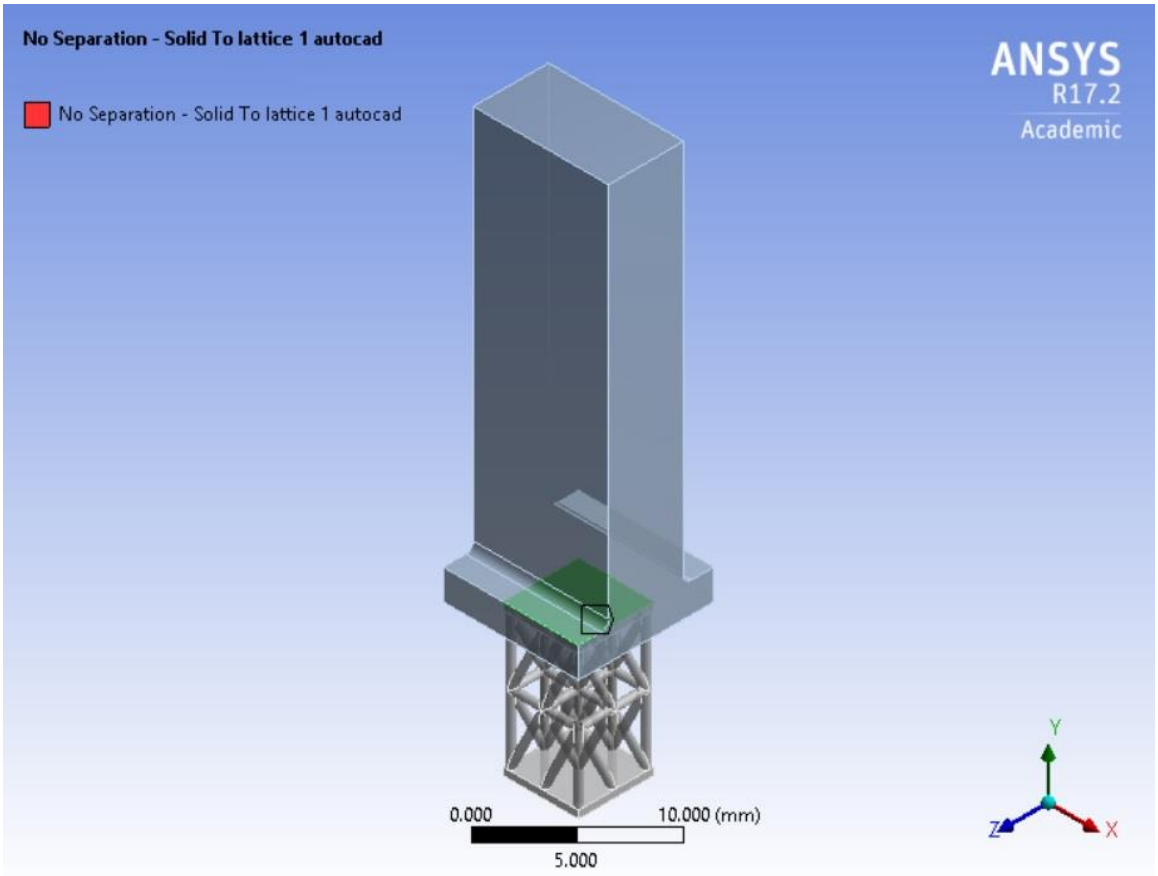

Figure 2.14: No separation contact condition between lattice and compressor.

This kind of separation allows the surfaces to slide relative to each other but constrains their separation in the normal direction.

Modeling of lattice structures in ANSYS Workbench was carried out performing compressive axial testing using transient structural simulation, where implicit integration method is used to calculate the dynamic response [39]. Governing equation of transient simulation is given by:

$$[M]\{\ddot{D}\} + [C]\{\dot{D}\} + [K]\{D\} = \{F\} \quad (20)$$

With $[M]$ as the mass matrix, $\{D\}$ as the nodal displacement vector, $[C]$ as damping matrix, $[K]$ as the stiffness matrix, and $\{F\}$ as the nodal external forces vector.

This is a model with multiple degrees of freedom described as an extension of the single degree of freedom for static case:

$$[K]\{D\} = \{F\} \quad (21)$$

Simulation of samples was performed using a nonlinear approach. For this study, the initial portion of the stress-strain curve response is considered linearly proportional to the load. The slope of the curve is constant in this case but cannot be described by Hooke's law because the model does not present elastic response and it is time-dependent. In this nonlinear problem, the principle of superposition is not applicable, and the compressive loading influences the solution.

A nonlinear simulation will then be described by:

$$[K(D)]\{D\} = \{F\} \quad (22)$$

Where the stiffness matrix $[K]$ in this case will be a function of the nodal displacement D instead of a constant matrix.

Sources of structural nonlinearity include large deformation due to geometry, change in between the contact of surfaces due topology or structural failure, and material non-linear stress-strain response.

The contact type “no separation”, applied between the samples and the compressor, only introduces small tangential sliding. In this case, it allows assuming the small displacement theory for the case. Thus, no contact nonlinearity is introduced in the model.

On the other hand, nonlinearity is introduced in the model due to geometry. The compressive load is responsible for creating a large deformation of the lattice structure, which induces a substantially change in the stiffness matrix [K]. The reason for that is because along with the geometry, the element stiffness matrices that compose the stiffness matrix [K] are a function of the material properties.

It is important in this case to include the geometry nonlinearity. For that, the large deflection was turned on in the details of “Analysis Settings”. Also, the convergence was improved by reducing the time steps necessary to solve the analysis.

The last aspect to be discussed in this chapter is the mesh of the geometries in the model. In real world problems, it is difficult to stablish governing equations directly from deformation behaviors. The use of finite element methods is then explored by dividing the entire geometric model into finite elements, which are geometrically simpler shapes connected within each other by nodes. In this case, each element is described by a governing equation that leads to a system of equations that are solved simultaneously. With this approach, a large complex geometric shape can be mathematically represented

by dividing the whole element into a high amount of smaller cells, which is inviable theoretically. The division of the geometric model into finite elements consists on the creation of the mesh.

The quality of the finite element model depends then on the division of the model into the elements, which is called meshing. Along with the environment conditions, the mesh characterizes the analysis and it is essential in the convergence of the nonlinear solution.

Different mesh manipulations are possible in order to create an accurate model. The number and the shape of the finite elements are a challenging determination and influences on a more efficient model.

The convergence test is a method used to refine the mesh continuously. Initially, a lower quality mesh is used to run the simulation. Then, a higher quality mesh, with more elements, is created for the same analysis and the simulation is performed again. These steps are continuously repeated. For each simulation ran, the results are observed. The convergence is stablished whenever the models present close values between one mesh and the other.

Since the governing equations are stablished for each element in the model, the system of equations is solved within the nodes of the elements. Due to the fact that the elements share faces, edges, and nodes, their stress state contributes to an average of the effects of all them together. The refinement of the nodes by increasing the number of elements in the model will then provide a capture of more details that could be neglected by using a poor mesh. Thus, it is important to create a refined mesh in particular locations within the model where geometric details are crucial for the stress response in the part.

The second factor that influences on the model simulation is the shape of the finite elements. Some shapes are definitely more efficient than others. Considering a 2D geometry simulation, the shape of the elements can be triangles or squares. This work, however, is a 3D geometry simulation and in this case, the possible shapes are tetrahedrons, prisms, pyramids, or hexahedrons.

The more efficient shapes are the ones that present more faces and nodes since this will contribute for higher interface connections in between the elements leading to a more accurate simulation. Then, in this study, the meshes were created to present as many hexahedra shape elements as possible in order to better represent the lattices structures.

In general, a mesh with tetrahedral elements is generated more easily due to the less refinement required to create them. However, it is important to create the model with a mesh containing higher nodes and faces elements where the accuracy will be improved, and the solution converged.

Sometimes refining the elements by increasing the number of finite elements or by exploring the shape of the elements within the mesh is not enough to assure that the model delivers a good quality simulation. In order to the nonlinear simulation converge it is necessary to have a good quality of mesh. Thus, mesh refinement is not a synonym of an acceptable mesh quality.

The quality of the mesh is given by the mesh metric called skewness and by the orthogonality feature. Both quality features are available in ANSYS Meshing and provide a good estimative of the mesh aspect for the studied geometries. These two criteria were used to evaluate the lattices geometries explored in this work.

Skewness of the finite elements is determined based on the equilateral volume deviation and on the normalized angle deviation.

The meshes created for the lattice structures present both tetrahedral and hexahedra elements, but the equilateral volume only takes into account the tetrahedrons elements. After determination of the number of actual tetrahedrons cell sizes, an error percentage is calculated based on the optimal tetrahedrons cell size desired for those elements. In this case, the skewness will be given by:

$$Skewness = \frac{optimal\ cell\ size - cell\ size}{optimal\ cell\ size} \tag{23}$$

Analysis of the hexahedra elements are performed by considering the normalized angle deviation. These elements present a 90º angle face and the skewness is calculated based on the ratio of difference between maximum and the angle face:

$$Skewness = max\left[\frac{\theta_{max} - 90}{180° - 90}, \frac{90 - \theta_{max}}{90}\right] \tag{24}$$

Based on these two different parameters to measure the skewness, the final skewness is given by the bar chart of the number of elements vs. element metrics. The element metrics vary from 0 to 1, where 0 represents an excellent mesh and 1 represents an unacceptable mesh, based on Ozen Engineering[40] recommendations.

Figure 2.15 shows the skewness of the lattice 1 used for this work simulation. Ideally, skewness below 0.94 is acceptable but reduction of element metrics is always better to make the solution converge. Another mesh quality measurement is the orthogonality. This feature measures the on cell vector (from the centroid of the cell to the one of the

face or from the centroid of the cell to the one of the adjacent cell) and the on face vector (from the centroid of the face to the one of the edge).

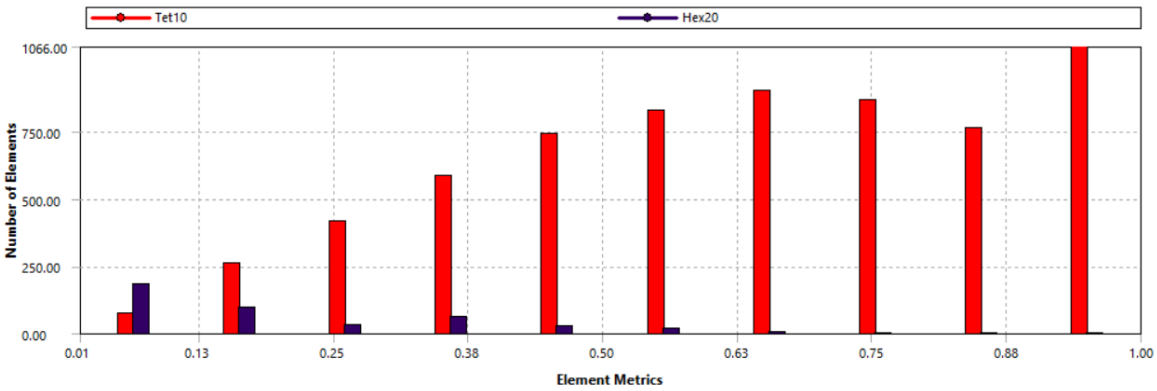

Figure 2.15: Skewness – lattice 1- mesh quality

Similarly to the skewness, the orthogonality element metrics vary from 0 to 1. However, now 0 represents an unacceptable mesh and 1 represents an excellent mesh based on Ozen Engineering recommendations [40]. Figure 2.16 shows the orthogonality of the lattice 1 used for this work simulation.

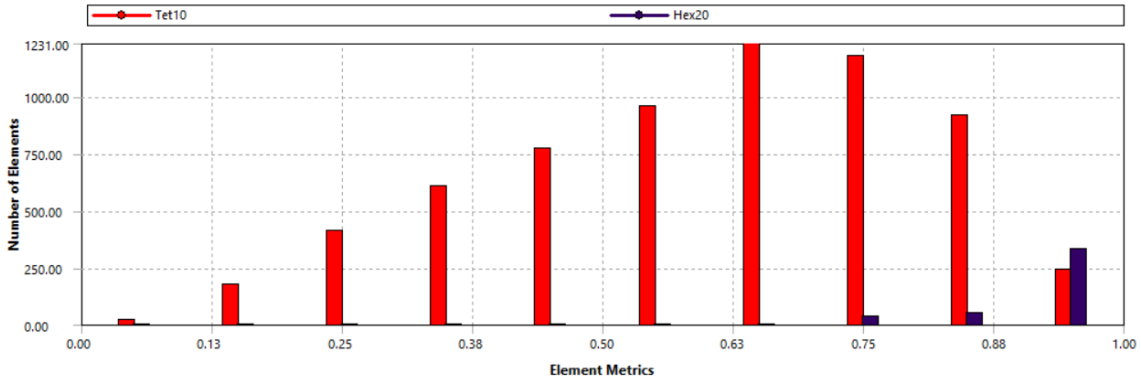

Figure 2.16: Orthogonality – lattice 1 - mesh quality.

Chapter 3 – Results and Discussion

3.1 Powder Characterization

3.1.1 Inconel 718

Powder size distribution was performed using CILAS machine. Inconel 718 powders obtained from Praxair Inc. and gas atomized under argon presented a homogeneous and normal distribution with mean powder diameter of 31.46 µm. Figure 3.1 shows the particle size distribution for the Inconel 718.

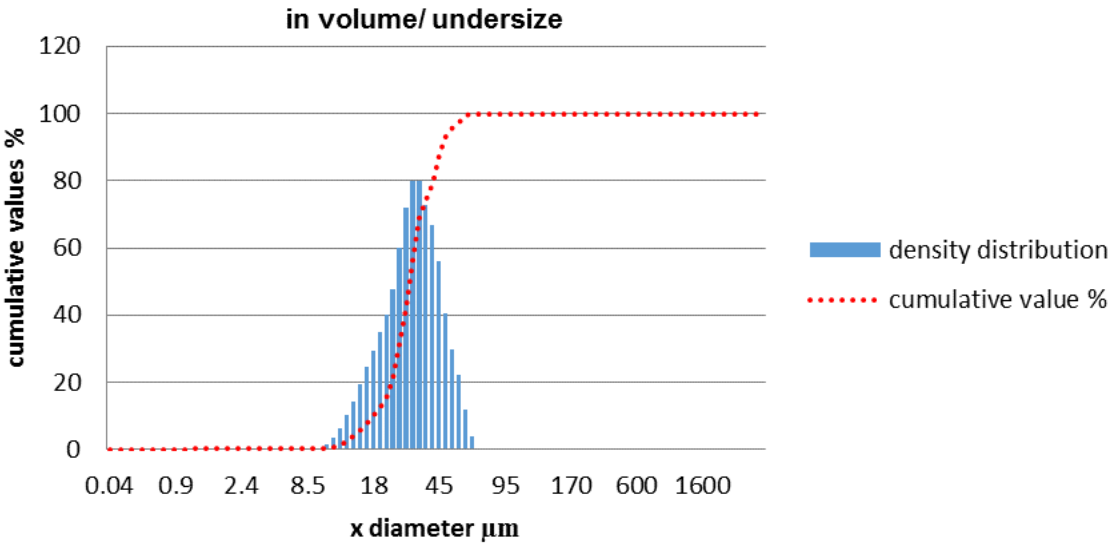

Figure 3.1: Powder size distribution – Inconel 718.

The morphology of Inconel 718 powders used in this work were investigated by SEM. Figure 3.2 (a) shows a low magnification backscatter electron (BSE) micrograph of the Inconel 718 powders, while Figure 3.2(b) shows an BSE micrograph of an individual particle.

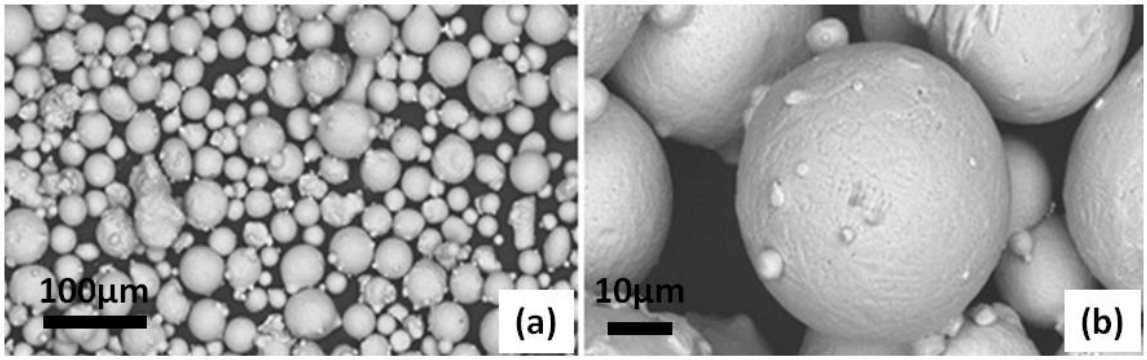

Figure 3.2: Backscattered electron micrographs (BSE) of Inconel 718 powders: (a) Low magnification micrograph showing the uniform spherical morphology of the powders; (b) Higher magnification micrograph of individual particle.

It can be inferred from the images that the powders present rounded or spherical shapes with a homogeneous size distribution. Irregular shaped particles with a similar chemical composition were observed to be attached to the main spherical shapes. The powders have uniform chemical composition as indicated by XEDS chemical analysis, Figure 3.3.

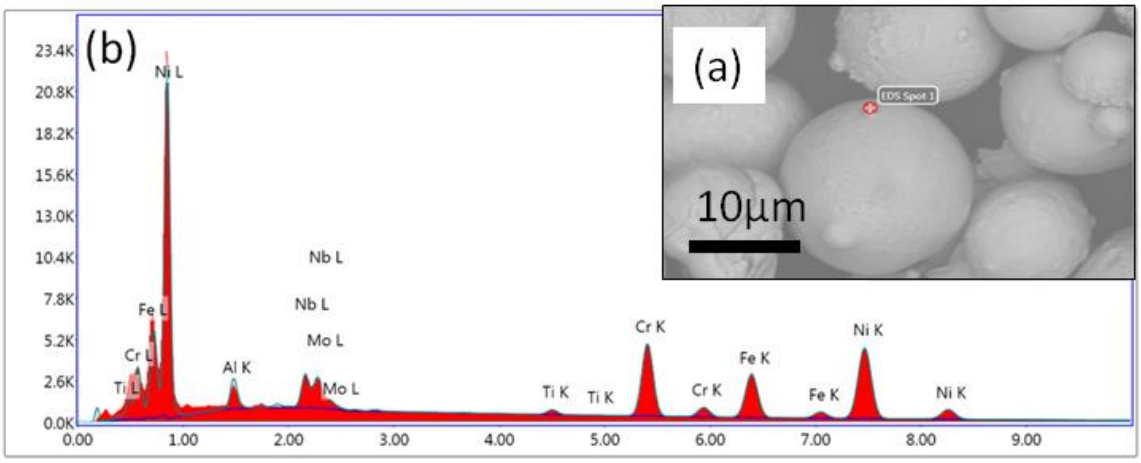

Figure 3.3: Chemical investigation of Inconel 718 powders using XEDS analysis. (a) Electron micrograph of the surface from which the XEDS spectrum was collected; (b) Corresponding XEDS spectrum.

3.1.2 NiMnGa

Particle size distribution of ball milled NiMnGa powder used for binder jetting is presented in Figure 3.4.

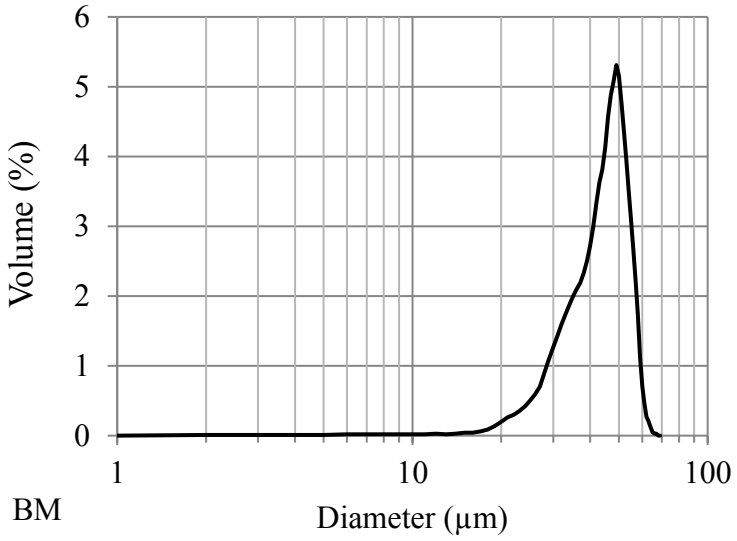

Figure 3.4: Powder size distribution – NiMnGa powders.

For this case, the results show a normal distribution with a mean powder diameter of 43.75 μm.

SEM of ball milled NiMnGa material reveals the uniform morphology of irregular shaped powders, Figure 3.5.

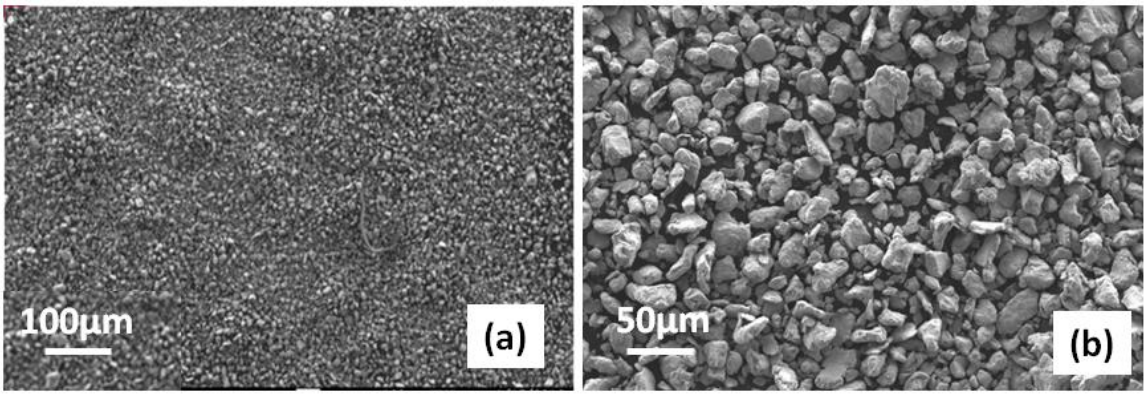

Figure 3.5: NiMnGa powders: (a) Low magnification micrograph showing the uniform morphology of the powders; (b) Higher magnification micrograph of irregular shaped individual particles.

XEDS of the NiMnGa powders is shown in Figure 3.6 and reveals a powder composition similar to the initial composition used to create the ingots.

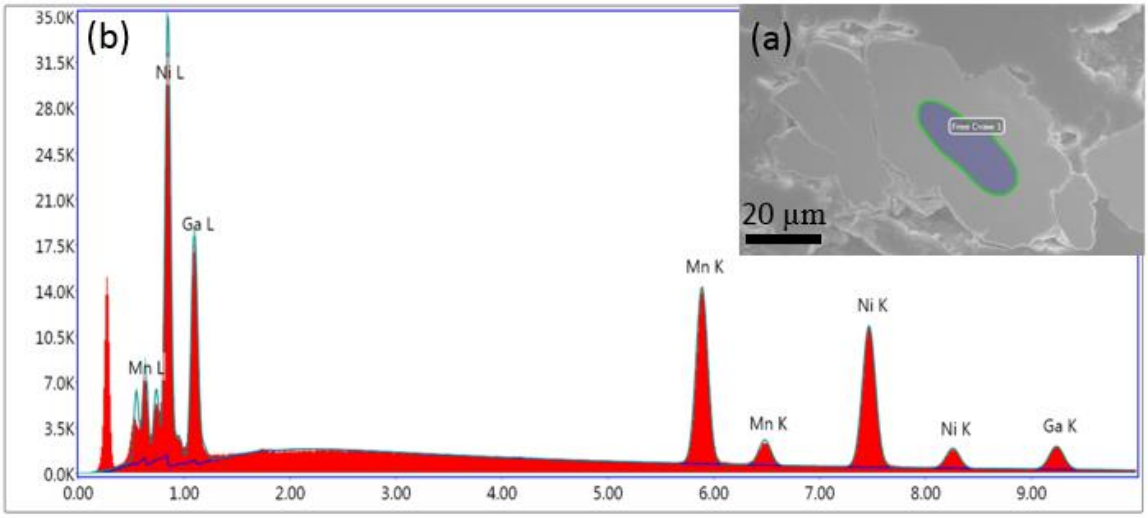

Figure 3.6: Chemical investigation of NiMnGa powders using XEDS analysis. (a) Electron micrograph of the surface from which the XEDS spectrum was collected; (b) Corresponding XEDS spectrum.

3.2 Additive Manufactured Lattice Structures: Microstructural Aspects, Mechanical Properties, and Failure Analysis

3.2.1 Selective Laser Melting

Electron microscopy investigation of 3D printed Inconel 718 lattices was performed before they were submitted to compressive testing in order to evaluate the microstructure and chemical composition of printed material. Figure 3.7 shows some of the characteristics inherent to the SLM produced parts.

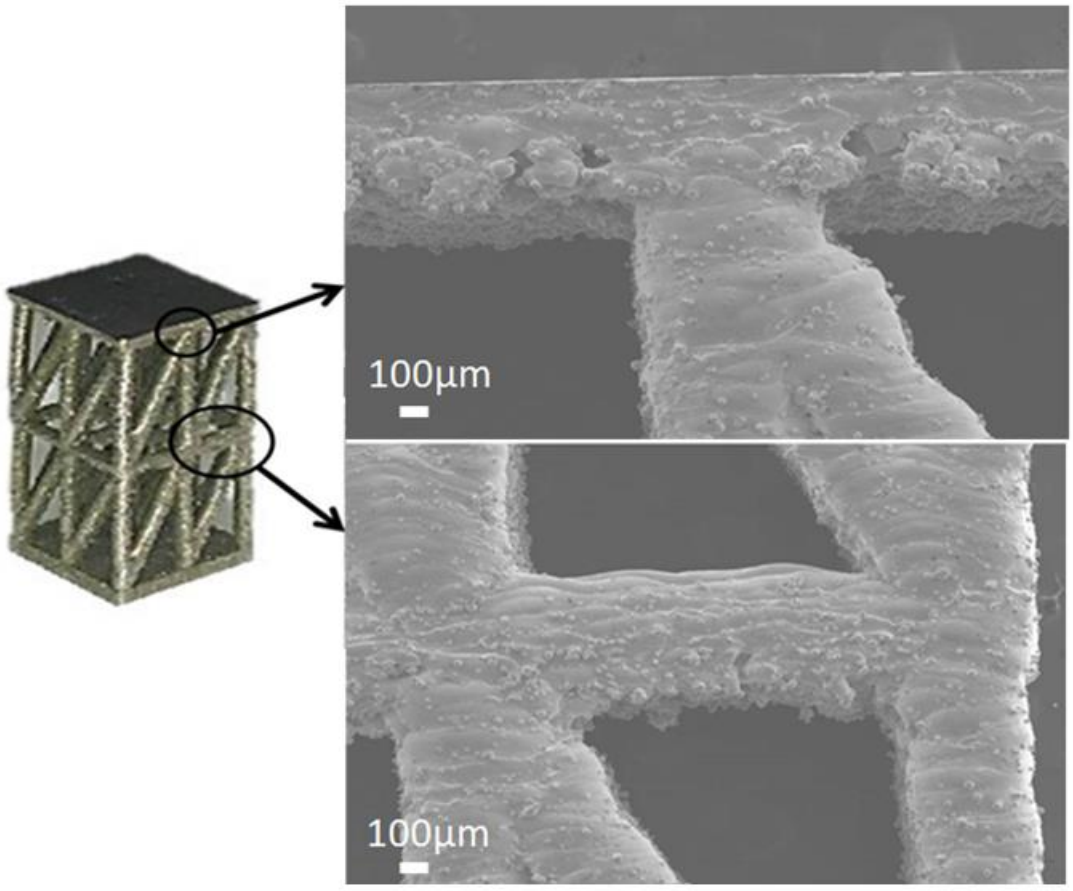

Figure 3.7: SEM – Lattice 1 Inconel 718 and some of the characteristics inherent to the SLM produced parts.

From the microscopy images, it is possible to visualize the printing layers produced by the laser during the SLM process. Observing the top horizontal strut, some level of porosity can be detected. A reason for that can be the lack of laser passes. In this case, it creates insufficient melting of the particles and a non-homogenous structure.

Sharp connections are observed at the nodes and they lead to stress concentration raisers. Struts off at 45°may cause maximum shear, and arched struts are justified by the lack of fixture during the printing process. Moreover, uneven cross section is present, where unmelted and partial melted powders are attached to surface. This creates an unsmooth surface with discontinued weld that can initiate the failure.

The chemical composition of the printed part was examined by XEDS, and no changes were observed compared to the staring powders. XEDS of the Inconel 718, Lattice 1 created by SLM process is shown in figure 3.8.

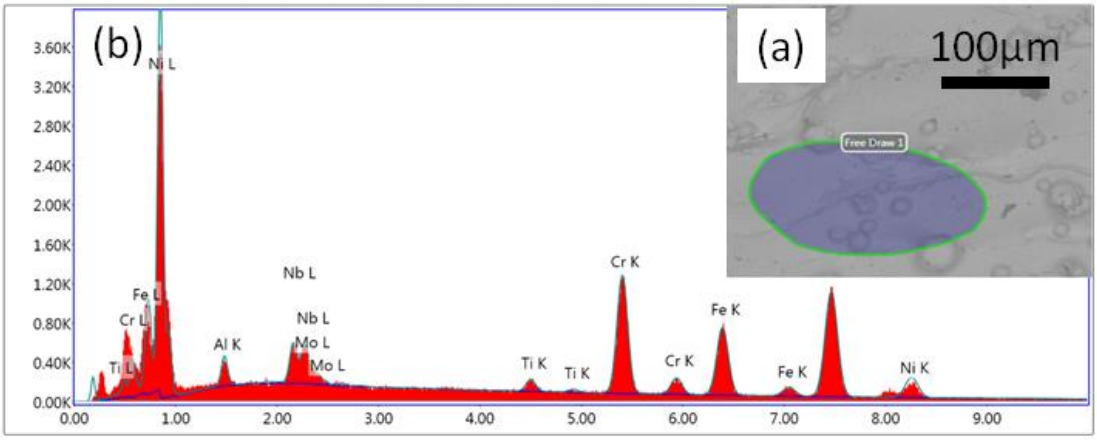

Figure 3.8: XEDS – Lattice 1 Inconel 718 (a) Electron micrograph of the surface from which the XEDS spectrum was collected; (b) Corresponding XEDS spectrum.

Chemical composition of Inconel 718 powder and that of printed part was compared to chemical composition of the material provided by literature[41]. Thus, the initial powder presents a satisfactory composition and the AM part showed similar composition to the powder, revealing that the SLM process occurred without chemical contamination.

After SLM printing, the top and bottom surfaces of the Inconel 718 lattices were polished, and the samples were measured and weighted in order to calculate their porosity. Table 3.1 presents the results for a batch of each lattice.

Table 3.1: Inconel 718 Lattices porosity levels.

	Porosity (%)
Lattice 1	74.3
Lattice 2	69.5
Lattice 3	66.8
Lattice 4	66.3

As expected, the increase of struts from lattice 1 until lattice 4 promotes a decrease in the porosity with the increase of the weight.

Measurement of porosity is important and it was used to stablish a relation between the relative density and the mechanical behavior of the lattice structures.

The failure analysis of compressed samples reveals the collapse mechanism characteristic for each type of geometry. Figure 3.9 shows the failure mode of samples from each lattice category.

Figure 3.9: Inconel 718 deformed lattices.

From the pictures taken after the compressive testing of the lattice structures, it can be seen that all, except for the Lattice 1 from the second batch, presented a similar collapse deformation behavior of the struts.

The reason why the Lattice 1 presented a different mechanism of collapse can be explained by the fact that before submitted to compressive axial loading, one of the struts in the structure was already bended. Thus, a different mechanism was created leading to an error of analysis.

An Inconel 718 part showing printing defects is presented in Figure 3.10. A bent strut is visible. Such a printing defect will decrease the mechanical strength of the part.

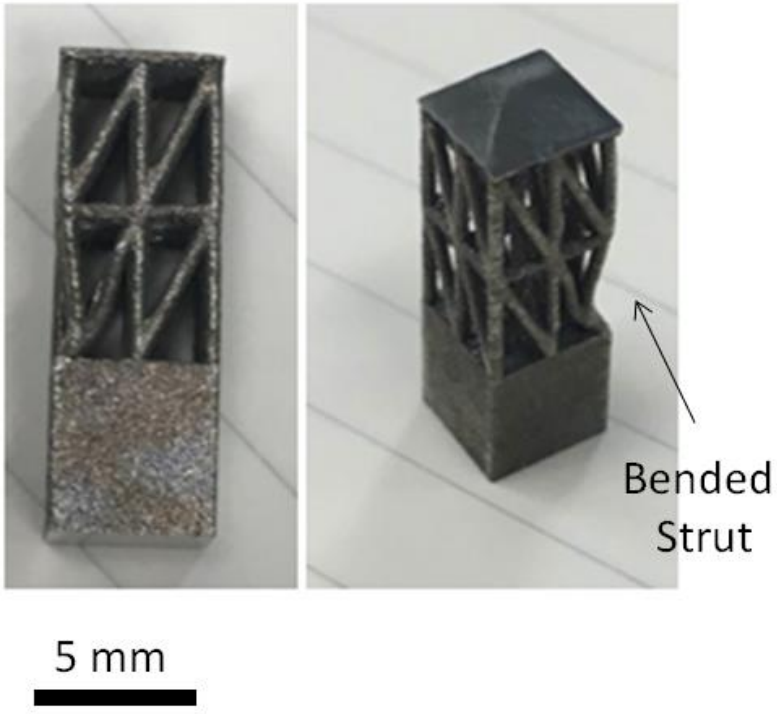

Figure 3.10: Inconel 718 lattice with bent strut before compressive testing – a possible printing defect.

Based on the load vs. extension raw data from Instron, the stress- strain curves for Inconel 718 lattices are shown in Figures 3.11 to 3.14, for lattices 1 to 4, respectively. HT stands for heat-treated sample.

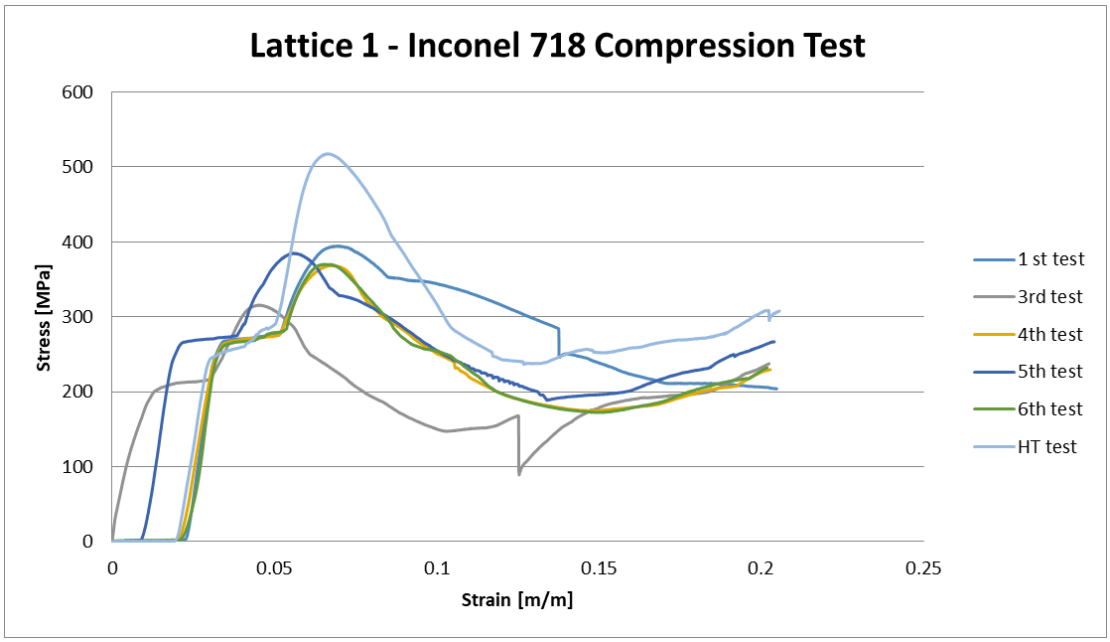

Figure 3.11: Stress-strain curves Lattice 1 Inconel 718.

The second test of the Inconel 718 Lattice 1 is not shown since it presents a very different behavior when compared to the others Lattices 1 samples. As stated before, this sample already had a bent strut and the compressive testing of it produced a stress-strain curve that cannot be compared with the curves from the others sample.

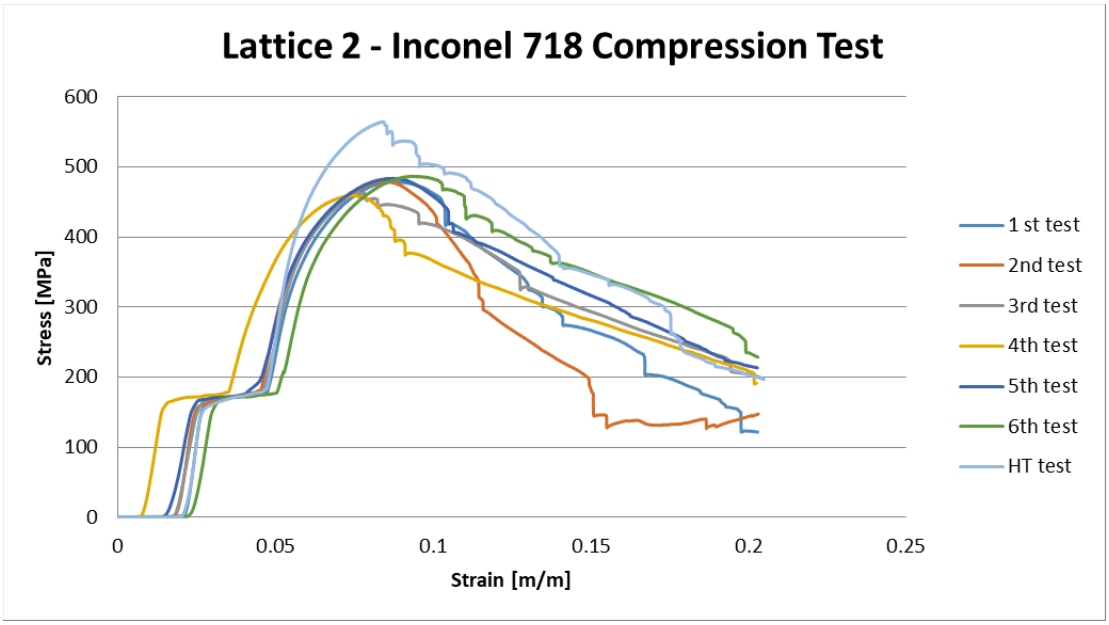

Figure 3.12: Stress-strain curves Lattice 2 Inconel 718.

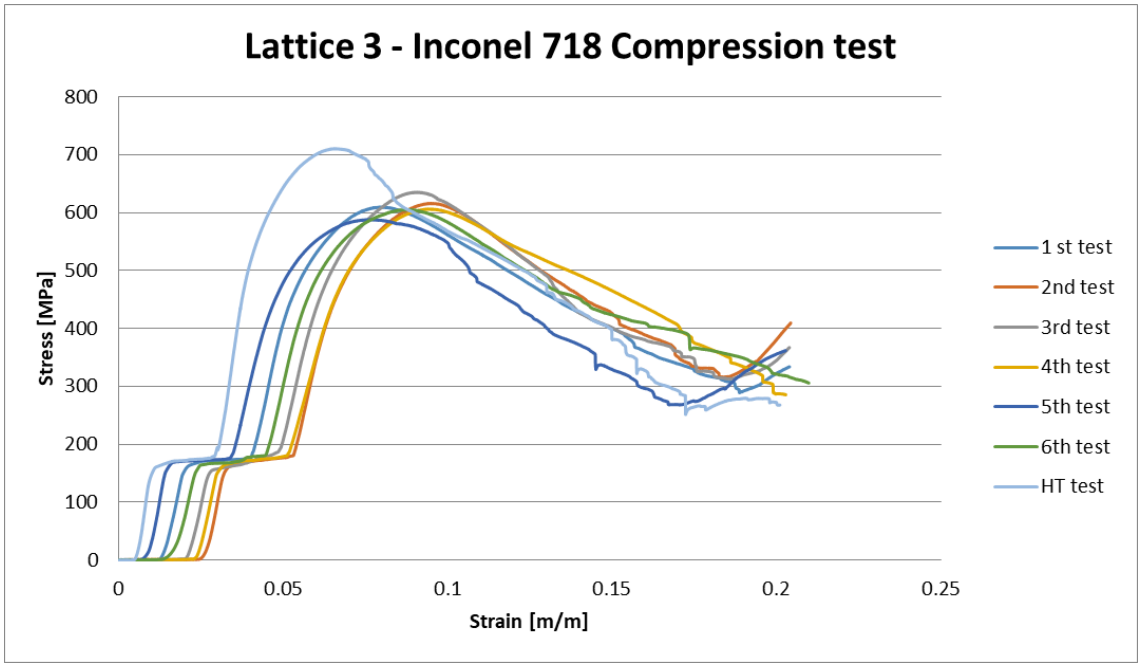

Figure 3.13: Stress-strain curves Lattice 3 Inconel 718.

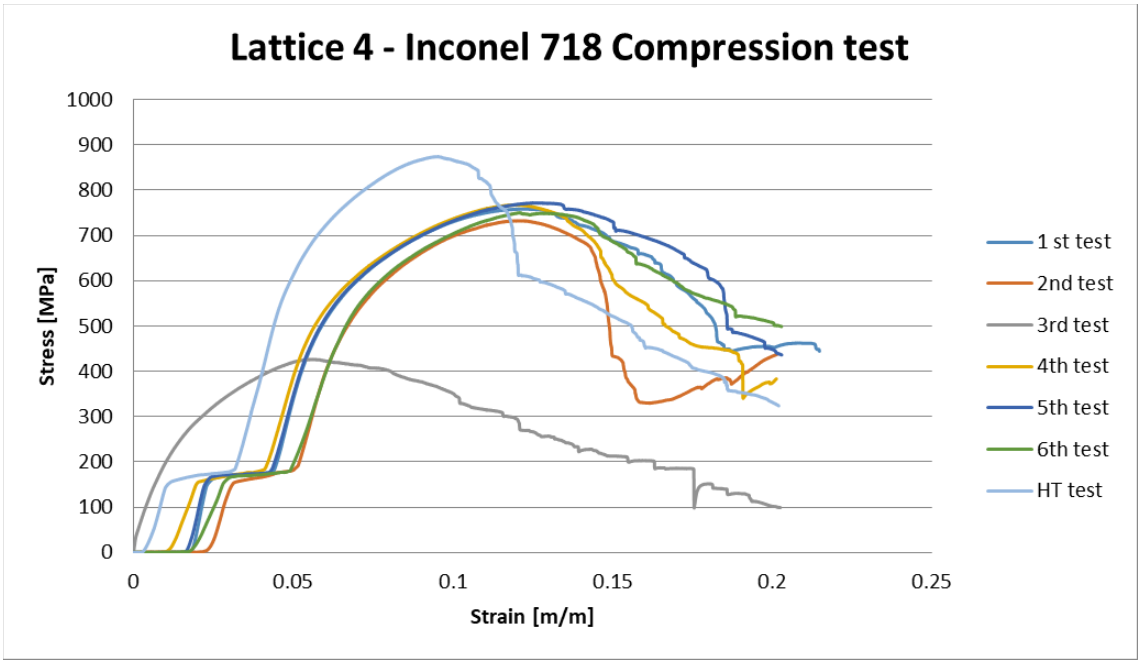

Figure 3.14: Stress-strain curves of Lattice 4 Inconel 718.

Considering Figure 3.14, analysis of stress-strain curves of Lattice 4 reveals a different behavior of the third test. The reason for the discrepancy of this test can be explained by the fact that the node connecting the struts to the bottom plate disconnected before reaching the plastic deformation region. Then, the lattice showed a reduced maximum stress when compared to the other samples. An internal defect during the manufacturing process is the possible cause of this earlier failure.

The overall observation of the stress-strain curves for all lattice geometries reveals that the heat-treated samples show the highest mechanical strength. Higher stress values were obtained, and it can be explained by the fact that the heat treatment changed the internal structure of the samples.

As expected from the theory, the stress-strain curve for the elastic ductile material shows a linear region followed by a plastic yielding region where, after strain hardening, reached the maximum stress level for each lattice.

Moreover, instead of fracture, further compression of the samples shows that the stresses will continually increase corresponding to the densification of the material.

Stress-strain curves for Inconel 718 lattices dependent on the relative density are plotted in Figure 3.15.

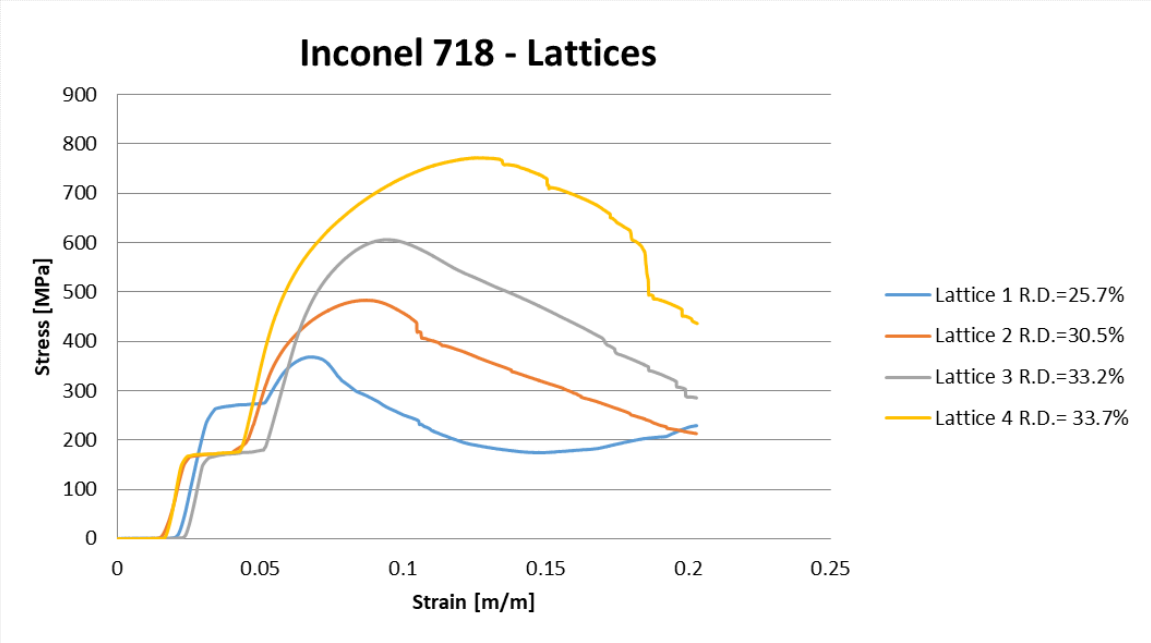

Figure 3.15: Stress-strain curves of lattices having different relative densities.

From the graph, it can be concluded that the increase of the relative density of the printed parts lead to increased mechanical properties. The maximum stress achieved was for the lattice 4, which also presents the highest relative density of 33.7%.

Further investigation included the surface of the heat-treated lattice. Figure 3.16 shows the light microscopy image of non-heat treated (a) and the other one heat treated (b) for Lattice 1.

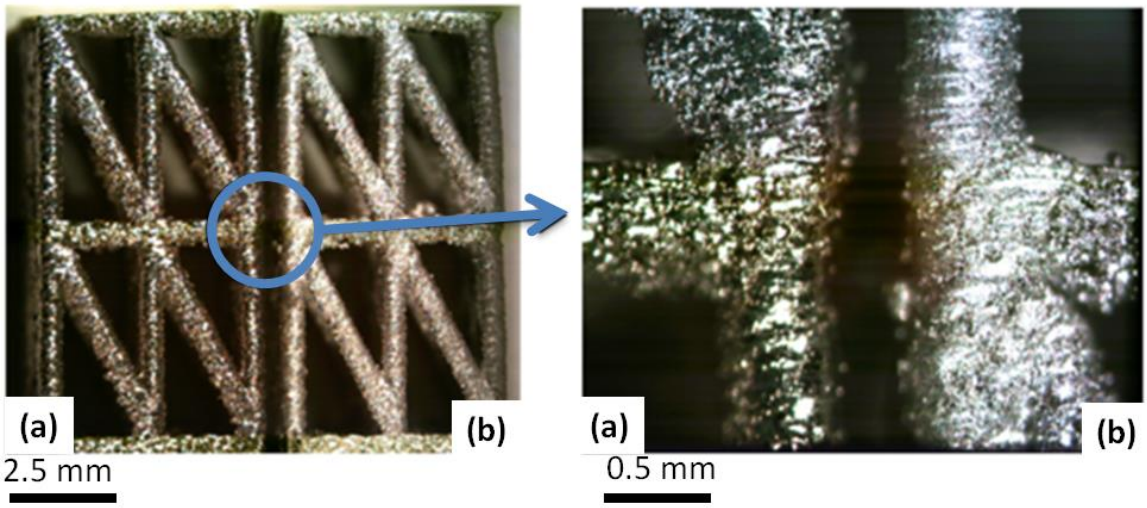

Figure 3.16: Morphology of Inconel 718 Lattices 1 surface: (a) As built; (b) Heat treated.

The rapid solidification of the layers during laser printing is responsible for the development of non-equilibrium phases where micro segregation of chemical composition and directional grain growth may be present. The laser interaction with the sample inputs a localized heat creating large thermal gradient that induces high thermal stresses [35].

Thus, heat treatment was performed to diminish those possible drawbacks of the SLM process as well as to reduce the voids due to pore defects.

Optical microscope images reveal a small improvement on the surface finish of the samples. The surface of the heat-treated structure presents a smoother finishing.

However, surfaces particles were not completely removed as can be seen in figure 3.16 (b).

Only a macroscopic analysis is not enough to understand the efficiency of the effect of the heat treatment on mechanical properties. Sometimes, process parameters are not always optimum and, as the result, defects that decrease mechanical properties of the printed parts are created inside the printed material [32]. Then, a more detailed investigation is needed to draw conclusions about the properties of the printed parts.

Besides light microscopy, SEM was involved in analyze the failure mechanism of printed Inconel 718 lattice structures. Details of the Inconel 718 Lattice 4 fractured sample, investigated using SEM as shown in figure 3.17.

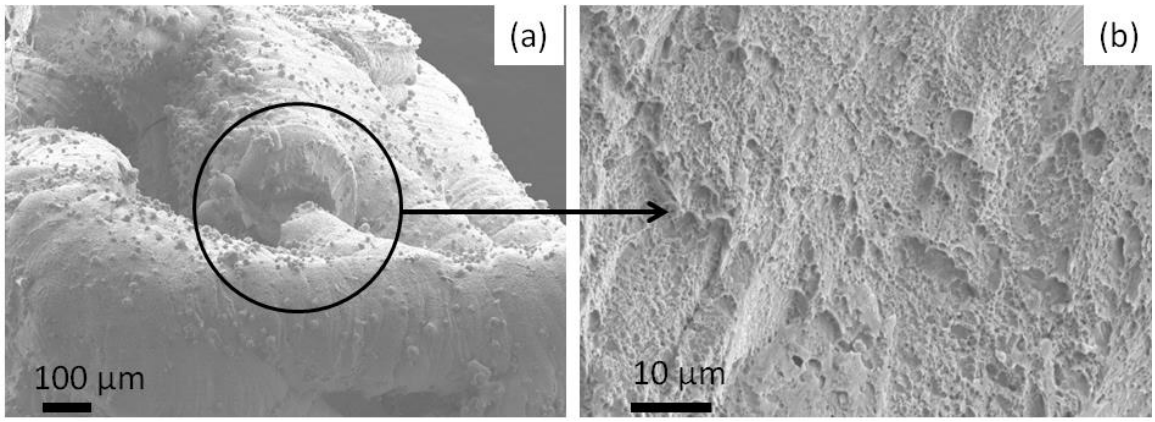

Figure 3.17: SEM investigation of Inconel 718 Lattice 4 - fractured surface details: (a) Cup-cone fracture; (b) Dimples.

Observing the failure strut on the sample of figure 3.17, it is possible to infer that the process occurs due to a tension stress on the region. The fracture is ductile due to the presence of nickel on the material composition where the dimples reveal that a plastic

deformation occurred before the failure. The characteristic of the failure is a cup cone fracture with a 45º appearance, as visible in Figure 3.17 (a). The heat treatment then improved the ductility of the part showing a tough material and a resilient structure.

The geometry of the failure region of the lattice structure (see Figure 3.17) impeded performing detailed analysis in the SEM. However, there is enough evidence to understand the failure mode.

Another SEM image of the Inconel 718 Lattice 4 was obtained for the strut connection next to the bottom plate and it is shown in figure 3.18.

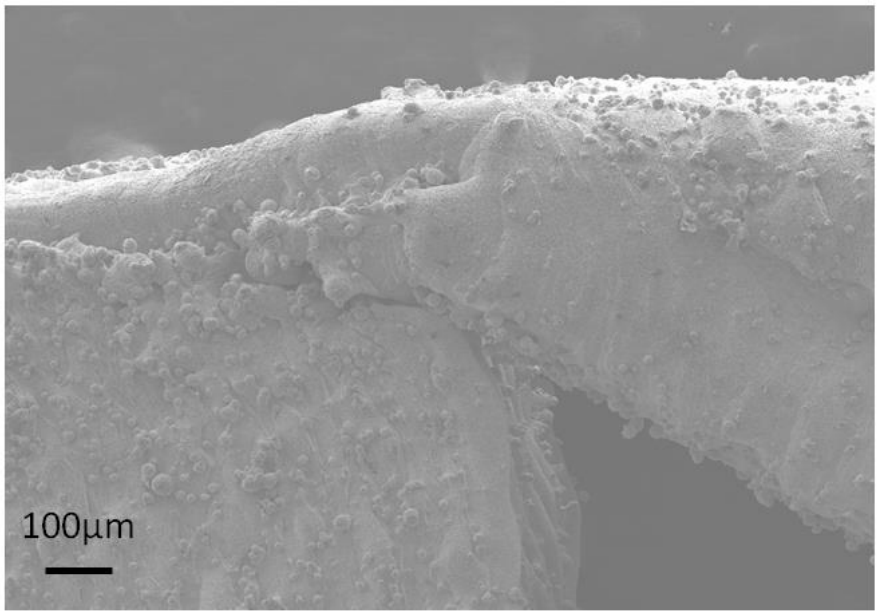

Figure 3.18: SEM Inconel 718 Lattice 4 – crack.

It is possible to see that the deformation of the strut due to the compression load induced a shear fracture at 45º next to the node connection. This created the crack next to the strut

where the stress concentration is present perhaps due to part discontinuity of the result of laser raster patter during the SLM process.

From this image it can also be seen the presence of unmelted particles on the surface that were not completely removed by the heat treatment.

3.2.2 Binder Jetting

The green parts of NiMnGa were heat treated at 1020 °C for 16h for sintering. Figure 3.19 shows the morphology of the sintered part.

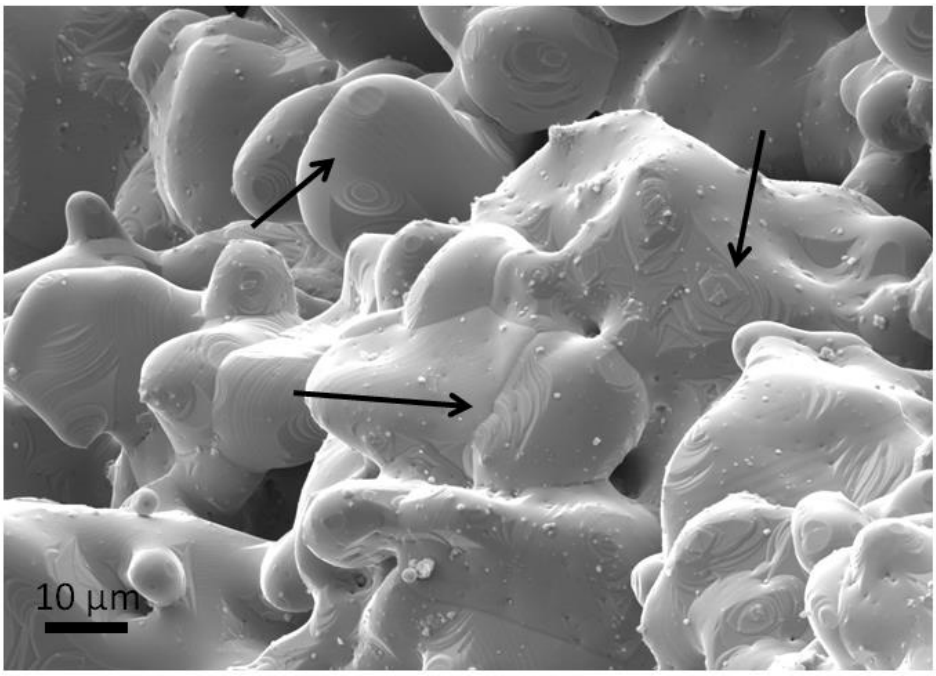

Figure 3.19: SEM – NiMnGa Lattice heat treated.

The parallel lines within the material, indicated by arrows, reveal the typical morphology of martensitic phase. Therefore, it can be state that the martensitic phase is present in printed material, as also proved by DSC investigation. Thus, the heat treatment was satisfactory in terms of preserving the desired characteristic.

After printed, the NiMnGa lattices produced via binder jetting were measured and weighted in order to calculate their porosity. Table 3.2 presents the results for each lattice.

Table 3.2: NiMnGa Lattices porosity levels

	Porosity (%)
Lattice 1	74.5
Lattice 2	65.4
Lattice 3	64
Lattice 4	63

Again, as noticed from the Inconel 718 samples, the increase of struts number from one lattice to the other promotes a decrease in the porosity with the increase of the weight.

However, in reality the overall porosities for the binder jetting samples should be lower. The printed samples, due to the small dimensions, presented some entrapped powders within the parts that should be voids. Figure 3.20 shows lattice 4 with entrapped powder that was not possible to be eliminated due to the nature of the manufacturing process.

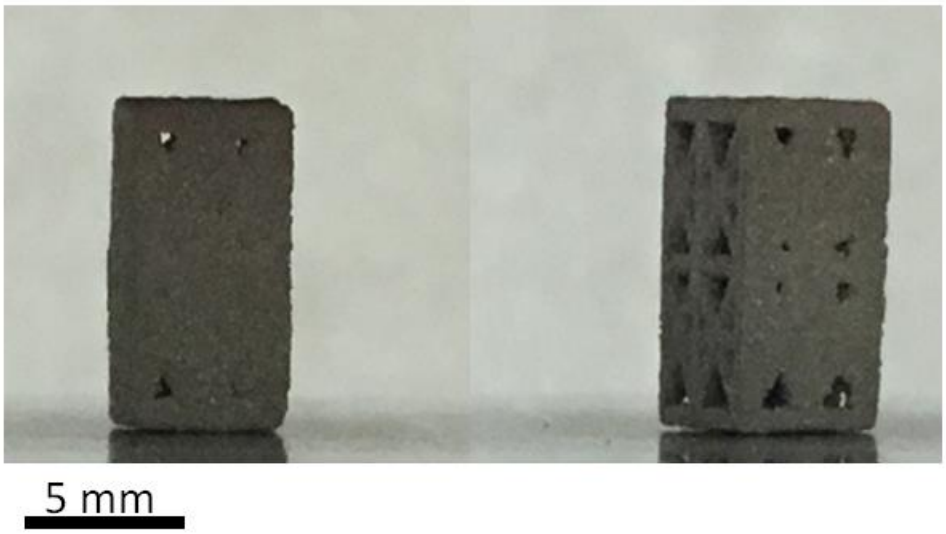

Figure 3.20: NiMnGa Lattice 4 – powders within the voids.

Samples prepared from 3D printing of NiMnGa powders presented surfaces that were not parallel within each other. Due to the brittle nature of the structures, they were not polished to avoid collapse of the lattices before testing.

Then, the compressive testing of the samples presented a gap between the compressor head interface and the sample top plate as shown in Figure 3.21.

The lack of parallelism induces errors and the experimental data may not be as accurate as should be. The initial compressive load in this case will force the right struts more than the others creating an unbalanced distribution of forces.

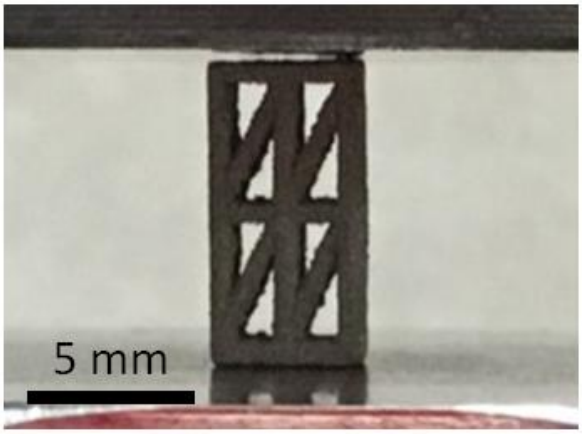

Figure 3.21: Unparalleled surfaces – NiMnGa lattice.

Another defect present in the NiMnGa samples was the ununiformed shrinking due to the heat treatment performed, as illustrated in Figure 3.22 that shows the shrinking of a lattice 3 sample.

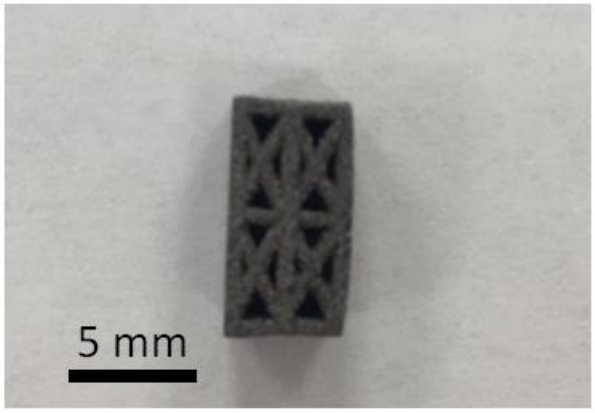

Figure 3.22: Shrink of lattice 3 due to heat treatment process.

Based on the load vs. extension raw data from Instron, the stress-strain curves for NiMnGa lattices are shown in Figure 3.23.

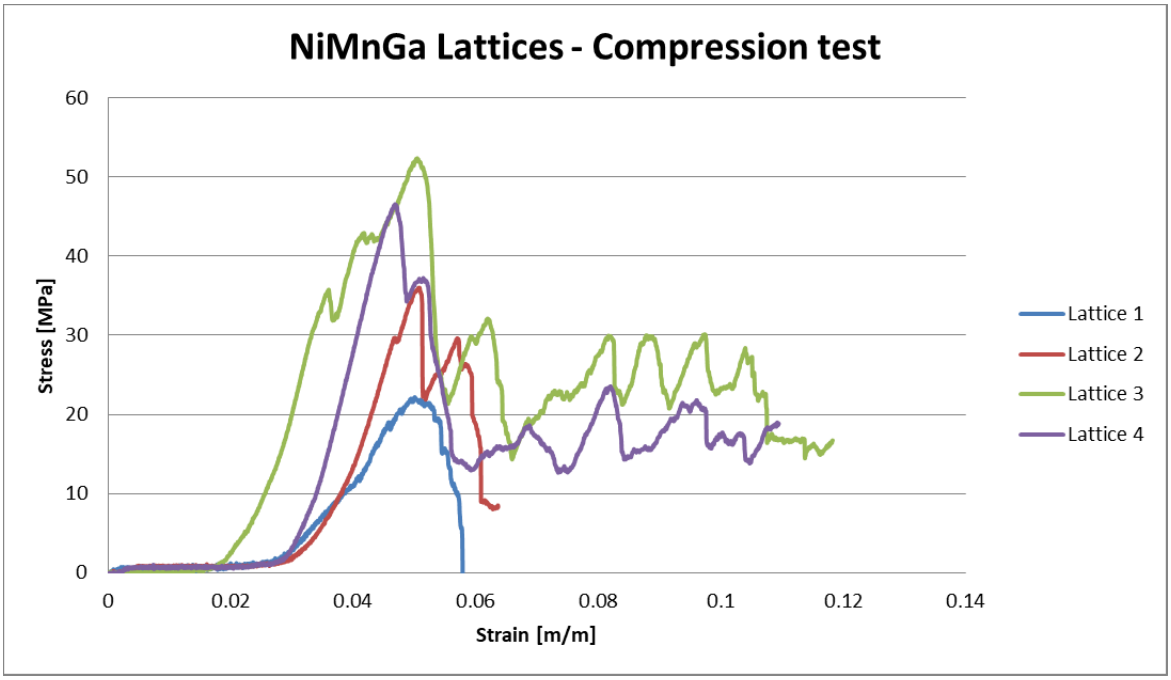

Figure 3.23: Stress-strain curve Lattices NiMnGa.

As opposed to the stress-strain curves from the Inconel 718 lattice structures, that are characteristic of ductile materials, the NiMnGa samples present a brittle response. The initial stress increases with the strain and does not present a plastic behavior. Instead, after reaching the maximum stress, the material fractures.

This is an expected result since the NiMnGa is a brittle material from its nature. However, it is possible to conclude that the increase of the porosity level within the structure produced a higher maximum stress for the studied lattices.

Figure 3.24 shows the SEM image of NiMnGa lattice 1. From a detailed observation, it can be noted the bimodal nature of the porosity in the NiMnGa.

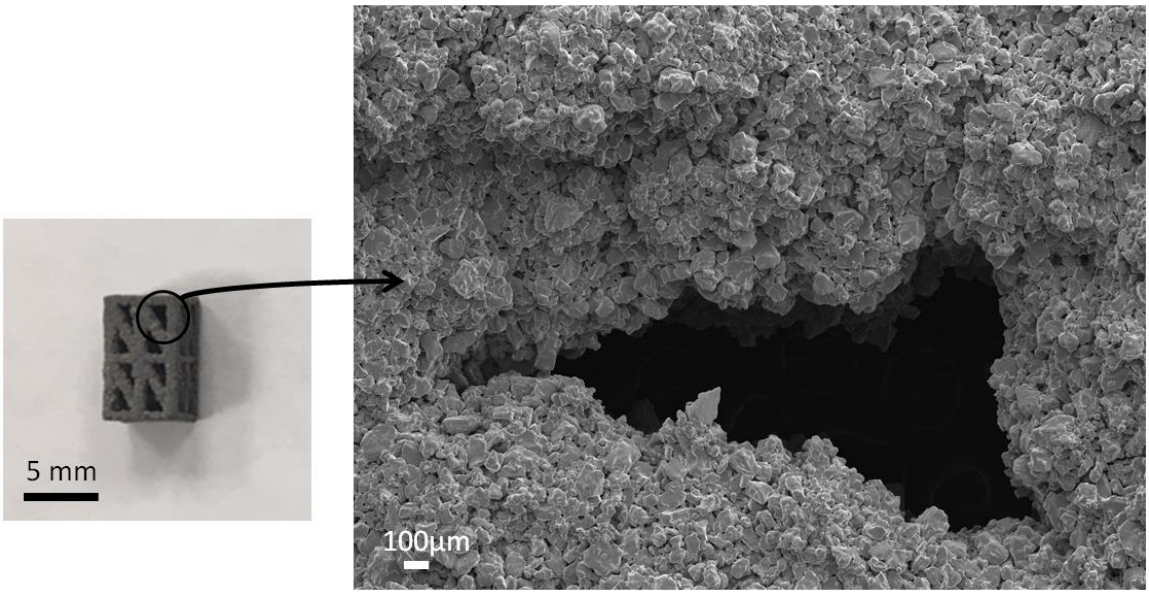

Figure 3.24: Dual porosity of NiMnGa lattice.

Photographs of NiMnGa lattices during compressive testing are shown in Figure 3.25. The pictures of the NiMnGa lattices taken under compressive loading reveal the nature of the brittle fracture that was also concluded from the stress-strain curves.

In this case, the samples present a sudden crack within the material and immediately fail. The increase of the struts helped to delay the fracture and the use of horizontal struts increased the maximum stress capacity of the sample preserving a higher integrity of the structure during the test.

Due to the type of failure, the collapse mechanism for the samples cannot be predicted. A more accurate analysis would also need to take into account the deformation of more samples for each lattice structure.

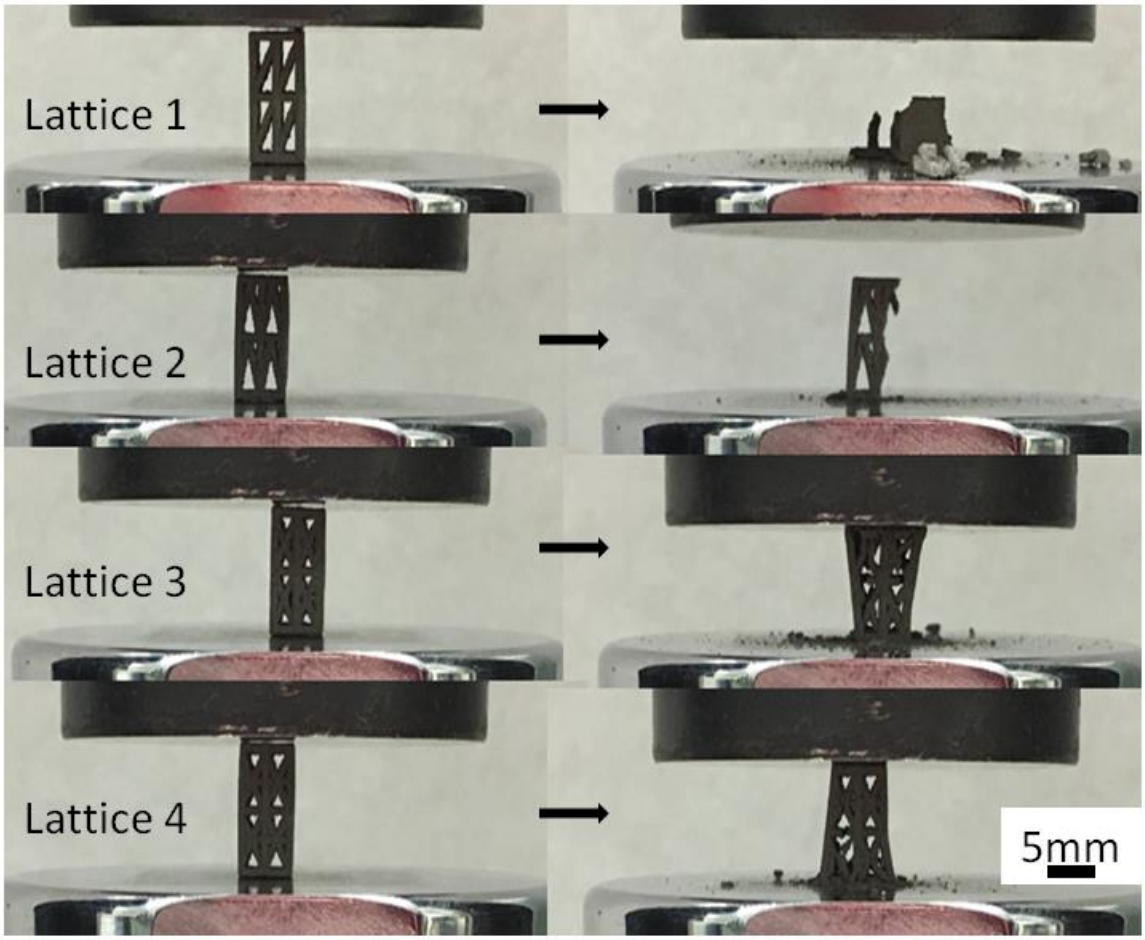

Figure 3.25: Deformation and fracture of NiMnGa Lattices during compressive testing.

Figure 3.26 shows fracture surfaces for the compressive failed NiMnGa samples.

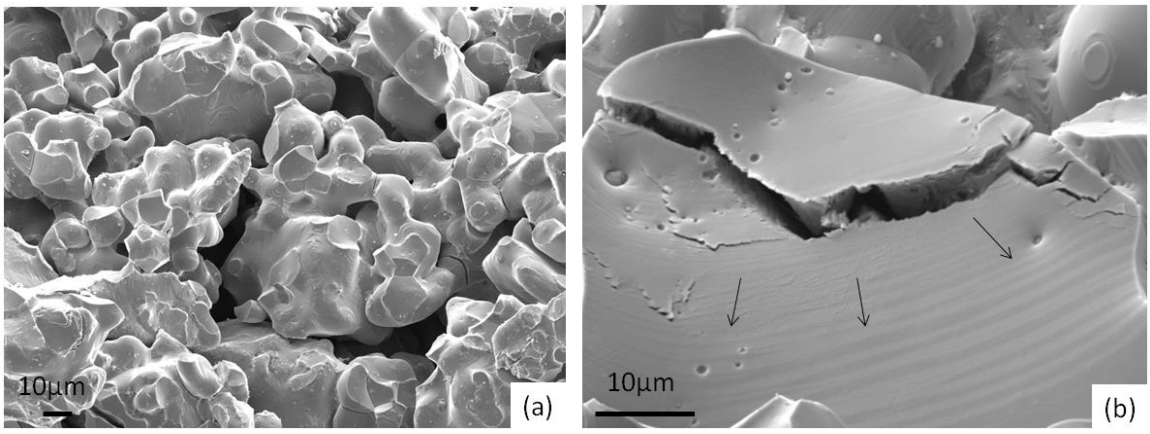

Figure 3.26: NiMnGa lattice fractured (a) Brittle fracture morphology; (b) Fracture along twin boundary.

The details of this fracture show that the brittle fracture occurred at the sintering necks between two particles, where the cross-sectional area of the sample had minimum surface. The sintering necks act as a weak bond within the structures, as well as twin boundaries of the martensitic structure. The arrows in Figure 3.26 (b) indicate the crack propagation along a twin boundary.

The mechanical property investigated for each lattice from each material was the Young's modulus. Represented by E and given in MPa units, it was calculated from the elastic portion of the experimental stress-strain curves, using Figures 3.27 to 3.34.

For each geometry, a stress-strain curve was selected and a linear portion with a 0.01 strain variation was used to determine the elastic modulus. Then, a linear trendline was stablished for the curve and the E modulus was obtained from the slope of the line.

The calculated E values for Inconel 718 lattices are presented in Table 3.3, and those for NiMnGa lattices are presented in Table 3.4.

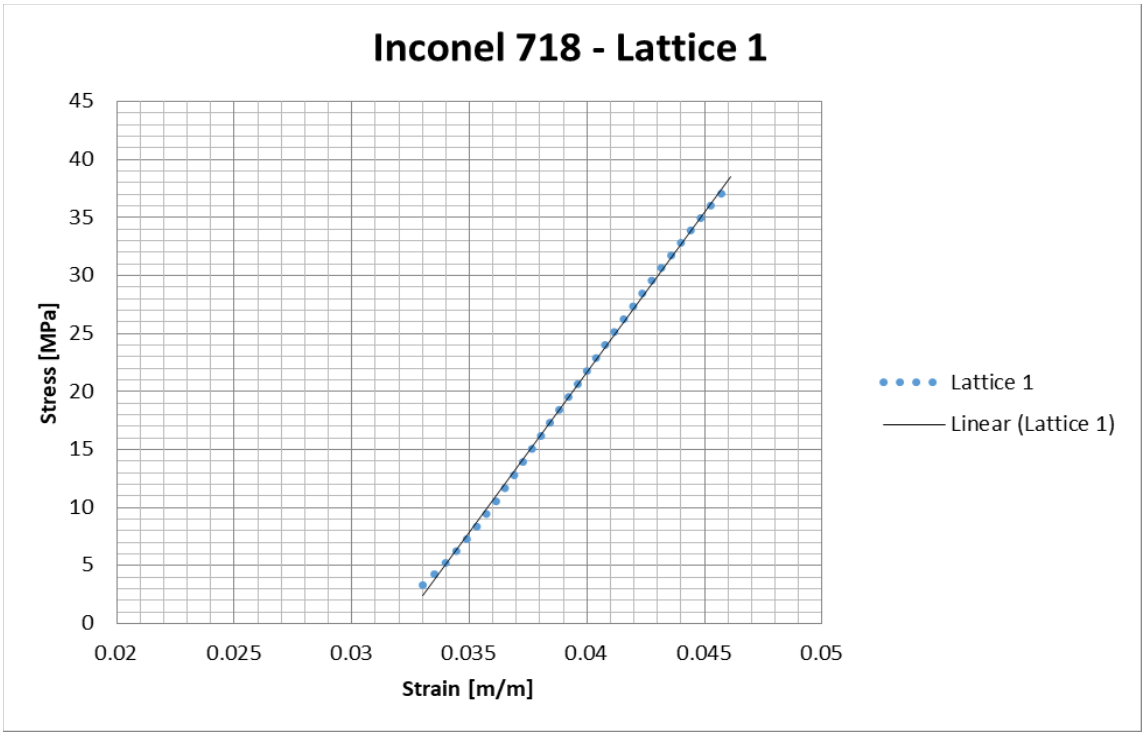

Figure 3.27: Elastic curve Inconel 718 - Lattice 1

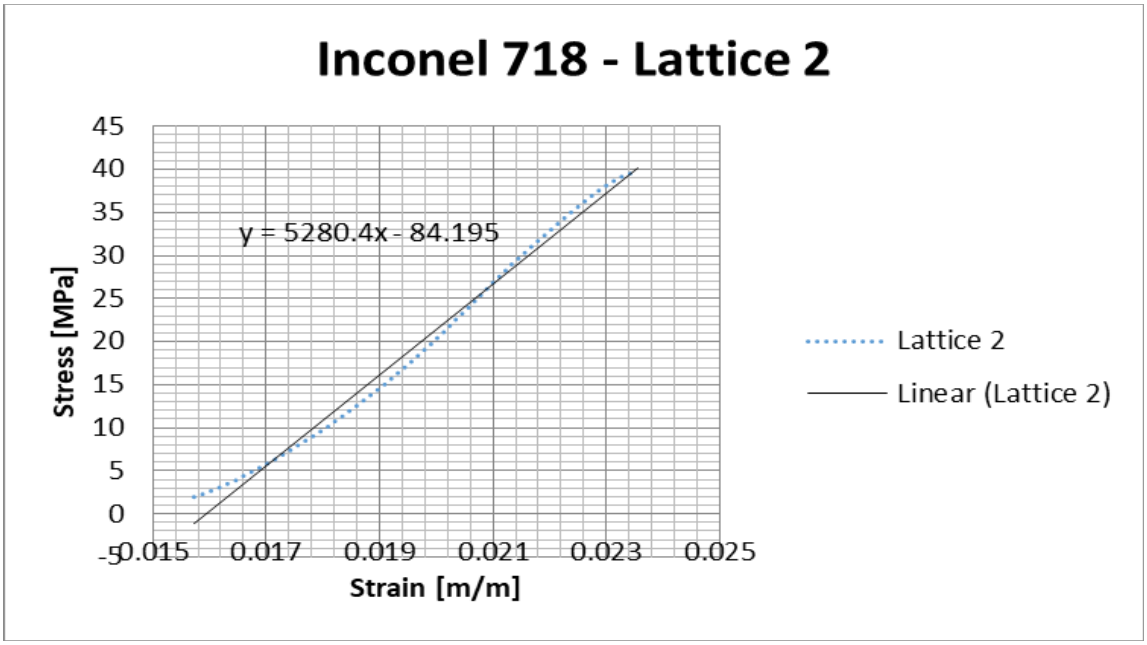

Figure 3.28: Elastic curve Inconel 718 - Lattice 2.

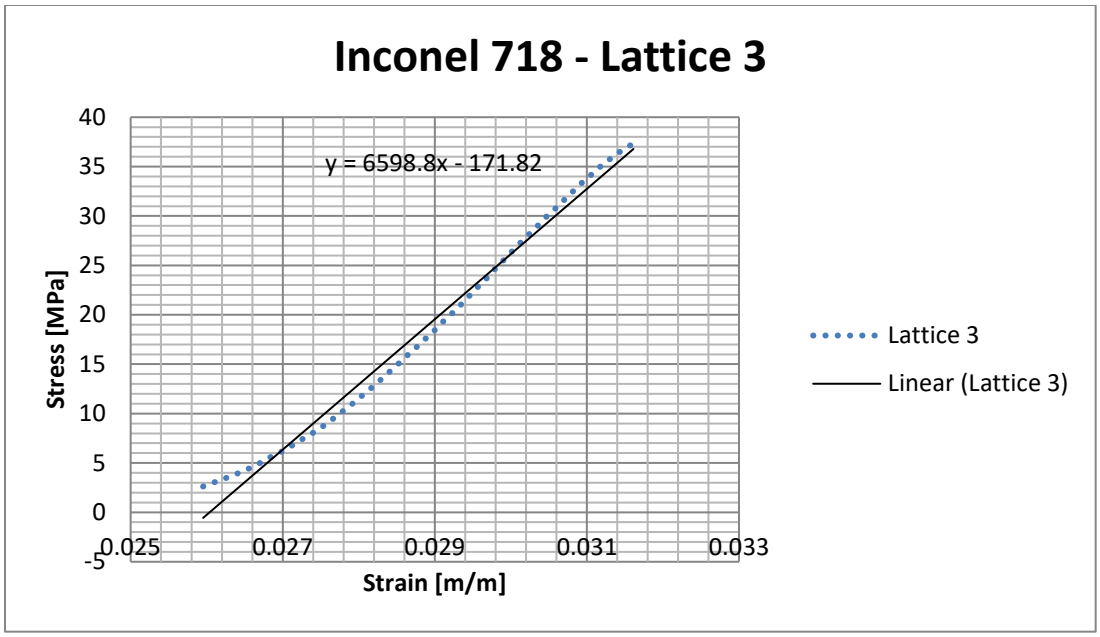

Figure 3.29: Elastic curve Inconel 718 - Lattice 3.

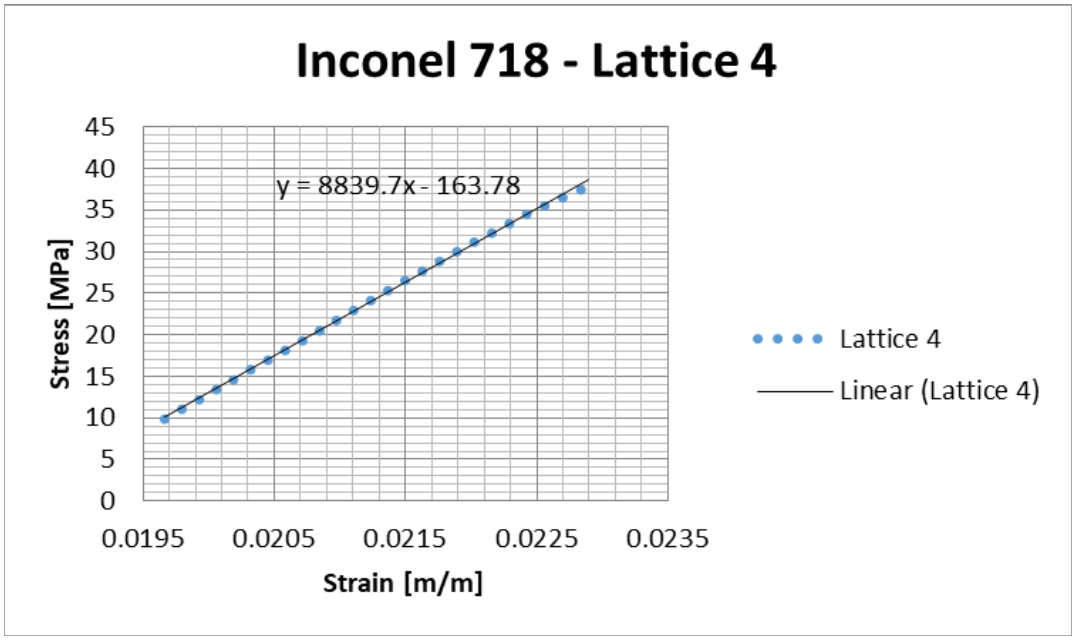

Figure 3.30: Elastic curve Inconel 718 - Lattice 4

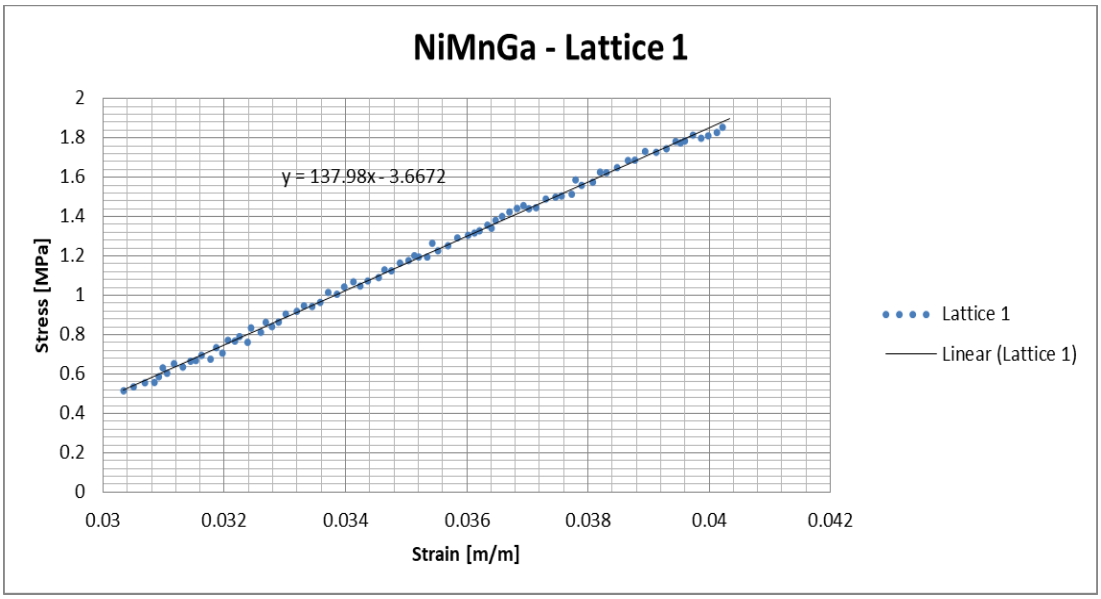

Figure 3.31: Elastic curve NiMnGa - Lattice 1.

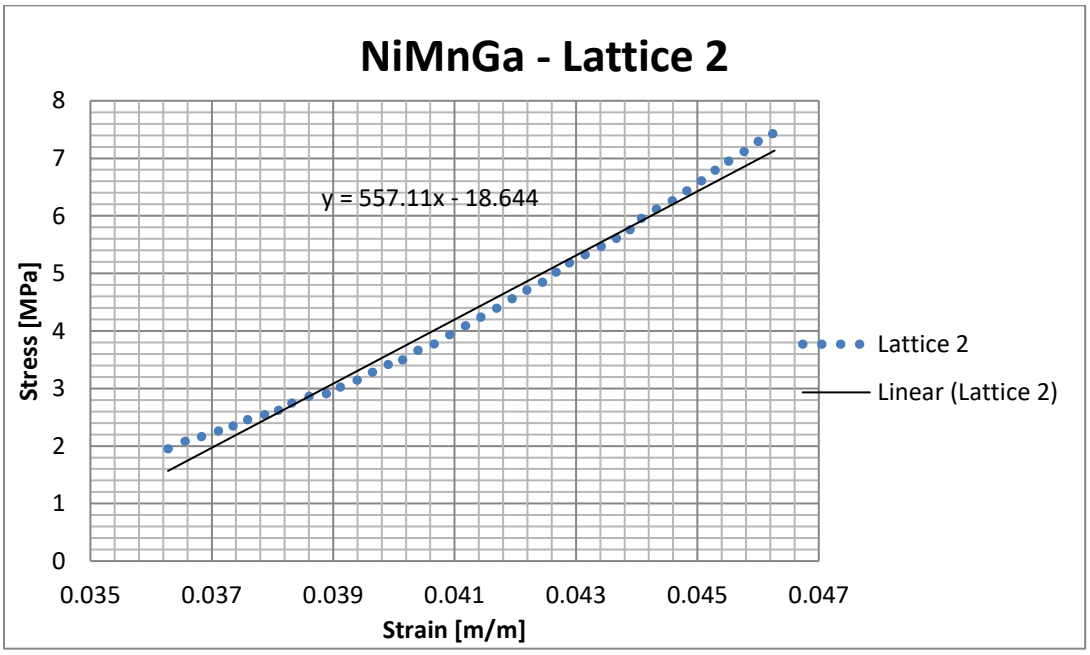

Figure 3.32: Elastic curve NiMnGa - Lattice 2.

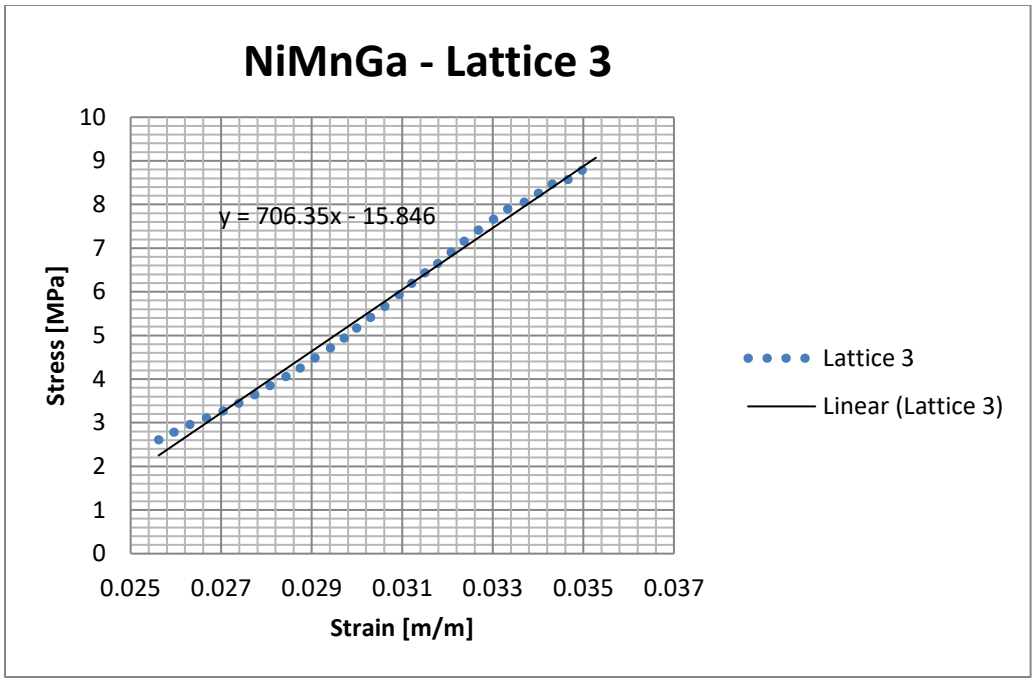

Figure 3.33: Elastic curve NiMnGa - Lattice 3.

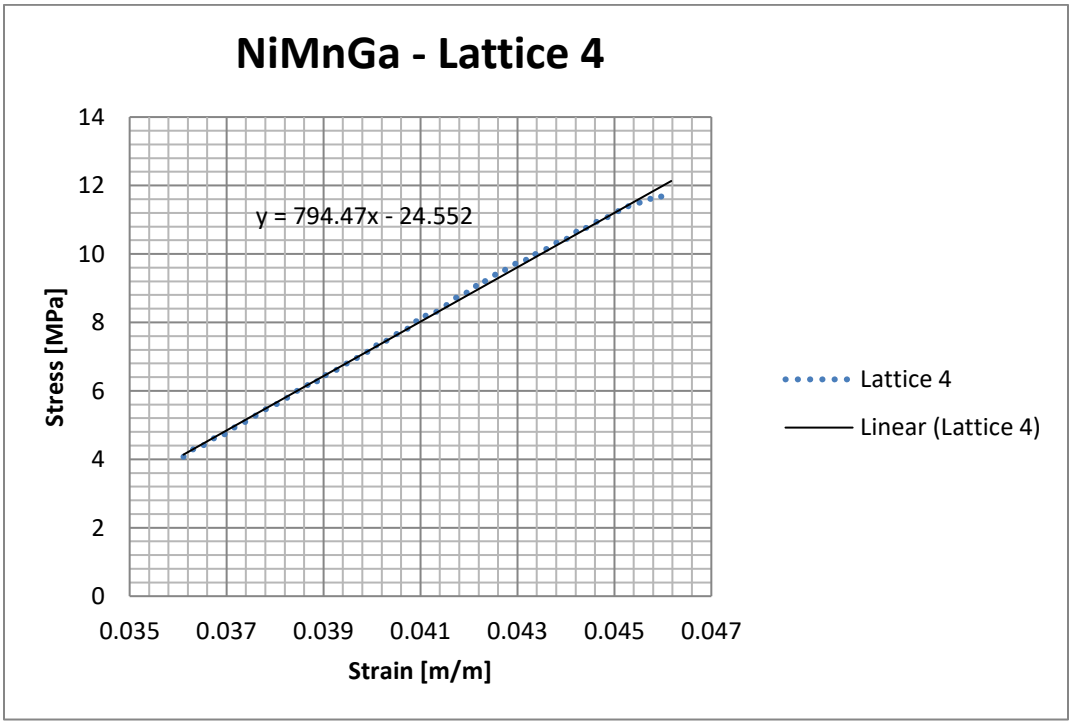

Figure 3.34: Elastic curve NiMnGa - Lattice 4.

Table 3.3: Inconel 718 Lattices –Elastic Modulus

	Elastic Modulus (MPa)
Lattice 1	4144.8
Lattice 2	5280.4
Lattice 3	6598.8
Lattice 4	8839.7

Table 3.4: NiMnGa Lattices – Elastic Modulus

	Elastic Modulus (MPa)
Lattice 1	137.98
Lattice 2	557.11
Lattice 3	706.35
Lattice 4	794.47

From the linear part of the stress-strain curves for both Inconel 718 and NiMnGa lattices, the reduction in the porosity resulted on increased values of Young's modulus.

Then, even though the samples presented defects due to the manufacturing methods, the overall response was in accordance to the expected results predicted by the theory. A more refined study is necessary to determine the relation between the level of porosity and the mechanical properties of the created lattices. Also, more NiMnGa samples need to be tested to verify the range of the maximum stresses for each lattice.

From the stress strain curves, the specific strength was calculated for the NiMnGa lattices. Then, the values were compared to the specific strength of the bulk material.

Table 3.3 shows the values calculated for NiMnGa lattice.

Table 3.5: NiMnGa Lattices – Specific strength compared to bulk

Ni-Mn-Ga Bulk Specific Strength: 0.048 MPa m^3/kg

Lattice – NiMnGa	Specific Strength (MPa m^3/kg)	% Compared to Bulk
1	0.031234	-36.16
2	0.046902	-4.14
3	0.057799	18.12
4	0.064778	32.39

It can be seen that the increase of the relative density produced increased specific strength. Lattice 4 had 66.3% of porosity and delivered a specific strength increase of 32.39% when compared to the bulk part. As an overall, lattices 3 and 4 present a better specific strength than bulk and can be successfully printed. Thus, the NiMnGa were successfully 3D printing with dual porosity, near net shapes, reduction of weight and increased mechanical properties.

3.3 Modeling Results

3.3.1 FEA of Inconel 718 Lattice Structures

The use of the mechanical properties of solid/bulk Inconel 718 to perform the simulation of compressive testing of the lattice samples allowed understanding the behavior of collapse mechanisms of created geometries. The deformations from FEA analysis were visually compared to the real deformation of the lattices. The maximum stress points in the simulation were mapped to understand where the weakest struts fail and how geometry optimization affects the mechanical behavior.

For Inconel 718 lattice structures, the results of FEA modeling, including deformation and maximum stress location for each lattice structure type, are presented below.

Lattice 1:

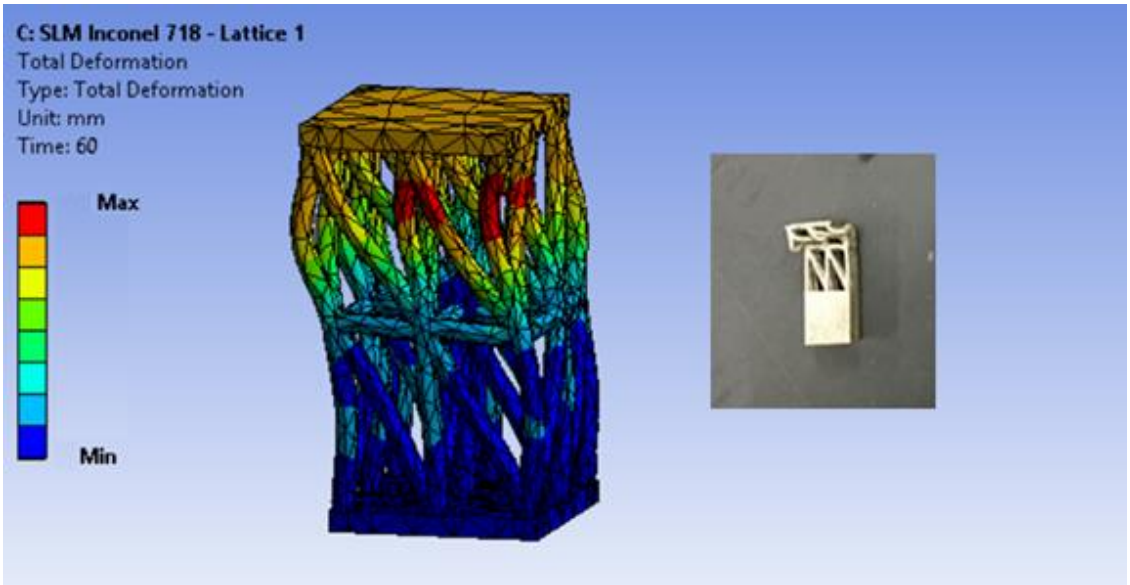

Figure 3.35: Deformation of Lattice 1 – Inconel 718.

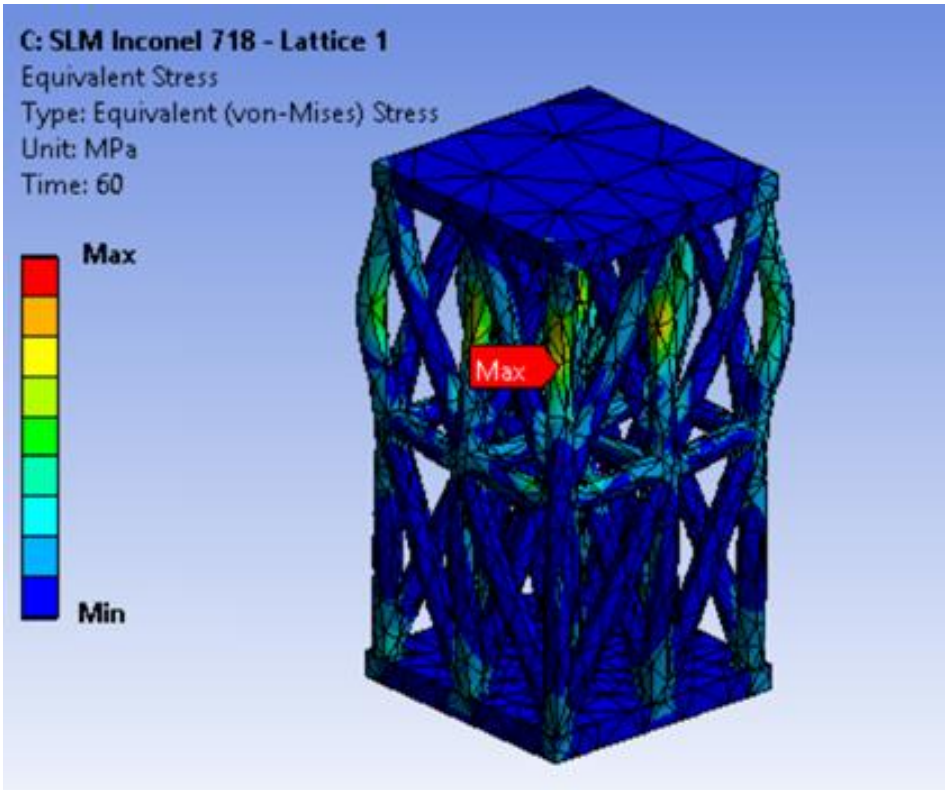

Figure 3.36: Stress distribution on struts Lattice 1- Inconel 718.

Figures 3.35 and 3.36 show the deformation and stress distribution for lattice 1. From the models, it can be concluded that the maximum stress concentrates on the vertical strut that does not have a support connection.

The compressive load in this case promotes bending of the strut and the deformation of the lattice is guided from this point.

Lattice 2:

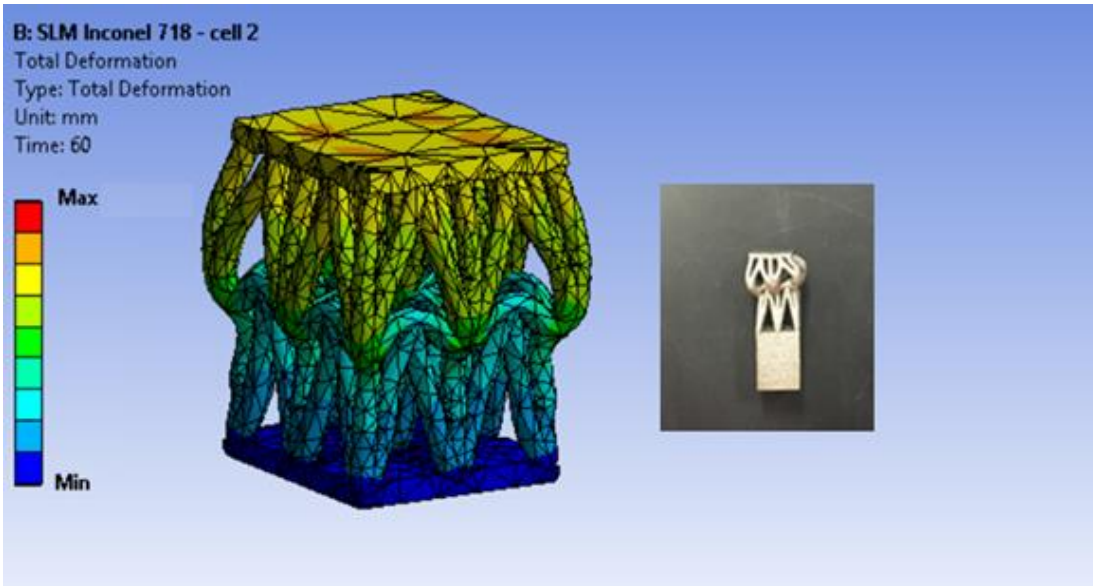

Figure 3.37: Deformation of Lattice 2 – Inconel 718.

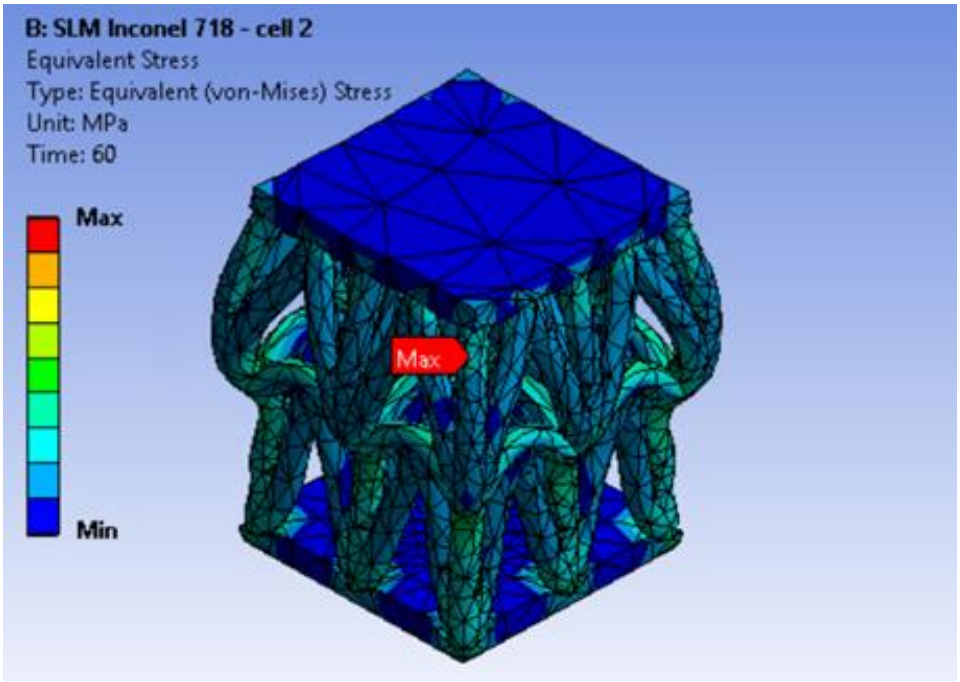

Figure 3.38: Stress distribution on struts Lattice 2 - Inconel 718.

For lattice 2, Figures 3.37 and 3.38, simulation behavior is similar to the collapse mechanism found by experimental testing. However, two of the lattices tested, presented collapse of the node. In that case, the failure can be attributed to the defect from the manufacturing method, where a discontinuity in the layer of the material induces crack propagation. Samples that do not experience that defect had similar behavior as the modeled one, where the maximum stress concentrates on the vertical external strut that bends and reduces the mechanical properties of the geometry.

Lattice 3:

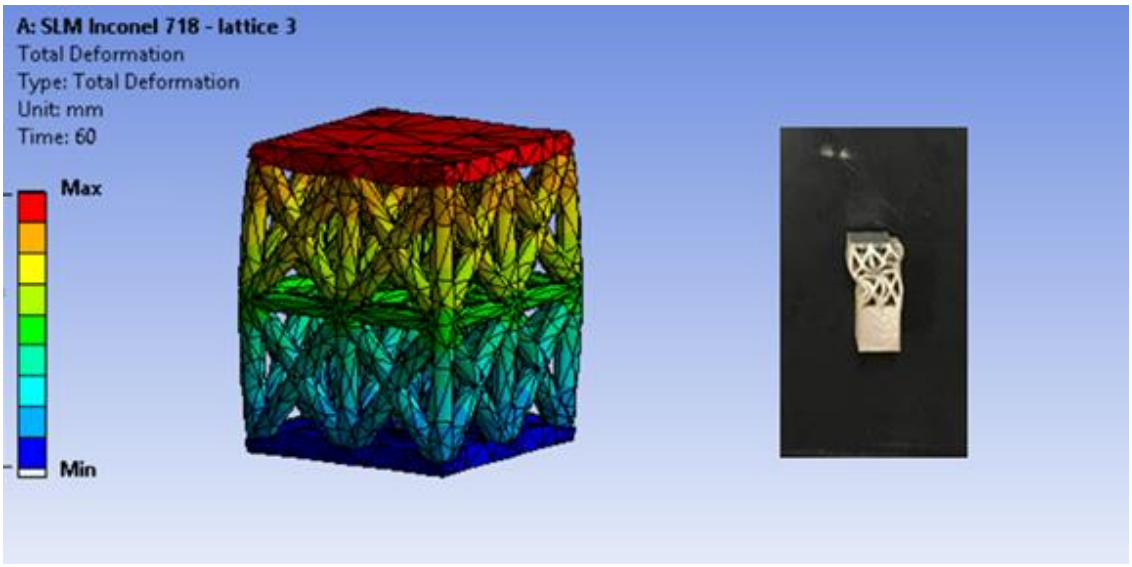

Figure 3.39: Deformation of Lattice 3 – Inconel 718.

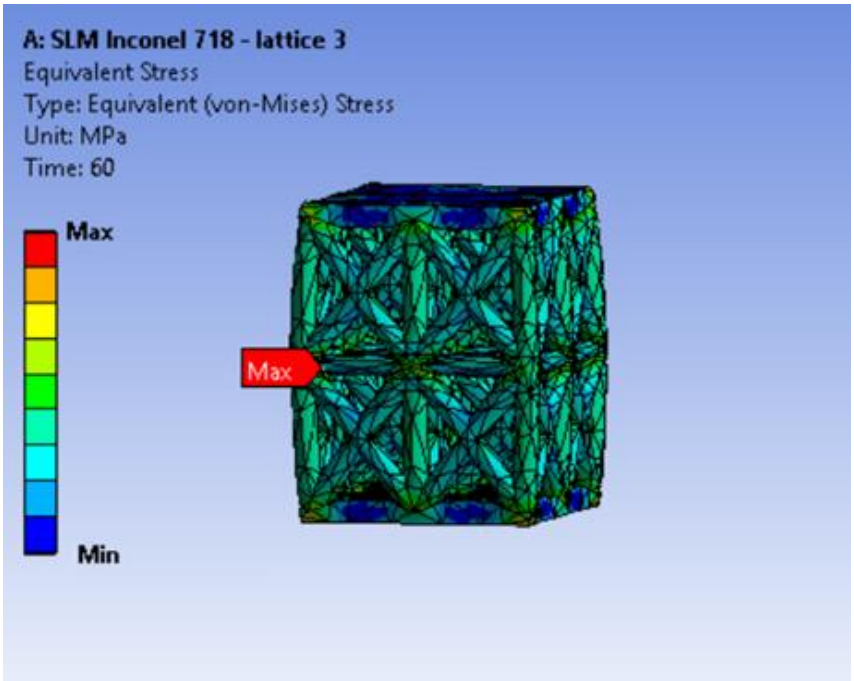

Figure 3.40: Stress distribution on struts Lattice 3 - Inconel 718.

The case of lattice 3 of Inconel 718, Figures 3.39 and 3.40, is inconclusive for the simulated and the real deformation behavior of the structure. In this situation, it is necessary to perform complete failure analysis of all deformed samples in order to understand the reason of the failure, because the photographs from the compressed samples indicate that it could be due to defects from manufacturing process.

On the other hand, the maximum stress point is similar to the point where a fracture due to tension load occurred in the heat-treated sample, which presented the best mechanical properties. Then, in this case, the distribution of the struts contributed to a better load distribution within the structure.

Lattice 4:

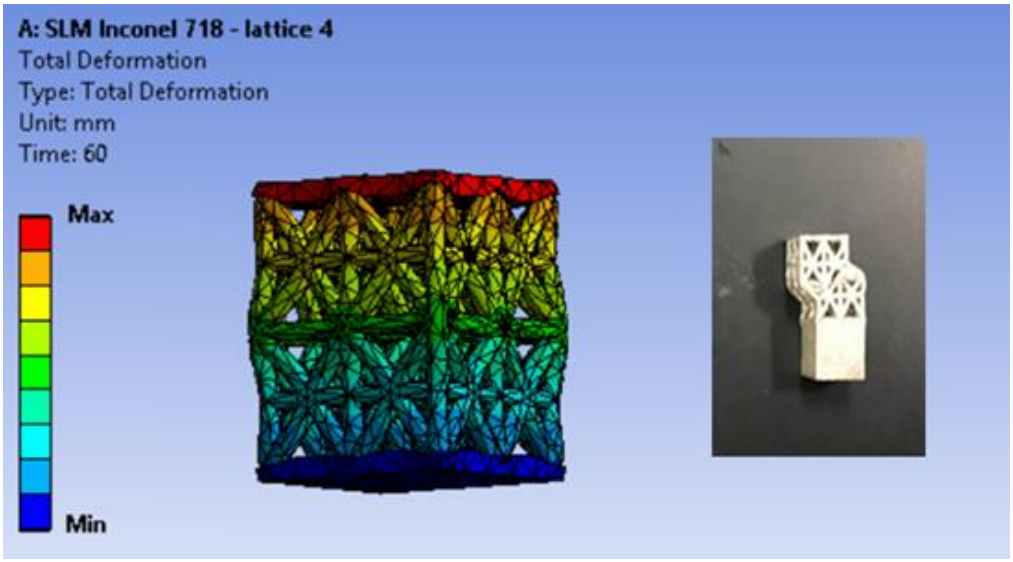

Figure 3.41: Deformation of Lattice 4 – Inconel 718.

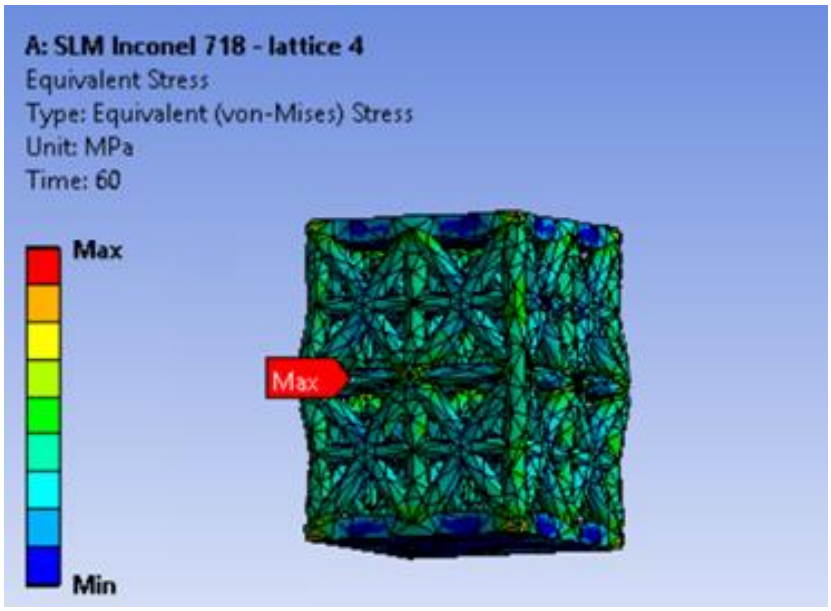

Figure 3.42: Stress distribution on struts Lattice 4 - Inconel 718.

The last case for the Inconel 718 is the lattice 4, Figure 3.41 and 3.42. Similarly to the lattice 3, the deformation model expected in the simulation is more uniform than in reality. The bent of the strut from experimental compressive testing may suggest that a manufacturing defect or a not perfect parallel surface were present and thus directly affects the deformation behavior.

The maximum stress point in this geometry is expected to be in the same strut and region where rupture of the strut was reported in the experimental analysis. Then, lattices 3 and 4 are optimized compared to lattices 1 and 2 since the compressive load was distributed as a tension load within horizontal struts. This is a desired characteristic when designing the lattice because the vertical struts will bare less compressive load and the mechanical properties will be enhanced.

3.3.2 FEA of NiMnGa Lattice Structures

The mechanical properties of solid/bulk NiMnGa were used in numerical analysis of NiMnGa lattice behavior under compressive load. The modeling allows understanding the failure mechanisms of printed geometries. Due to the characteristic brittleness of this material, a deformation behavior pattern cannot be determined. Then, stresses from FEA analysis were compared to the real failed samples in order to stablish a relation between the compressive testing and the struts distribution within the lattice.

For NiMnGa lattice structures, the stress distributions obtained by FEA modeling are presented in Figures 3.43 to 3.44.

Lattice 1:

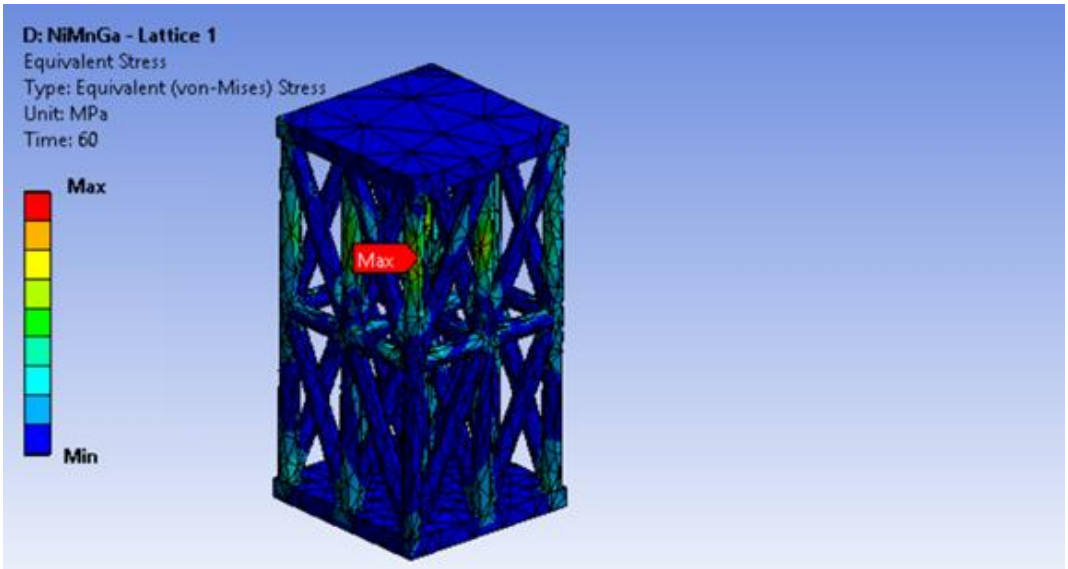

Figure 3.43: Stress distribution on struts Lattice 1- NiMnGa.

Since the experimental part presented a total collapse of lattice 1 it was not possible to map a strut failure. In this case, theoretical analysis based on the FEA model suggests

that the outsider strut, as shown in Figure 3.43, is the most likely to fail and be responsible for the lattice collapse.

Lattice 2:

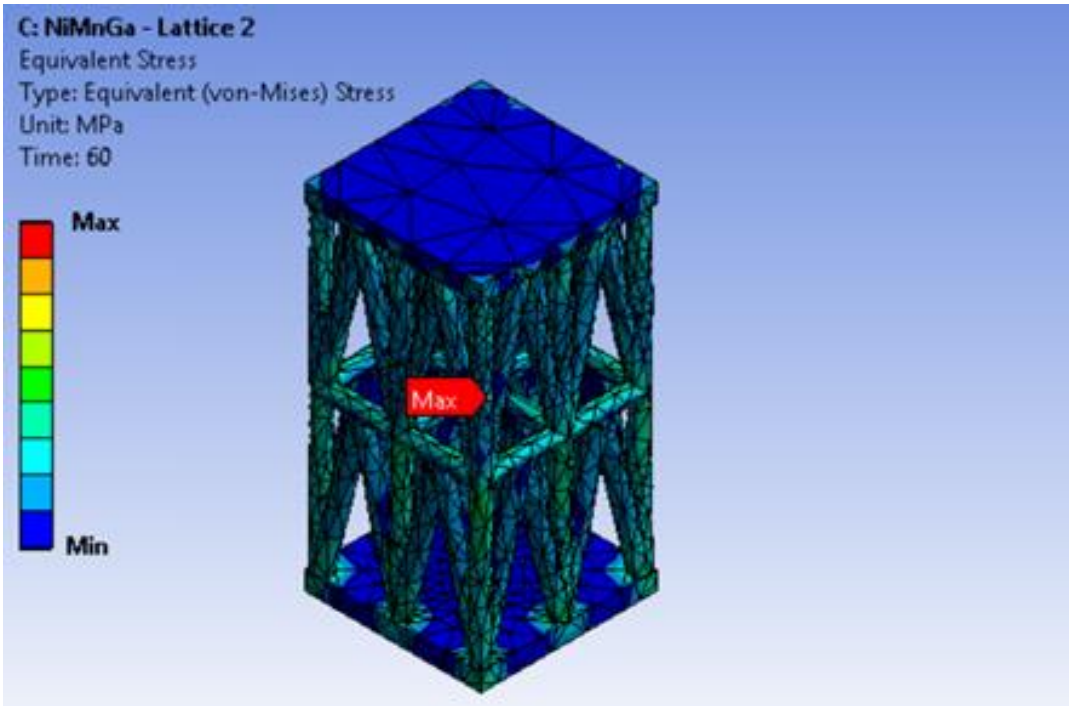

Figure 3.44: Stress distribution on struts Lattice 2- NiMnGa.

The second lattice, when deformed under compressive loading presented a collapse of an entire side of the lattice, as shown in Figure 3.44.

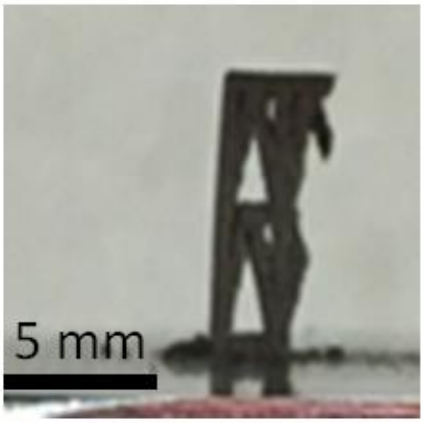

Figure 3.45: Experimental collapse of lattice 2 from NiMnGa.

When compared to the maximum stress location in the simulated model, the right strut appears to be the one that failure as seen in Figure 3.45. In this case, the simulation and the experimental data show some similarity.

Lattice 3:

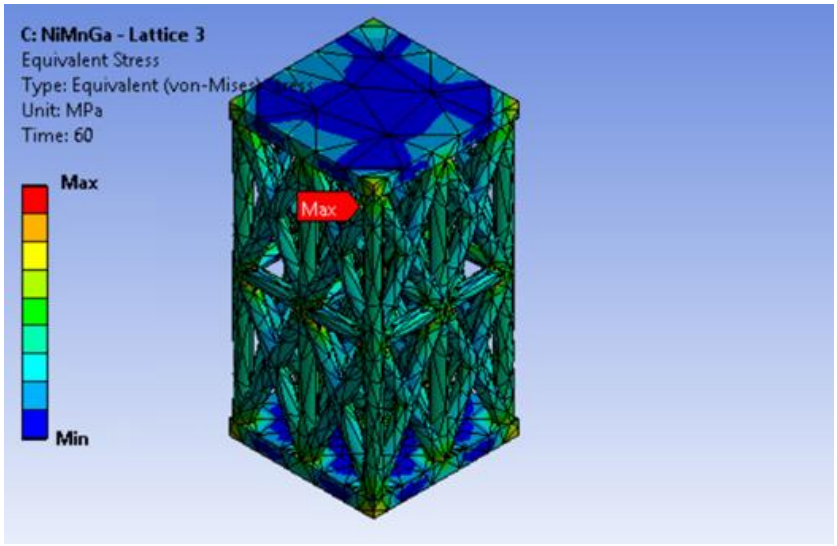

Figure 3.46: Stress distribution on struts Lattice 3- NiMnGa.

For the case of lattice 3, Figure 3.46, the model predicts a maximum stress located near one of the nodes in the corner of the sample. Comparing with the experimental collapse behavior, it can be seen that there is actually a crack near the node in the corner similarly to the FEA model as shown in figure 3.47.

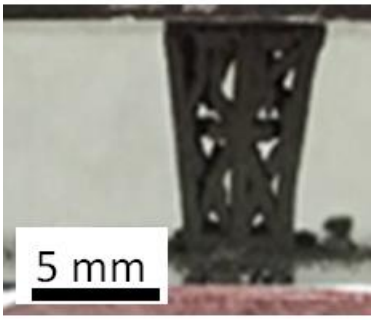

Figure 3.47: Experimental collapse of lattice 3 from NiMnGa.

Lattice 4:

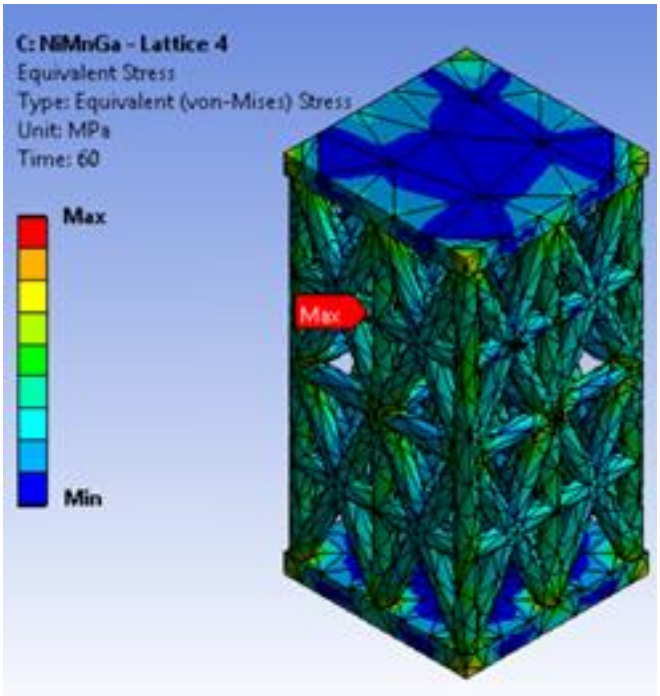

Figure 3.48: Stress distribution on struts Lattice 4- NiMnGa.

Finally, for lattice 4, it can be seen from Figure 3.48 that the maximum stress is located on the horizontal strut responsible for absorbing some of the compressive load and redistributing it as a tensile stress. This is similar to the behavior of the ductile lattice 4 made of Inconel 718.

Figure 3.49 shows the fracture that is nearby the location of maximum stress determined by simulation.

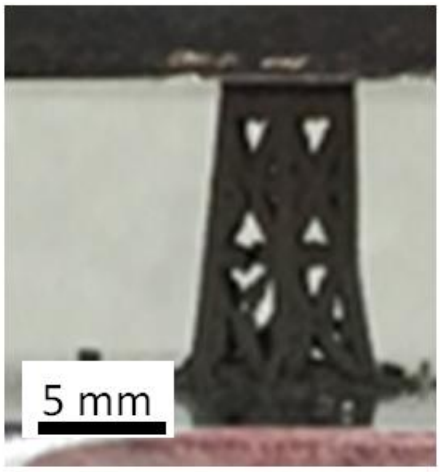

Figure 3.49: Experimental collapse of lattice 4 from NiMnGa.

Then, even though the nature of the materials is different, the geometry still dictates some of the failure behavior.

Chapter 4 - Additive Manufacturing of Iron-Based High Temperature Magnetic Materials

This work was performed as part of the Ohio Federal Research Network (OFRN) High Temperature Magnetic Materials grant.

4.1 Introduction

The objective of studying magnetic alloys is to contribute in producing parts that can be used in electric power technologies such as ultra-efficient commercial vehicles, solar and wind turbines, and hybrid-electric aircrafts propulsion.

Hybrid-electric and all electric concepts are continuously being explored to develop aircraft propulsion systems that deliver efficiency and sustainability. The reliance on electrical power generation, conversion, and condition technologies is crescent since the advances in technologies are allied with lower carbon emissions [42].

Magnetic materials existent today and that are used in electrical applications present substantial core losses. This leads to a poor performance under high frequencies and reduce full exploration of power electronics. Thus, there is a requirement for soft magnets materials that present lower losses at 20 kHz at high temperatures environments [43 44 45].

A class of magnetic materials investigated in this research is categorized as a nanocrystalline soft magnetic alloy. The advantage of it consists on the high efficient core material for alternating current applications. This is a consequence of the large saturation magnetization and the coercivity (resistance of the material to changes in magnetization).

Nanocrystalline magnetic materials are nanoscale magnetic crystallites in an intergranular amorphous matrix. Grains need to be smaller than a fundamental magnetic length scale in order to deliver large saturation induction and high permeability. This reduces the core losses and improves the performance of the material.

A cost-effective production of Fe-Co-Ni-Zr-B-Cu consists in reducing the Co content and developing a non-equilibrium process.

First, long and thin ribbons are created by rapid solidification delivering an amorphous alloy. Then, the ribbons are annealed above 500ºC and ultrafine grains are created.

The rapid solidification is possible due to the use of a melt-spinning technique. This method uses induction coils that melt the ingot placed in a quartz crucible. The molten ingot is splashed on a rotation copper wheel that promotes the solidification of the melt [46].

4.2 Purpose

This works focuses on the study of Fe-Co-Ni based nanocomposite soft magnetic alloys in order to develop smaller, lighter, and more energy efficient power converters. This would enable future creation of electric aircraft power technologies.

Form factors of present materials restrain exploring new geometries and the use of AM expands these possibilities. Thus, Youngstown State University teamwork is contributing in producing advanced soft magnetic materials for high temperature aeronautic applications by creating inductor designs with the binder jetting 3D printing method available at the Center for Innovation in Advanced Manufacturing.

4.3 Experimental Methods

The steps needed to produce the parts by AM include characterization and classification of the Fe-Co-Ni based powder, determination of physical and mechanical properties, exploration of different designs for specific applications, modeling of produced parts, and macro/micro structural characterization.

Seven samples of different batches of $Fe_{77}Ni_{5.5}Co_{5.5}Zr_7B_4Cu_1$ produced powders were provided for this study. The magnetic powders were produced by ball milling from melt quenched ribbons described in the introduction. Magnetic powder size distribution and particle morphology determine the binder jetting printing parameters such as layer thickness and binder saturation. Therefore, the received particles have been investigated using several materials characterization techniques. The particle size distribution was investigated using CILAS technique and the morphology and chemical competition was evaluated using JEOL JSM 7600F scanning electron microscope (SEM) equipped with X-ray energy dispersive spectrometer (XEDS). In order to investigate the printing behavior of the magnetic powders, several samples were produced using the following method. A cylindrical mold with an internal diameter of 5 mm and about 5 mm height was filled with Fe-based magnetic powder and then the binder (aqueous based) was added to the mold. The sample was then cured at 190°C for 4 h in air. After one part have been sintered at 600°C for 24h.

4.3 Results and Discussion

As mention above seven batches of $Fe_{77}Ni_{5.5}Co_{5.5}Zr_7B_4Cu_1$ magnetic powders have been received from University of Toledo. The results presented below are only for sample 0 (the first received sample) and sample 2 (the third sample we received). However, a summary of main characteristics of all seven samples is tabulated at the end of the chapter.

4.3.1 Sample 0

This metal powder was produced by ball milling in ZrO jar-ball system for 36 hours. The size distribution was determined using CILAS machine located at YSU. Figure 4.1 shows the particle size distribution for this sample.

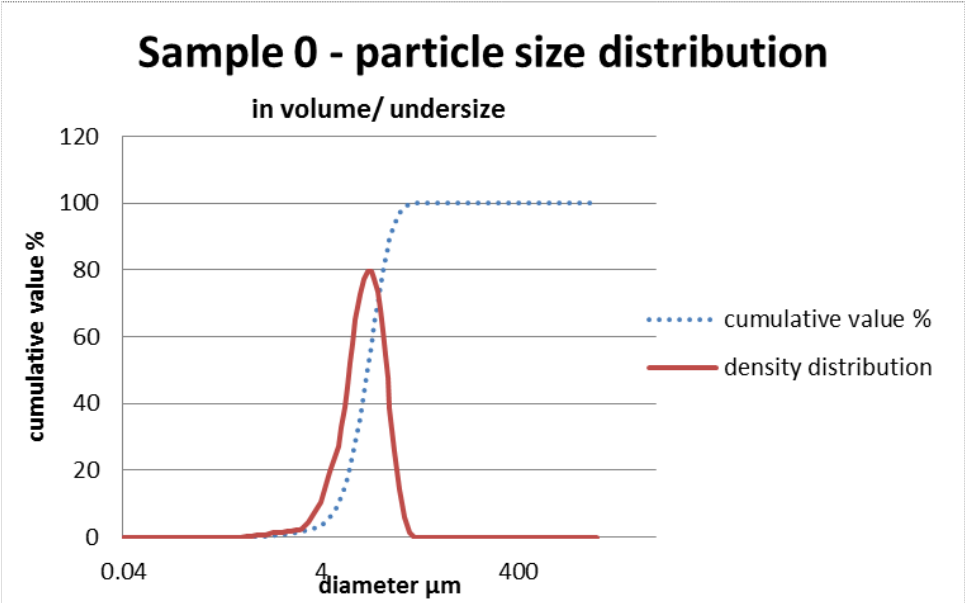

Figure 4.1: CILAS particle size analyzer. The average particle size is determined to be between 6 µm and 8 µm.

Powder morphology was investigated by SEM. Figure 4.2 shows the typical morphology of powders in sample 0.

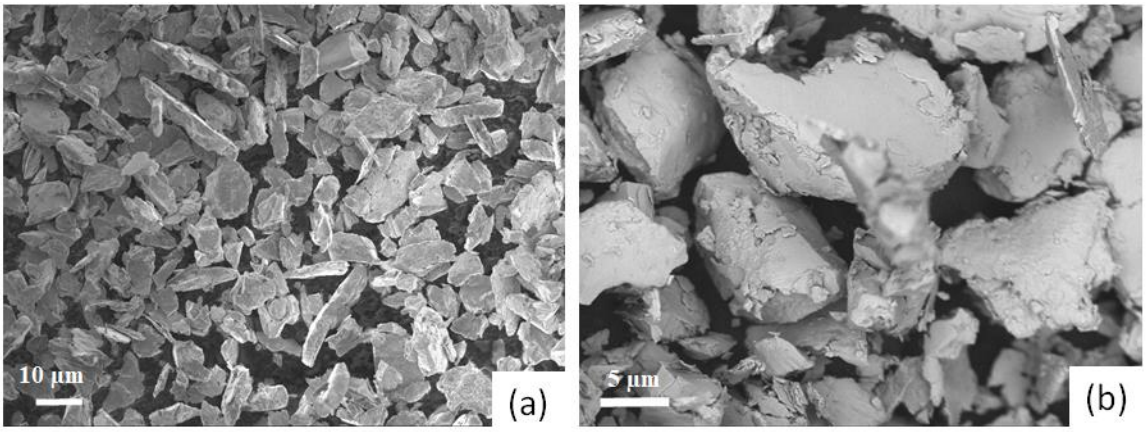

Figure 4.2: (a) SE and (b) BSE micrograph showing the typical morphology of particulate material of sample 0.

The micrographs reveal a uniform composition of the particulate material with plate-like morphology of uniform thickness that is correspondent to the thickness of the quenched ribbons. A more detailed SEM micrograph of the particles in figure 4.3 reveals the presence of micrometer and nanometer scale particles.

The observation of fracture behavior of the particles due to the ball milling process shows that brittle and plastic deformation are present on the same material surface.

Brittle behavior is present due to the fracture of the metallic glass phase while the plastic deformation is observed by the presence of dimples within the structure. The SEM micrographs in Figure 4.3 show the nature of the fracture for the same investigated particle.

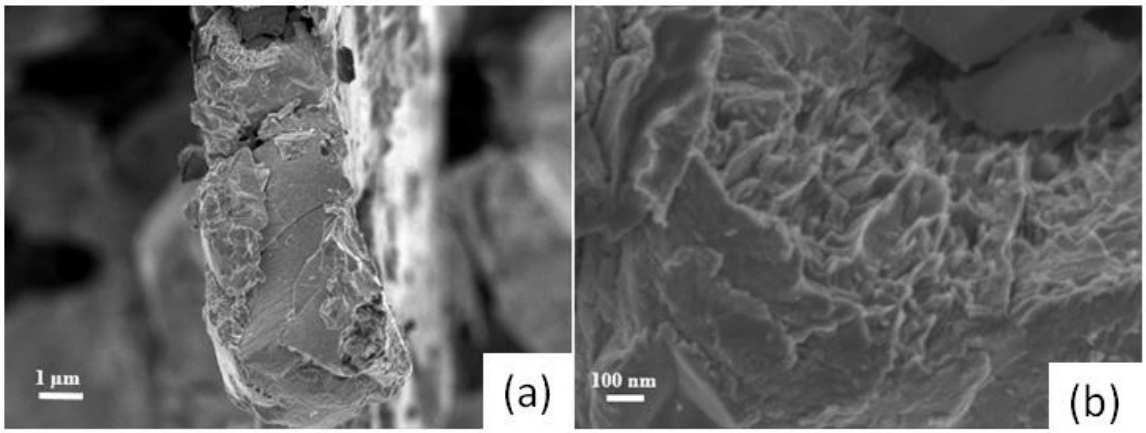

Figure 4.3: SEM micrographs revealing brittle (a) and plastic deformation (b).

Chemical composition of the metal particles from sample 0 was investigated by XEDS in SEM, Figure 4.4. The XEDS spectrum was collected from particles shown in Figure 4.2.

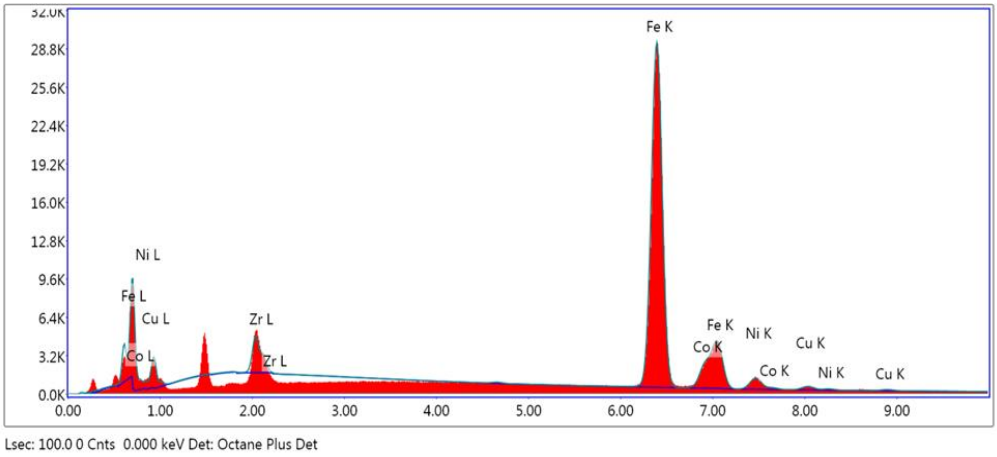

Figure 4.4: XEDS spectrum from an individual particle confirms a Fe-based material and the presence of Ni, Co, Zr, and Cu and chemical composition.

4.3.2 Sample 2

Particle size analysis distribution of sample 2 powders was also performed using the CILAS machine. Particle size distribution for sample 2 is shown in figure 4.5.

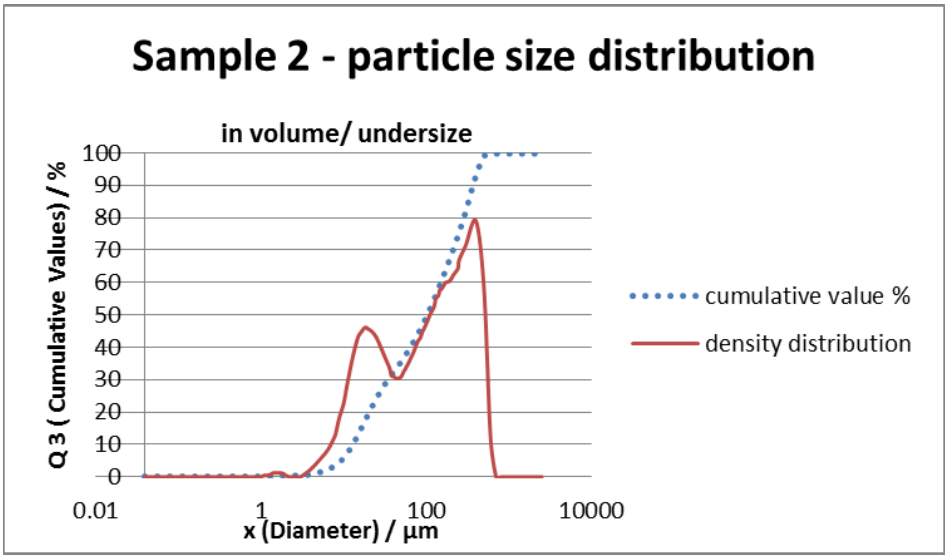

Figure 4.5: Bimodal particle size distribution of sample 2.

From the data obtained of the particle size distribution it can be inferred that a dual distribution of particle size is present in sample 2. Further SEM investigation provided confirmation of bimodal distribution of these particles as shown in figure 4.6. Based on the bimodal particle size distribution, it can be concluded that longer milling time is necessary to produce uniform sized particles.

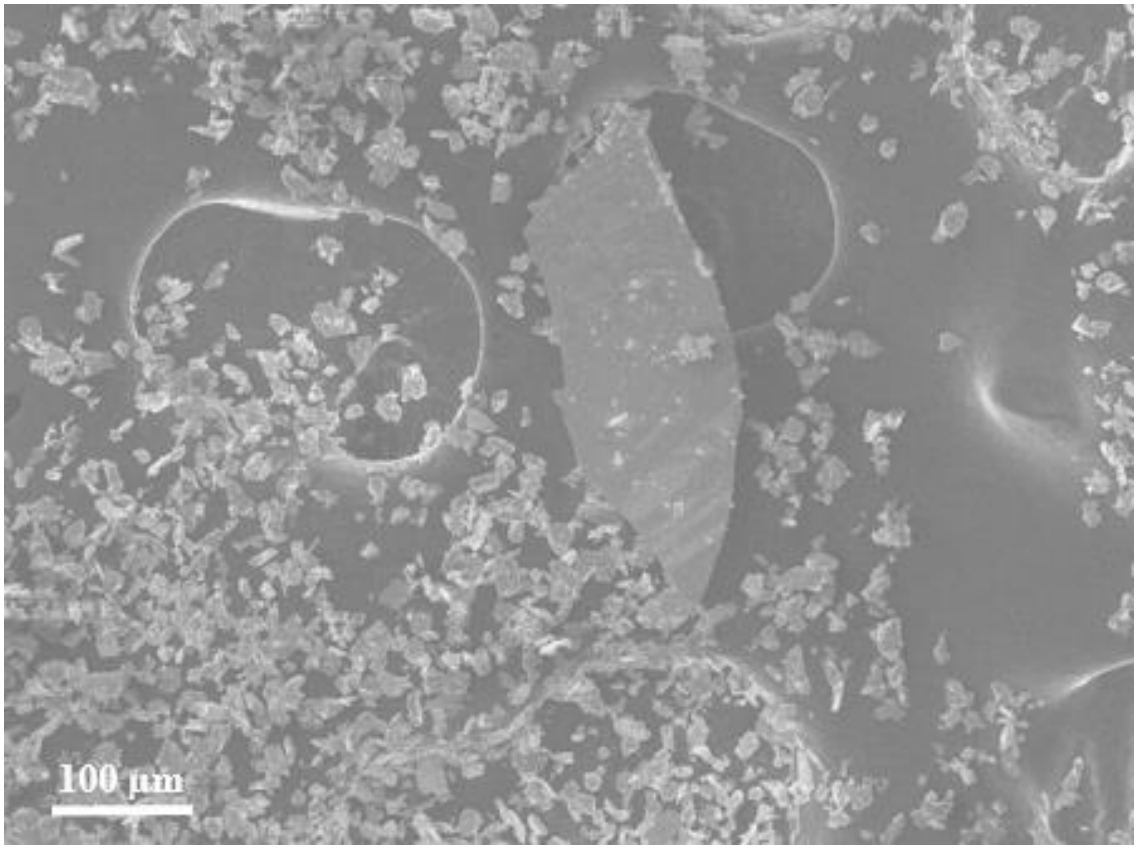

Figure 4.6: Un-milled ribbon within smaller particles.

XEDS maps collected from the surface of the ribbon piece in figure 4.6 indicates the presence of iron oxide, as shown in figure 4.7. The oxidation probably occurred during the ribbon manufacturing process.

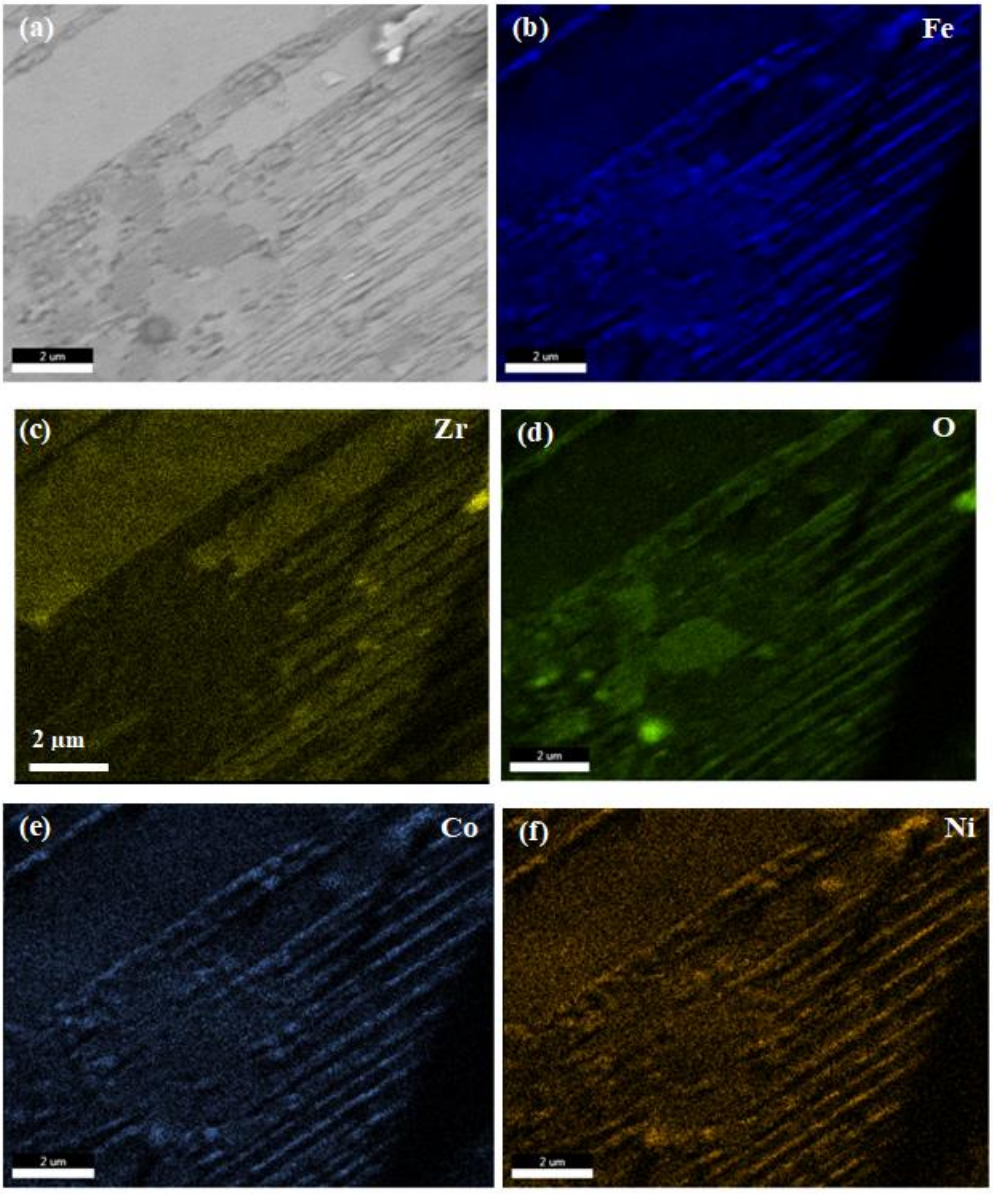

Figure 4.7: (a) BSE micrograph and (b) to (f) corresponding XEDS maps collected from the ribbon surface. The strips observed in (a) seems to be iron oxide rich. It seems that oxidation occurred during ribbon elaboration process or during storage.

4.4 3D Printed Sample from Magnetic Powders

After powder investigation and analysis, several parts have been printed as described in the Experimental Methods. After binder impregnation the sampled have been cured in air at 190°C.

For sintering the cured samples (green parts) were placed in quarts tubes. After air evacuation the tube was flushed with argon several times and then sealed. A sealed tube with a sample inside is shown in Figure 4.8 (a).

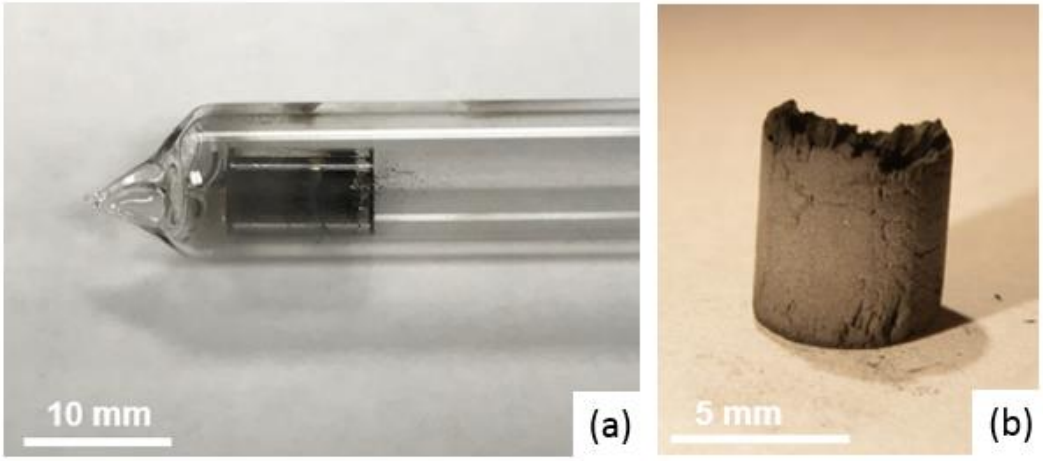

Figure 4.8: (a) Cured samples for 4h at 190°C ready for sintering; (b) Sintered part at 600°C for 24h.

Several samples were sintered at different sintering time and temperature. Figure 4.8 (b) shows the sample sintered at 600°C for 24h.

The sintering process is still under investigation since the temperatures and times used so far did not delivered desired mechanical properties for 3D printed prats. Table 4.1 summarizes the analysis of different powder samples that were investigated.

Table 4.1: Summary of Fe77Ni5.5Co5.5Zr7B4Cu1 powder characterization

Sample name	Sample 0	Sample 1/ April	Sample 2/ April	Sample A	Sample B	Sample 1/ July	Sample 2/ July
Milling system	ZrO	WC	WC	YSZ	WC	YSZ	WC
Milling Time	36h	12h	8h	6h	6h	6h	6h
Milling media	NA	Methanol	Methanol	Methanol	Methanol	Methanol	Methanol
Heat treatment	NA	NA	NA	Annealed 500°C, 10^-2 Torr	Annealed 500°C, 10^-2 Torr	Annealed 500°C, 10^-2 Torr	Annealed 500°C, 10^-2 Torr
Mean diameter (CILAS)	7 µm	NA	NA	67.2 µm	94.61 µm	48.56 µm	85.87 µm
Size distribution (CILAS)	Normal Distribution	Bimodal Distribution	Bimodal Distribution	Normal Distribution	Bimodal Distribution	Normal Distribution	Bimodal Distribution
Morphology (SEM)	Uniform plate-like	Mostly plate-like, large flakes observed	Pieces of original metal ribbon observed	Uniform plate-like	Mostly plate-like, large flakes observed	Uniform plate-like	Mostly plate-like, large flakes observed
Chemical composition (XEDS)	Homogeneous	Homogeneous	Inhomogeneous, metal oxide observed	Homogeneous	Homogeneous	Homogeneous	WC contamination of metal glass particles
Suitable for 3D Printing	Yes	No	No	Yes	No	Yes	No

Chapter 5 - Conclusions

5.1 Conclusions: Mechanical Behavior of 3D Printed Lattice-Structured Materials

Mechanical behavior of lattice structures was explored by successfully printing four different geometries from Inconel 718 and NiMnGa via selective laser melting (SLM) and binder jetting, respectively. Compressive axial testing of heat treated Inconel 718 samples showed higher stress numbers than non-heat treated parts. Moreover, compression tests provided data to correlate specific strength with amount of porosity.

Use of dense and ductile Inconel 718 metal parts produced by selective laser melting method allowed creating a more accurate analysis of the deformation mechanism for different lattice structures and to determine the mechanical behavior for a given geometry. On the other hand, use of binder jetting delivered NiMnGa structures with dual porosity that could benefit the magnetic field strain of MSMAs.

FEA simulation provided a consistent method for full dense Inconel 718 material in order to map the stress concentration along the struts. For the case of NiMnGa parts, modeling presented lack of accuracy due to the internal porosity of the material. Exploring structures developed with NiMnGa material presented challenging understand of failure mechanisms due to the intrinsic brittle characteristic of the material.

Although brittleness of NiMnGa materials contributes to the reduction of mechanical properties of produced parts, creation of lattice structures showed an improvement of specific strength compared to bulk. In conclusion, NiMnGa printed parts provided a

combination of dual porosity and weight reduction. These are desirable mechanical properties that are in line with the enhancement of functional properties.

Future work would involve using a load cell with lower capacity and digital image correlation to track the strain that may produce more accurate results. Performing simulation using nonlinear models with material input from experimental data and a CT scan of the porous structure is necessary to model it taking into account the internal effects of voids in the sample. Also, change in laser pattern and part orientation may be used to avoid defects. Finally, study of a continuum analysis can be performed in the future to understand the behavior of a larger lattice structured parts.

5.2 Conclusions: Iron-Based High Temperature Magnetic Materials

Investigation of Iron-Based High Temperature Magnetic Materials powders was performed to determine printing parameters and mechanical properties of 3D printed parts. The printing parameters investigation was necessary to determine whether the powders were suitable or not to be used in the binder jetting 3D printer system.

Powder investigation and characterization were successfully completed by determining particle size distribution using CILAS machine, powder morphology using SEM, and chemical composition using EDS.

Following analysis, powders from sample 0, sample A, and sample 1/July were accepted for printing due to the normal particle size distribution, uniform plate-like morphology and homogeneous chemical composition. On the other hand, powders from sample 1/April, sample 2/April, sample B, and sample 2/July were no acceptable due to bimodal particle size distribution and morphology with large flakes.

The green parts manufactured using 3D binder jetting approach were cured and sintered. However, produced structures showed poor mechanical properties and need improvement.

Future work for this research includes developing a successful sintering method for the 3D Printed part as well as optimizing parameters during the printing process.

In this sense, characterization of nanoscale powder produced by the ball milling may help understand how to achieve the best printing variables necessary for a successful manufacturing of complex shapes using $Fe_{77}Ni_{5.5}Co_{5.5}Zr_7B_4Cu_1$ metal glass powder.

References

1. Zanaboni, Eleonora. "One Way and Two Way-Shape Memory Effect: Thermo-Mechanical Characterization of Ni-Ti Wires." *Universita degli Studi di Pavia, Pavia, Italy* (2008).

2. Caputo, M. P., and C. V. Solomon. "A facile method for producing porous parts with complex geometries from ferromagnetic Ni-Mn-Ga shape memory alloys." *Materials Letters* 200 (2017): 87-89.

3. Solomon, Virgil C., et al. "Microstructural characterization of Ni-Mn-Ga ferromagnetic shape memory alloy powders." *Journal of Applied Physics* 95.11 (2004): 6954-6956.

4. Dunand, David C., and Peter Müllner. "Size Effects on Magnetic Actuation in Ni-Mn-Ga Shape-Memory Alloys." *Advanced Materials* 23.2 (2011): 216-232.

5. Gaitzsch, Uwe, et al. "Mechanical training of polycrystalline 7M Ni 50 Mn 30 Ga 20 magnetic shape memory alloy." *Scripta Materialia* 57.6 (2007): 493-495.

6. Caputo, Matthew, Mike Krizner, and C. Virgil Solomon. "Investigation of 3d printing parameters of shape memory alloy powders." *Contributed Papers from Materials Science & Technology* 2015 (MS&T"15) 1669 – 1675.

7. Chmielus, Markus, et al. "Training, constraints, and high-cycle magneto-mechanical properties of Ni-Mn-Ga magnetic shape-memory alloys." *The European Physical Journal-Special Topics* 158.1 (2008): 79-85.

8. Müllner, Peter, et al. "Recent Developments in Ni-Mn-Ga Foam Research." *Materials Science Forum*. Vol. 635. Trans Tech Publications, 2010.

9. Berkowitz, A. E., et al. "Hollow metallic microspheres produced by spark erosion." *Applied physics letters* 85.6 (2004): 940-942.

10. Tian, Bin, et al. "Phase transformation and magnetic property of Ni-Mn-Ga powders prepared by dry ball milling." *Journal of Materials Engineering and Performance* 21.12 (2012): 2530-2534.

11. Solomon, Virgil C., et al. "Electron microscopy investigation of spark-eroded Ni–Mn–Ga ferromagnetic shape-memory alloy particles." *Scripta Materialia* 56.7 (2007): 593-596.

12. Ochin, Patrick, et al. "Martensitic transformation in spark plasma sintered compacts of Ni-Mn-Ga powders prepared by spark erosion method in cryogenic liquids." *Materials Science Forum*. Vol. 738. Trans Tech Publications, 2013.

13. Amato, K. N., et al. "Microstructures and mechanical behavior of Inconel 718 fabricated by selective laser melting." *Acta Materialia* 60.5 (2012): 2229-2239.

14. Zhang, Dongyun, et al. "Effect of standard heat treatment on the microstructure and mechanical properties of selective laser melting manufactured Inconel 718 superalloy." *Materials Science and Engineering: A* 644 (2015): 32-40.

15. Gu, D. D., et al. "Laser additive manufacturing of metallic components: materials, processes and mechanisms." *International materials reviews* 57.3 (2012): 133-164.

16. Zhao, Xiaoming, et al. "Study on microstructure and mechanical properties of laser rapid forming Inconel 718." *Materials Science and Engineering: A* 478.1 (2008): 119-124.

17. Wang, Zemin, et al. "The microstructure and mechanical properties of deposited-IN718 by selective laser melting." *Journal of Alloys and Compounds* 513 (2012): 518-523.

18. Wohlers, Terry. "Wohlers report." *Wohlers Associates Inc.* (2014).

19. Frazier, William E. "Metal additive manufacturing: a review." *Journal of Materials Engineering and Performance* 23.6 (2014): 1917-1928.

20. Wauthle, Ruben, et al. "Effects of build orientation and heat treatment on the microstructure and mechanical properties of selective laser melted Ti6Al4V lattice structures." *Additive Manufacturing* 5 (2015): 77-84.

21. Song, X., et al. "Liquid phase separation in melt-spun Cu70Co30 ribbon." *Materials Letters* 31.3-6 (1997): 261-266.

22. Schaedler, Tobias A., and William B. Carter. "Architected cellular materials." *Annual Review of Materials Research* 46 (2016): 187-210.

23. Ashby, M. F. "The properties of foams and lattices." *Philosophical Transactions of the Royal Society of London A: Mathematical, Physical and Engineering Sciences* 364.1838 (2006): 15-30.

24. Deshpande, V. S., M. F. Ashby, and N. A. Fleck. "Foam topology: bending versus stretching dominated architectures." *Acta Materialia* 49.6 (2001): 1035-1040.

25. Gibson, Lorna J., and Michael F. Ashby. *Cellular solids: structure and properties*. Cambridge University Press, 1999.

26. Alghamdi, Ahmad, et al. "Critical Buckling Load for Lattice Column Elements with Variable Dimensions." *KnE Engineering* 2.2 (2017): 84-90.

27. Ashby, Michael F. "Cellular solids–scaling of properties." *Cellular Ceramics: Structure, Manufacturing, Properties and Applications* (2005): 1-17.

28. Aly, Mohamed Shehata. "Behavior of closed cell aluminum foams upon compressive testing at elevated temperatures: Experimental results." *Materials Letters* 61.14 (2007): 3138-3141.

29. Carlton, Holly D., et al. "Mapping local deformation behavior in single cell metal lattice structures." *Acta Materialia* 129 (2017): 239-250.

30. Zheng, Qing, et al. "Analysis of failure loads and optimal design of composite lattice cylinder under axial compression." *Composite Structures* 131 (2015): 885-894.

31. Paranthaman, M. Parans, et al. "Binder Jetting: A Novel NdFeB bonded magnet fabrication process." *JOM* 68.7 (2016): 1978-1982.

32. Chlebus, E., et al. "Effect of heat treatment on the microstructure and mechanical properties of Inconel 718 processed by selective laser melting." *Materials Science and Engineering: A* 639 (2015): 647-655.

33. Sing, Swee Leong, Florencia Edith Wiria, and Wai Yee Yeong. "Selective laser melting of lattice structures: A statistical approach to manufacturability and mechanical behavior." *Robotics and Computer-Integrated Manufacturing* 49 (2018): 170-180.

34. Xia, Mujian, et al. "Influence of hatch spacing on heat and mass transfer, thermodynamics and laser processability during additive manufacturing of Inconel 718 alloy." *International Journal of Machine Tools and Manufacture* 109 (2016): 147-157.

35. Xia, Mujian, et al. "Selective laser melting 3D printing of Ni-based superalloy: understanding thermodynamic mechanisms." *Science Bulletin* 61.13 (2016): 1013-1022.

36. Budynas, Richard Gordon. *Advanced strength and applied stress analysis*. WCB/McGraw-Hill, 1999.

37. Special metals website, Retrieved from: http://www.specialmetals.com/assets/smc/documents/inconel_alloy_718.pdf

38. Myers, Eric. “Finite element modeling (FEM) of porous additively manufactured ferromagnetic shape memory alloy using scanning electron micrograph (SEM) based geometries”. M. S. Thesis, Youngstown State University, 2017.

39. Lee, Huei-Huang. *Finite element simulations with ANSYS workbench 16*. SDC publications, 2015.

40. M. Ozen, Ph.D, “Meshing Workshop,” November 13, 2014.

41. Engineering Alloys 5th Edition, Ed. Norman E. Woldman and Robert C. Gibbons, Van Nostrand Reinhold Company Regional Offices, 1973.

42. National Aeronautics Strategic Implementation Plan, NP-2015-03-1479-HQ www.aeronautics.nasa.gov/strategic-plan.htm

43. Willard, M. A., et al. "Structure and magnetic properties of (Fe 0.5 Co 0.5) 88 Zr 7 B 4 Cu 1 nanocrystalline alloys." *Journal of Applied Physics* 84.12 (1998): 6773-6777.

44. Knipling, Keith E., Maria Daniil, and Matthew A. Willard. "Fe-based nanocrystalline soft magnetic alloys for high-temperature applications." *Applied Physics Letters* 95.22 (2009): 222516.

45. Willard, M. A., M. Daniil, and K. E. Kniping. "Nanocrystalline soft magnetic materials at high temperatures: A perspective." *Scripta Materialia* 67.6 (2012): 554-559.

46. Willard, M. A., K. E. Knipling, and M. Daniil. "Nanostructured Magnets for Improved Energy Efficiency." *Materials Science and Technology, 2010 NRL Review* 180-181.

47. Boeing website, Retrieved from http://www.boeing.com/features/2015/10/innovation-lightest-metal-10-15.page